THE UNIVERSITY OF CHICAGO

OPTICAL MAGNETISM IN NANOPHOTONICS AND OPTICAL MATTER

A DISSERTATION SUBMITTED TO
THE FACULTY OF THE DIVISION OF THE PHYSICAL SCIENCES
IN CANDIDACY FOR THE DEGREE OF
DOCTOR OF PHILOSOPHY

DEPARTMENT OF CHEMISTRY

BY
EMMANUEL GOCE VALENTON

CHICAGO, ILLINOIS
AUGUST 2023

TABLE OF CONTENTS

LIST OF FIGURES

LIST OF TABLES

ACKNOWLEDGMENTS

While it is not unique for many successful Ph.D. graduates to say that their journey was extremely tenuous, I would like to believe that the route I took was among the more difficult ones. Between worldwide events such as the recent pandemic as well as certain personal trials, there have been many obstacles to spring up, each of which I sincerely believed was the final lightning bolt that would sever the slow progress I was making towards finishing the doctoral program.

Thus without the support of many family members, friends, coworkers, and advisers, it is almost certain that I would have abandoned this effort long ago, and consigned myself to a different fate. With their help, I managed to persevere and complete a task that I had previously decided was impossible.

First, I would like to acknowledge my faculty adviser, Professor Norbert Scherer, who accepted me into his research group, provided mentorship over the years, and supported my dissertation and final defense. Through his instruction, I learned about the novel and unique world of Optical Matter and Nanophotonics. I also would like to thank Professor Stuart Rice and Bozhi Tian, who formed the rest of the thesis committee, evaluated the quality of my work, and supported the completion of my degree.

I would like to acknowledge and thank all the members of the Scherer group, especially the ones present when I first joined and the members present now that I am finishing. I would like to thank the postdoctoral fellows, Yuval Yifat, Delphine Coursault, Tian-Song Deng, Itay Gdor, Xiaolei Wang, Matthew Daddysman, Ying Bao, and Nishant Sule, who shaped the group dynamics and did much to add a human element. I would also like to thank Dr. Yanzeng Li for all his help, advice, and scientific insight, which contributed much towards my final projects and the completion of my degree.

Outside of the University of Chicago, I would like to thank Dr. Karl van Bibber who provided much advice on navigating UC Berkeley, research, and graduate school in general.

I also would like to thank Dr. Stephen Leone and Dr. Christopher Kliewer for introducing me to physical chemistry research, as well as Dr. Joseph Nilsen for much advice and recommendations during my early years in undergrad.

Finally, I would like to acknowledge and thank my parents for raising and encouraging me from the very beginning up to the current day. While it may have been difficult to understand the trials of research and graduate school, I am very grateful for your support and advice. I also would like to thank all six of my siblings for all their help and contributions, which while indirect, are more then they imagine.

ABSTRACT

Understanding light-matter interactions in the near-field regime is crucial towards making advances in optical matter and nanophotonics. However, the approach for much of the previous work in these topics is based on analyzing the electric field component of light and the properties of matter that closely relate to the electric field. Since the relative magnetic permeability of most materials is negligible at optical frequencies, the magnetic field component of light-matter interactions was often foregone as a complementary value. Recently, new nanophotonic structures and optical matter building blocks have been fabricated with non-negligible effective magnetic properties. Thus, it is the goal of this thesis to investigate new phenomena and applications in optical matter and nanophotonics based on magnetic light-matter interactions. In this thesis, it is observed that optically magnetic nanoparticles experience the novel Transverse Scattering Force, due to the photonic Hall effect, causing them to undergo trapping behavior that is far from analogous to electric field-based optical trapping. Using the same optically magnetic particles to form the building blocks of nanophotonic structures on conducting substrates, as well as to couple to electronic molecular transitions, it is discovered that the interaction between the electric and magnetic dipole modes and images gives rise to novel scattering behavior and that non-metallic optically magnetic nanostructures can induce a small Purcell effect. The applications for this study on magnetic light-matter interactions in optical matter and nanophotonics include mesoscopic quantum physics, nano-scale machines, and electromagnetic cloaking.

CHAPTER 1

INTRODUCTION

Since early times, the manipulation of light in the visible regime could be closely linked towards mankind's increasing understanding of the natural world. In the early 1600s, Galileo Galilei created what is presumed to be the first telescope and observed surface features such as mountains and basalt plains on the Earth's closest celestial neighbor, the Moon, as well as subtle additions to the known entities of the solar system, such as the moons of Jupiter [1]. Likewise, scientists such as Robert Hooke and Antony van Leeuwenhoek popularized the use of the microscope and made discoveries about the nature of cells and microorganisms [2]. With the discovery of the laser, mankind achieved a new means for controlling light and implementing it as a tool for exploring the natural world and advancing human welfare. Indeed, much of the achievements of the information age have been made either directly or indirectly using laser technology [3].

Since those times, the frontier of research has moved from redirecting light in the far-field regime ($l \gg \lambda$) using macroscopic devices, such as lenses, to the manipulation of light in the near-field regime ($l \lesssim \lambda$) using fabricated devices on the same size scale as the wavelength of light [2]. Indeed, early efforts in this direction were pioneered by Ernst Abbe who formulated the extent to which light can be focused by a macroscopic lens [3]. This concept, known as the diffraction limit, set a boundary to which light can be manipulated using classical, geometric optics. However, further explorations were made by Lord Rayleigh who composed the theory of elastic scattering of light [3], which explains why the sky is blue at midday, and Gustav Mie who explained the scattering of light by spherical particles with sizes on the order of a single wavelength [4]. These theories explored how light interacts with matter on the wavelength scale and were important in bringing the frontier of research in light-matter interactions to the near-field regime. Today, it is well known that nanosize matter ranging from colloidal metal nanoparticles to periodic dielectric photonic crystals can manipulate

light in the near-field regime, beyond the diffraction limit [2, 3, 5]. Indeed, current work ranges from strongly focusing light using noble metal nanoparticles [6], to redirecting light around objects using metamaterials [7], to imaging features smaller than the diffraction limit, to promoting coupling in quantized systems such as quantum dots [2, 8]. Collectively, this research forms the the general topic of nanophotonics, where the study of light-matter interactions on the nanometer scale is explored [2, 3].

More recently with the discovery of the laser, light is not just used to observe matter, but also to exert control such as in the case of optical matter and optical machines [9, 10]. The ability to push and trap micron-size particles in water using laser light was demonstrated by Arthur Ashkin [11]. These findings would form the basis of the optical tweezers method, where micron and nanometer size particles are trapped using focused laser beams, and would earn Ashkin the 2018 Nobel Prize in Physics [12]. Analysis of the light-matter interactions using the Maxwell stress tensor formalism indicates that the induced forces are the result of momentum transfer and redirection as light is scattered by the particle [13]. However, a further treatment, which involves the same theoretical framework, will be undertaken in Chapter 4, which will indicate many additional subtleties involved due to the interplay of the electric and magnetic fields and the particle material properties.

This scenario of light being used to exert forces on a particle of matter in solution can be extended to collections of many particles. In this regime, the forces on a given particle induced by the incident light are complicated by the fact that the light scattered by neighboring particles also needs to be considered. As a result, there is interference between the incident field, the field scattered by the given particle, and the field scattered by neighboring particles, with the resulting forces also becoming an intricate function of the entire collection. In such a situation, many unconventional phenomena arise such as negative torque, non-reciprocal forces, and self-organization [14, 15, 16, 17, 18, 19]. Such a system of many particles with unique forces and self-organizing behavior is often termed "Optical Matter"

[20].

1.1 Outlook

As will be discussed in later chapters, much of the current understanding of nanoscale light-matter interactions at optical frequencies has been gathered by analyzing the electric field and the electrical polarizability of the matter present [2, 3, 13]. Often times it was assumed that the magnetic properties of the system were negligible and that the magnetic field was a complimentary quantity that simply followed the electric field. However, recently there has been a gradual shift in focus towards analyzing the role that the magnetic field may play in nanophotonic and optical matter systems, as well as to fabricate such systems with pronounced optical magnetic properties [21, 22, 23].

With this in mind, the work presented in this dissertation constitutes a series of explorations into nanophotonics and optical matter in order to uncover new phenomena where the magnetic field plays a dominant role. The main theme was to depart from the electric field perspective and to investigate light-matter interactions by analyzing the magnetic field. At times, the research was lead by theoretical insights, where simulations or simple first principles calculations of the magnetic properties would indicate a possible novelty. At other times, the investigative direction was based on the explorations that other researchers have made along this new frontier.

As is the nature of research, certain projects would not come to a successful conclusion, either because the resources and equipment needed were beyond the means available and the experimental design lacked sufficient sensitivity or because the expected phenomenon was in fact not present and what had been discovered was the null result. However, it is my hope that future researchers will be able to build on these findings to achieve new scientific and practical goals based on magnetic light-matter interactions. As such, collected here in this dissertation are the most informative and salient results, organized so as to make it easier

for the reader to understand what has already been done and what foundations are available to be built upon.

1.2 Structure of Dissertation

This dissertation will be structured with first a brief outline in Chapter 2 of relevant electromagnetic theory, as well as a short description of the simulation methods used, . Since the majority of the simulations performed in conjunction with the experiments was done using open source packages or software created in-house, as many details will be provided in this Chapter and throughout the thesis to aid the reader.

Then in Chapter 3, the experimental methods used for the proceeding works will be described. For many of the experiments and sample preparations involved, home-built optical setups and custom procedures were frequently used, so as much detail will be included in order to aid the reader in recreating the experiment, should they choose to do so.

Starting first with optical matter, the endeavors to trap particles by relying on the magnetic component of light and the magnetic properties of matter will be presented in Chapter 4. In this work, it is discovered that magnetic optical trapping is not a direct analogue to prior optical trapping work, which was often based on plasmonic metal nanoparticles with strong electric polarizabilities and focused laser beams with intense electric fields. In fact a new phenomenon, the photonic Hall effect, needs to be considered in order to account for the trapping behavior observed, and the simple point electric dipole based model used to explain previous optical trapping behavior needs to be enlarged to include what is termed, the Transverse Scattering Force.

Turning from optical matter to nanophotonics in Chapter 5, interactions in the near field regime, mediated by the magnetic field were investigated. A high index nanoparticle with magnetic Mie resonances was placed on a metallic substrate acting as a mirror and the interaction between the particle and its mirror image was explored. It was discovered

that the finite conductance, and similar deviations from perfect mirror behavior, of the substrate have significant effects on the scattering behavior of the magnetic and electric Mie resonance modes, as the particle is placed on the mirror substrate. As opposed to the typical theoretical model for magnetic dipole and electric charge distributions placed near mirrors–the method of mirror images–which is commonly described in electromagnetism textbooks, it was discovered that a new model is needed, which takes into account the finite conductance of the substrate. In this Chapter, the corresponding experiments and the new theory will be presented.

In Chapter 6 the topic of nanophotonics was once more taken up and strong and weak coupling in nanophotonic systems with magnetic properties was explored. More specifically, the possible coupling between the lanthanide ion, Eu^{3+}, and a high index nanoparticle was investigated. As will be discussed in this Chapter, Eu^{3+} has electronic transitions which occur via a transition magnetic dipole, while the high index nanoparticle posses strong magnetic Mie resonance modes. Thus, it is expected that the combination of the two in close spatial proximity would result in some form of strong or weak coupling that is magnetic in nature. The results of these experiments will be presented along with a theoretical explanation.

CHAPTER 2

THEORETICAL BACKGROUND AND SIMULATION METHODS

For the scope of this dissertation, mainly the classical picture of light will be considered. If necessary, a semi-quantum mechanical treatment of matter will be included in order to fully explain certain light-matter interactions. However, considering that most phenomena discussed in this thesis is mediated by light in the near-infrared to ultraviolet range and that nanosize particles with masses much larger than single atoms or molecules are considered, this treatment should be adequate.

Naturally, the beginning of a theoretical treatment of light would start first with Maxwell's equations. Many outstanding textbooks [13, 24] and resources [2, 25, 26, 27] have been written to give a thorough explanation of Maxwell's equations and related electromagnetic phenomena, so a short summary of relevant principles will be discussed here. Listed below are the differential form of the four macroscopic Maxwell equations [13],

$$\nabla \cdot \mathbf{D} = \rho \tag{2.1}$$

$$\nabla \cdot \mathbf{B} = 0 \tag{2.2}$$

$$\nabla \times \mathbf{H} = \mathbf{J} + \frac{\partial \mathbf{D}}{\partial t} \tag{2.3}$$

$$\nabla \times \mathbf{E} + \frac{\partial \mathbf{B}}{\partial t} = 0 \tag{2.4}$$

where Equations 2.1, 2.3, and 2.4 follow from Gauss's Law, Ampére's Law, and Faraday's Law, respectively, while Equation 2.2 is based on the nonexistence of magnetic monopoles [13, 24, 25, 26, 27]. $\mathbf{B}$ and $\mathbf{E}$ are the Magnetic induction and Electric field, respectively, and $\mathbf{D}$ and $\mathbf{H}$ are the Electric Displacement and Magnetic field, respectively. The current density and charge density are denoted as $\mathbf{J}$ and ρ, respectively. $\mathbf{E}$, $\mathbf{B}$, $\mathbf{D}$, and $\mathbf{H}$ are functions of

time and space and typically have the following harmonic form,

$$\mathbf{E}(\mathbf{r},t) = \mathfrak{Re}\left(\mathbf{E}(\mathbf{r})e^{-i\omega t}\right) \tag{2.5}$$

Thus the time dependence can be removed via the application of the Fourier transform, after which Maxwell's equations become [2],

$$\nabla \cdot \mathbf{D}(\mathbf{r},\omega) = \rho(\mathbf{r},\omega) \tag{2.6}$$

$$\nabla \cdot \mathbf{B}(\mathbf{r},\omega) = 0 \tag{2.7}$$

$$\nabla \times \mathbf{H}(\mathbf{r},\omega) = \mathbf{J}(\mathbf{r},\omega) - i\omega\mathbf{D}(\mathbf{r},\omega) \tag{2.8}$$

$$\nabla \times \mathbf{E}(\mathbf{r},\omega) = i\omega\mathbf{B}(\mathbf{r},\omega) \tag{2.9}$$

where ω is the frequency of light.

The material properties of the system are contained in ρ, $\mathbf{J}$, $\mathbf{D}$ and $\mathbf{H}$. At the macroscopic level, the electric displacement and magnetic field are further defined as [13],

$$\mathbf{H} = \frac{1}{\mu_0}\mathbf{B} - \mathbf{M} \tag{2.10}$$

$$\mathbf{D} = \epsilon_0\mathbf{E} + \mathbf{P} \tag{2.11}$$

where $\mathbf{M}$ is the magnetic moment density, $\mathbf{P}$ is the electric dipole moment density, and ϵ_0 and μ_0 are the vacuum permittivity and vacuum permeability, respectively. Assuming that the matter involved is linear, local, and isotropic, Equations 2.10 and 2.11 reduce to [2],

$$\mathbf{H} = \frac{1}{\mu\mu_0}\mathbf{B} \tag{2.12}$$

$$\mathbf{D} = \epsilon\epsilon_0\mathbf{E} \tag{2.13}$$

where the magnetization is proportional to the magnetic field ($\mathbf{M} = \chi_m\mathbf{H}$) by the magnetic

susceptibility constant (χ_m), just as the polarization is proportional to the electric field ($\mathbf{P} = \epsilon_0 \chi_e \mathbf{E}$) by the electric susceptibility constant (χ_e), and μ and ϵ are the relative permeability and permittivity, respectively. The relative permeability and permittivity are functions of space and frequency, reflecting the structure and response of the material present. However, at optical frequencies the bulk magnetic response of most materials negligible, so the relative permeability is often neglected (that is, $\mu \approx 1$).

Over wide electromagnetic frequency ranges, bulk matter will often exhibit absorption and dispersion properties. This behavior is due to the charge carriers of the material being unable to oscillate as fast as the electromagnetic wave, as well as electronic and rovibrational transitions present within the constituent molecules and similar phenomena stemming from the molecular and atomic nature of the material [2, 13, 24, 25, 26, 27]. In order to capture this dispersive behavior, the relative permittivity is often set as a complex value,

$$\epsilon = \epsilon' + i\epsilon'' \tag{2.14}$$

For most materials, the complex relative permittivity can be described as follows [13],

$$\epsilon(\omega) = 1 + \frac{Ne^2}{\epsilon_0 m} \sum_j \frac{f_j}{\omega_j^2 - \omega^2 - i\omega\gamma_j} \tag{2.15}$$

where e is the electron charge, N is the molecule volume density, m is the electron mass, f_j is number of electrons of the jth molecule, ω_j and γ_j are phenomenological constants reflecting the resonance frequency and damping of the jth molecule, and the sum is over every molecule.

If a conductor is being considered, then the unbound charge carriers need to be taken into account. In this case, the complex relative permittivity is described using the Drude

model and has the following form [13],

$$\epsilon_D(\omega) = \epsilon(\omega) + i\frac{Ne^2 f_0}{\epsilon_0 m\omega(\gamma_0 - i\omega)} \tag{2.16}$$

where $\epsilon(\omega)$ is Equation 2.15, f_0 are the free electrons per molecule and γ_0 is a phenomenological constant reflecting the damping of the conducting material.

If discrete objects and environments of different media are considered, then the interfaces between the different materials give rise to boundary conditions that the electromagnetic fields need to fulfill [2, 13, 24]. Using the integral form of Maxwell's equations, the boundary conditions at the interfaces can be derived as follows [2, 13],

$$\mathbf{n} \cdot (\mathbf{D}_2 - \mathbf{D}_1) = \sigma \tag{2.17}$$

$$\mathbf{n} \cdot (\mathbf{B}_2 - \mathbf{B}_1) = 0 \tag{2.18}$$

$$\mathbf{n} \times (\mathbf{E}_2 - \mathbf{E}_1) = 0 \tag{2.19}$$

$$\mathbf{n} \times (\mathbf{H}_2 - \mathbf{H}_1) = \mathbf{K} \tag{2.20}$$

where σ and $\mathbf{K}$ is the surface charge density and surface current density, respectively, and where the subscripts indicate the regions on either side of the boundary. Equations 2.17 and 2.18 govern the fields normal to the boundary surface, whereas Equations 2.19 and 2.20 govern the fields tangential to the boundary.

Maxwell's equations, together with material properties and system structure represented respectively by the permittivity and permeability constants and the electrodynamic boundary conditions, form the essential fundamental principles needed to analyze the optical matter and nanophotonic phenomena presented in this thesis. In the following section, these principles will be used to analyze the light scattering of a spherical particle in a homogeneous medium to lay further theoretical groundwork by shedding light on an elemental building block frequently used for creating the nanophotonic and optical matter systems present in

later work.

2.1 Mie Theory

The work presented in this thesis will make frequent use of spherical nanoparticles, either in nanophotonic structures or as elements of optical matter. Fortunately, the electromagnetic fields of a spherical particle scattering incoming light were already analyzed by Gustav Mie [4]. As a result, the theories originally derived by Gustav Mie and expanded by others will be used often in order to gain an understanding of the light-matter interactions investigated in this thesis [4, 28, 29, 30, 31].

To give a brief overview of Mie theory, a system consisting of a homogeneous sphere of arbitrary material in vacuum under a plane wave is first considered. It is assumed that the sphere is centered at the origin and that the plane wave is propagating in the $\hat{\mathbf{z}}$ direction and polarized in the $\hat{\mathbf{x}}$ direction. To find a solution of the resulting fields outside the particle, Maxwell's curl equations (Equations 2.8 and 2.9) are first considered. By applying the curl operator to both sides of Ampére's Law and Faraday's Law, the full set of Maxwell's equations for the region outside the particle can be reduced to the following homogeneous vector Helmholtz equations,

$$\nabla^2\mathbf{E} + k^2n^2\mathbf{E} = 0 \tag{2.21}$$

$$\nabla^2\mathbf{H} + k^2n^2\mathbf{H} = 0 \tag{2.22}$$

with the help of the identity, $\nabla\times\nabla\times = -\nabla^2 + \nabla\nabla\cdot$, and the divergence Maxwell equations. The wavenumber is indicated by k, and n is the complex index of refraction of the medium.

The solutions to the vector Helmholtz equations are dictated by the spherical symmetry

and boundary conditions of the problem and have the following form [28],

$$\mathbf{E} = \mathbf{M}_v + i\mathbf{N}_u \tag{2.23}$$

$$\mathbf{H} = in\mathbf{N}_v - n\mathbf{M}_u \tag{2.24}$$

where

$$\mathbf{M}_\Psi = \nabla \times (\mathbf{r}\Psi) \tag{2.25}$$

$$nk\mathbf{N}_\Psi = \nabla \times \mathbf{M}_\Psi \tag{2.26}$$

and $\Psi = u, v$ is the solution to the scalar Helmholtz equation, $\nabla^2\Psi + k^2n^2\Psi = 0$.

For the scattered field, the solution to the scalar Helmholtz equation in spherical coordinates is [28],

$$u = e^{iwt}\cos(\phi)\sum_{n=1}^{\infty} -a_n(-i)^n \frac{2n+1}{n(n+1)} P_n^1(\cos\theta) h_n^{(2)}(kr) \tag{2.27}$$

$$v = e^{iwt}\sin(\phi)\sum_{n=1}^{\infty} -b_n(-i)^n \frac{2n+1}{n(n+1)} P_n^1(\cos\theta) h_n^{(2)}(kr) \tag{2.28}$$

The function, $P_n^1(\cos\theta)$, is an associated Legendre polynomial with order 1, and $h_n^{(2)}(kr)$ is a spherical Bessel function. The coefficients, a_n and b_n are given as follows [28],

$$a_n = \frac{\psi_n'(mk\alpha)\psi_n(k\alpha) - m\psi_n(mk\alpha)\psi_n'(k\alpha)}{\psi_n'(mk\alpha)\zeta_n(k\alpha) - m\psi_n(mk\alpha)\zeta_n'(k\alpha)} \tag{2.29}$$

$$b_n = \frac{m\psi_n'(mk\alpha)\psi_n(k\alpha) - \psi_n(mk\alpha)\psi_n'(k\alpha)}{m\psi_n'(mk\alpha)\zeta_n(k\alpha) - \psi_n(mk\alpha)\zeta_n'(k\alpha)} \tag{2.30}$$

where α is the radius of the sphere, and ψ_n and ζ_n are the Riccati-Bessel functions given in the notation used by Debye. For Equations 2.29 and 2.30, m in this case is the index of refraction.

2.2 Maxwell Stress Tensor

The ability of light to induce a force on matter has been hypothesized and explored by figures such as Johannes Kepler in the 17th century [32], down to Ashkin in more recent times [11]. Since light carries momentum, there exists the possibility for momentum to be exchanged during light-matter interactions, giving rise to optically induced forces due to momentum conservation laws. The theoretical framework for this phenomenon is contained in a formalism known as the Maxwell stress tensor, which also forms the foundation for much optical matter theory [2, 10, 13].

The Maxwell stress tensor formalism originates from Maxwell's equations and the Lorentz force, which is as follows,

$$\begin{aligned} \mathbf{F} &= q\mathbf{E} + q\mathbf{v} \times \mathbf{B} \\ &= \int_V (\rho\mathbf{E} + \mathbf{J} \times \mathbf{B})\, dV \end{aligned} \tag{2.31}$$

where ρ and $\mathbf{J}$ are the charge and current densities. The Lorentz force gives the force on a charge and current distribution due to the electromagnetic fields present and is based on the fundamental definitions of the electric and magnetic field. Following the derivation given in Jackson, the Maxwell stress tensor is obtained from these fundamental laws and is given as follows [13],

$$\hat{\mathbf{T}} = \epsilon_0 \mathbf{EE} + \mu_0 \mathbf{HH} - \frac{1}{2}\left(\epsilon_0 \mathbf{E} \cdot \mathbf{E} + \mu_0 \mathbf{H} \cdot \mathbf{H}\right) \hat{\mathbf{I}} \tag{2.32}$$

where $\hat{\mathbf{I}}$ is the identity matrix, and $\mathbf{EE}$ and $\mathbf{HH}$ are outer products of the vectors $\mathbf{E}$ and $\mathbf{H}$. The quantity $\hat{\mathbf{T}}$ indicates the flow per unit area of momentum and can be integrated over an arbitrarily defined closed surface to find the change in the field and mechanical momentum

within the enclosed volume [2, 13],

$$\int_{\partial V} \hat{\mathbf{T}} \cdot d\mathbf{A} = \frac{d}{dt}\mathbf{G}_{\text{field}} + \frac{d}{dt}\mathbf{G}_{\text{mech}} \tag{2.33}$$

$$\mathbf{G}_{\text{field}} = \frac{1}{c^2}\int_V (\mathbf{E} \times \mathbf{H}) dV \tag{2.34}$$

$$\frac{d}{dt}\mathbf{G}_{\text{mech}} = \int_V (\rho\mathbf{E} + \mathbf{J} \times \mathbf{B}) dV \tag{2.35}$$

where c is the speed of light. Note that the integrand in Equation 2.35 is simply the Lorentz force (Equation 2.31). Over the course of one optical cycle, the field momentum change averages to zero. Thus, Equation 2.33 reduces to [2],

$$\int_{\partial V} \left\langle \hat{\mathbf{T}} \right\rangle \cdot d\mathbf{A} = \langle \mathbf{F} \rangle \tag{2.36}$$

which is the mechanical force exerted on the enclosed volume due to an exchange of momentum between the enclosed matter and the electromagnetic field.

Since the Maxwell stress tensor formalism follows from Maxwell's equations and the Lorentz force, it in principle would yield the sum of all forces induced by electromagnetic fields. Further analysis can then isolate individual forces, such as the ones due to electric or magnetic material properties, as will be explored in Chapter 4.

2.3 Simulation Software and Methods

Frequent recourse was taken to analytical and numerical simulations in order to elucidate underlying physical principles and to confirm experimentally observed phenomena. In particular, three different software packages were used: MiePy and StokeD, SMUTHI, and MEEP FDTD.

MiePy and StokeD are two Python modules developed by Dr. John Parker, a former student of the Scherer group, for the purpose of calculating electromagnetic phenomena of

nanoparticles in an aqueous solution and simulating the Langevin dynamics of the nanoparticles due to the forces from the electrodynamic interactions [33, 34]. MiePy is based on generalized multiparticle Mie theory (GMMT), calculating the electromagnetic fields, forces, and other related quantities around a collection of arbitrarily shaped particles under a user-defined coherent light source [31, 33]. StokeD solves the Langevin equation for a collection of particles, taking into account fluid viscosity, interparticle hydrodynamic interactions, simple nonspherical particle shapes, and other external forces [34]. The two modules are sufficient for calculating a wide variety of phenomena involving optical matter and were frequently used for the work described in Chapter 4.

The package, SMUTHI (Scattering by MUltiple particles in THIn-film systems), is an open-source software developed to calculate the electromagnetic fields of a collection of particles embedded in layered media [35]. It is based on Mie theory and Sommerfeld integrals, as well as the T-matrix formalism for the handling of particles with arbitrary shapes. This software package was used heavily in the work described in Chapter 5. Shown in Figure 2.1 is a summary of the basic operating principles of SMUTHI.

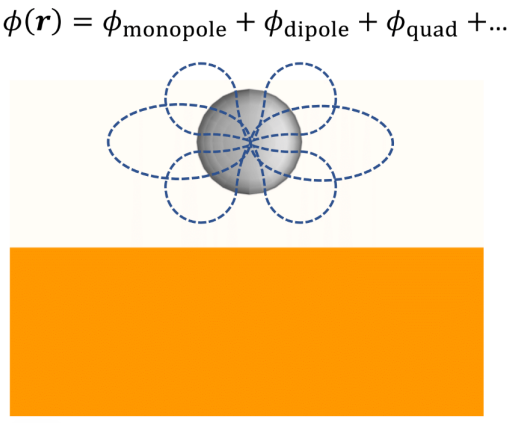

Figure 2.1: Cartoon representation of the basic operating principles of the open-source software package SMUTHI. The electromagnetic fields around particulate matter embedded in layered medium, such as a nanoparticle on a semi-infinite gold slab in air as shown in this diagram, are decomposed into electric and magnetic multipole modes using Mie theory and the T-matrix formalism [35].

Finally, the finite-difference time-domain method (FDTD) was applied frequently in order to confirm the results obtained by the MiePy and SMUTHI packages, as well as to gain initial insight into experimental results. It is a well known method of iteratively solving Maxwell's equations in order to obtain the electromagnetic fields of an arbitrary system, and for the later work in this dissertation, the MEEP (MIT Electromagnetic Equation Propagation) implementation of FDTD was chosen [36, 37, 38]. MEEP is an open-source software implementation of FDTD with a Python, Scheme, and C++ interface and a library of different materials and analyses tools. In later work, MEEP was frequently run on parallel threads using the OpenMPI framework in order to decrease computation time.

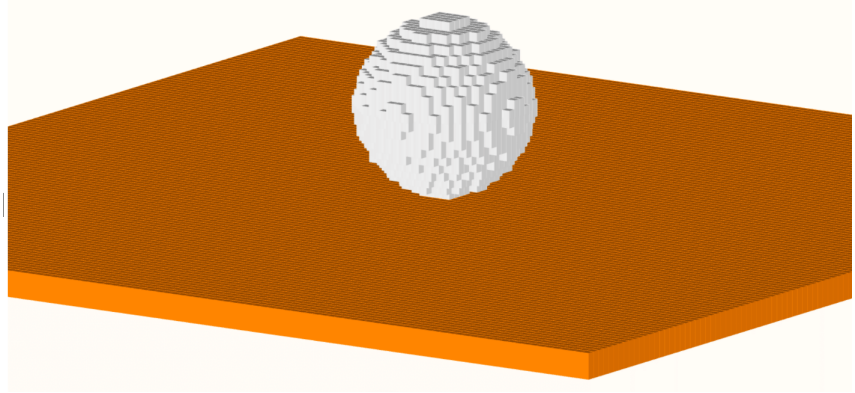

Figure 2.2: Cartoon representation of the basic operating principles of the MEEP implementation of the FDTD method. The system, consisting of a nanoparticle on a gold substrate, is discretized onto a three-dimensional grid. Then Maxwell's equations are iteratively solved at each grid point to give the electric and magnetic fields themselves [36, 37, 38].

These simulation software were run on a home-built Linux desktop machine, outfitted with an Intel i7-7800X processor and 128 GB of RAM, as well as on a Linux high-performance computing (HPC) center [39], equipped with Intel Broadwell computing nodes with 64 GB of RAM and 28 CPU cores per node. Real world time to completion varied from seconds, as was frequently the case for simulations using MiePy and SMUTHI, to several days for certain FDTD simulations.

CHAPTER 3

EXPERIMENTAL METHODS

Presented here is a description of the salient experimental procedures and equipment used throughout the course of the work in this dissertation.

3.1 Nanoparticle Characterization by Dynamic Light Scattering

Throughout this thesis, spherical particles with sizes on the order of 100 nm were used as the elemental building blocks for optical matter and nanophotonic systems of interest. These nanoparticles are available from commercial suppliers, as well as from collaborators, and can be made from metals such as gold, silver, aluminum and platinum, as well as from semiconductors, polymers, and ceramics [40, 41, 42].

Once received, dynamic light scattering (DLS) measurements were taken in order to assess the nanoparticle quality. During this process, laser light is scattered by the suspended nanoparticles. By taking the autocorrelation function of the scattering intensity over time, the diffusion coefficient may be found, from which the effective particle size is calculated using the Stokes-Einstein equation [43],

$$d_H = \frac{kT}{3\pi\eta D} \tag{3.1}$$

where k is Boltzmann's constant, T is absolute temperature, η is viscosity, D is the diffusion coefficient, and d_H is the diameter of the hard sphere that would diffuse as fast as the particle being measured.

Along the same line, by inducing electrophoretic motion using an external electric field and measuring the Doppler shift of the scattered light via interferometry, the nanoparticle electrophoretic mobility may be calculated. Using Henry's equation, the nanoparticle zeta

potential can be derived from the electrophoretic mobility [43],

$$U_E = \frac{2\epsilon\zeta f(\kappa\alpha)}{3\eta} \tag{3.2}$$

where ζ is the zeta potential, U_E is the electrophoretic mobility, ϵ is the absolute permittivity, η is viscosity, and $f(\kappa\alpha)$ is Henry's function. Since all measurements were made using aqueous solutions with moderate electrolyte concentrations, the value of 1.5 was used for Henry's function, which is known as the Smoluchowski approximation [43].

To carry out this characterization, the as-received aqueous nanoparticle samples were first diluted using 18 MΩ water in order to reduce the concentration to an acceptable range for DLS measurements. After dilution, the solutions were sonicated for ~ 4 minutes to disperse the nanoparticles and break up aggregates. Then, the nanoparticle solutions were placed into new disposable plastic cuvettes for size measurements, or into proprietary folded capillary zeta cells (Malvern Instruments DTS1070) for zeta potential measurements. The zeta cells were first rinsed with 18 MΩ water before use. The samples would then be loaded into the light scattering instrument (Malvern Zetasizer Nano ZS), which was capable of performing both DLS size and zeta potential measurements. An example of the resulting zeta potential and DLS size measurement of an aqueous solution of silicon nanoparticles received from collaborators is shown in Figure 3.1.

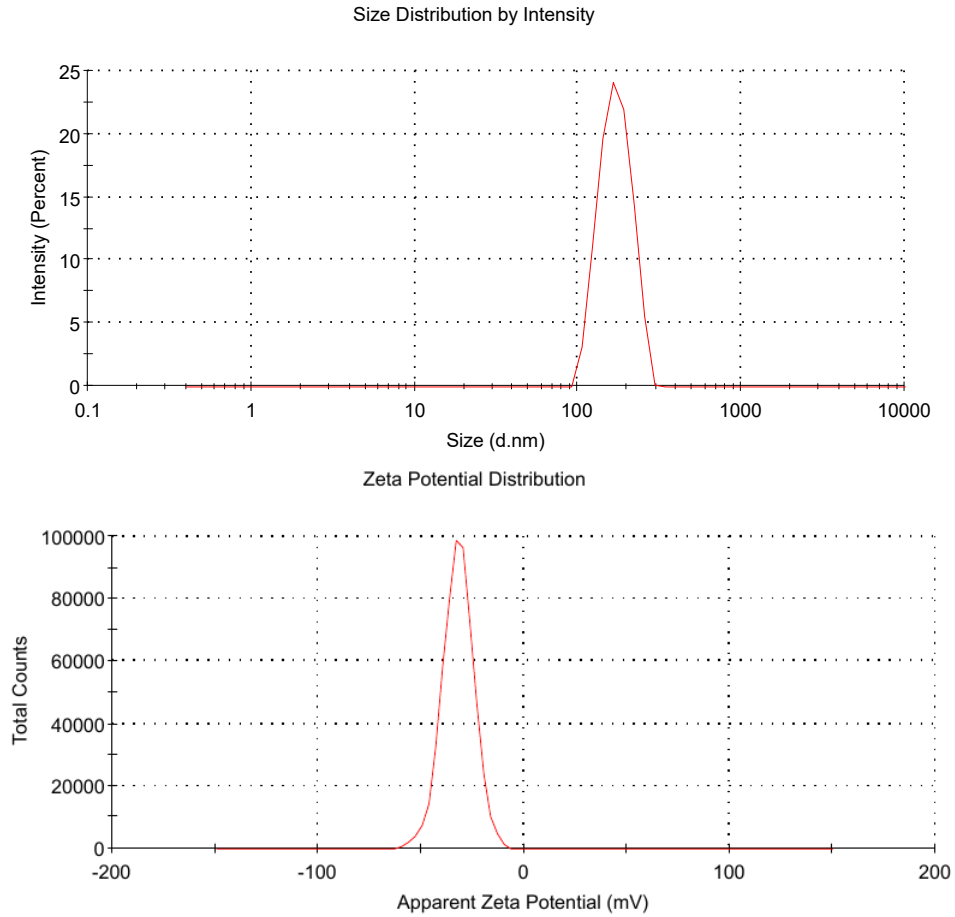

Figure 3.1: Zeta potential and DLS size measurements of an aqueous solution of silicon nanoparticles used as nanoparticle building blocks for further experiments in this thesis.

3.2 Scanning Electron Microscopy for Nanoparticle and Nanophotonic Structure Characterization

Due to the small size of the nanophotonic systems and optical matter investigated in this thesis, frequent use was made of scanning electron microscopy to image and characterize these systems. Specifically, a field effect scanning electron microscope (Carl Zeiss Merlin SEM) with secondary and backscattered electron detectors was used to make observations. A summary of the internal elements of the instrument is shown in Figure 3.2. Briefly, the SEM employs a Schottky field emitter electron gun to produce a stream of electrons which

are accelerated by an extractor through an aperture. After exiting the aperture, the electron beam passes between two condenser coils separated by another aperture which attenuate and focus the electron beam flux. The electron beam is then focused onto the sample, where it is raster scanned using a set of deflector coils. The resulting secondary and backscattered electron intensity are recorded as a function of electron beam position in order to reconstruct the full image [44].

While both secondary electrons and backscattered electrons are emitted from the sample due to the incoming electron beam, the secondary electrons are generated much closer to the point of impact and can be used to acquire images with much finer resolution [3, 44]. Thus for the majority of the imaging performed in this thesis, only secondary electrons were measured.

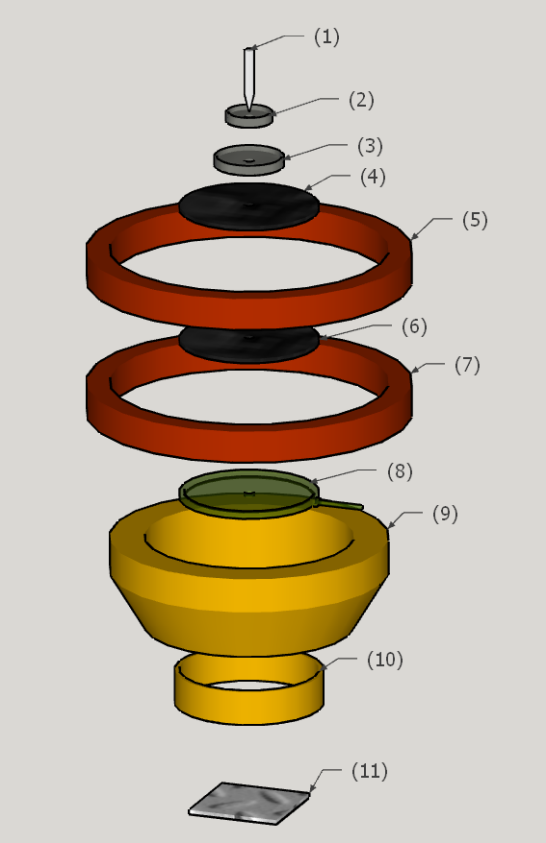

Figure 3.2: Schematic of the basic elements of the field emission scanning electron microscope. (1-2) Electron gun. (3) Extractor. (4) Anode aperture. (5) Upper condenser. (6) Aperture. (7) Lower condenser. (8) Scintillating secondary electron detector. (9) Objective lens. (10) Deflecting coils. (11) Microscope sample. Note that only the secondary electron detector is shown.

Samples were typically placed on a conductive indium tin oxide (ITO) coated microscope coverslips and then fixed to metal pin stubs (Ted Pella) using copper tape. Incoming electron flux would be transferred from the sample to ground via the conducting ITO layer and copper tape to prevent build up of electron charge that would severely distort the microscope image. It is possible to image samples on nonconducting substrates, such as bare glass, using very low probe current and voltage. However, the image quality is reduced significantly.

At times, high quality images were needed of nonconducting samples on insulating substrates. In these cases, the sample would be coated by a thin layer of evaporated metal

before imaging. A sputter coater (Cressington 208HR) was used to deposit a layer of Pt/Pd alloy, typically 5 nm thick, on the sample and substrate. The vacuum level at the start of this process was 0.08 mbar. At this level, the metal atoms would diffuse from the target to the sample and coat all exposed surface area in an even fashion. Note that the metal coating would severely affect the optical properties of the sample and would be applied after all experiments were completed.

3.3 Electron Beam Physical Vapor Deposition

A number of experiments in this dissertation involved nanophotonic systems with a thin metal film. To create these films, the desired metal was vacuum deposited onto a glass substrate using an electron-beam evaporator (AJA ATC-Orion 8E e-beam evaporation system). First, the substrate would be cleaned by plasma cleaning (Plasma Etch PE-100LF) with oxygen or by washing with ethanol or acetone and blow-drying with nitrogen. For certain trials, both methods would be used. Then, the substrate would be taped to a copper sample holder and loaded into the e-beam evaporator vacuum chamber. After manipulating the sample holder over the metal targets and pumping down the vacuum chamber, the desired material target would be rotated into position and the proprietary e-beam melting and evaporation sequence started. The deposition thickness was monitored using a proprietary crystal oscillator (AJA ATC-Orion) coupled to the e-beam control unit. After depositing the selected metal, further layers may be applied in the same manner, or the sample manipulated out of the target region and removed via the airlock.

Potential material targets include Titanium, Germanium, Gold, Silver, and Platinum. While the exact parameters used for deposition varied case to case, in general the guidelines given in Ref. [45] were taken into account.

3.4 Optical Trapping Setup

Described here is the optical trapping setup used for the creation and investigation of optical matter. It also serves as the model for optical setups used in additional experiments such as fluorescence spectroscopy and fluorescence lifetime measurements.

In order to generate the near-infrared (NIR) light needed for optical trapping, a continuous wave Ti:sapphire laser setup (shown in Figure 3.3) was used. At the beginning of the setup is a commercial continuous wave, diode-pumped visible laser (Spectra-Physics Millennia Vs laser) for generating laser light with an output power of 5 Watts and a wavelength of 532 nm. The 532 nm light is fed into a commercial Ti:sapphire laser cavity (Spectra-Physics Model 3900S) to produce 770 nm laser light of 750 mW power. The NIR light is directed through a Faraday isolator to prevent reflections from downstream components from interfering with the Ti:sapphire cavity and then focused by a lens through a diamond pinhole for spatial filtering. The laser source is then re-collimated with an additional lens.

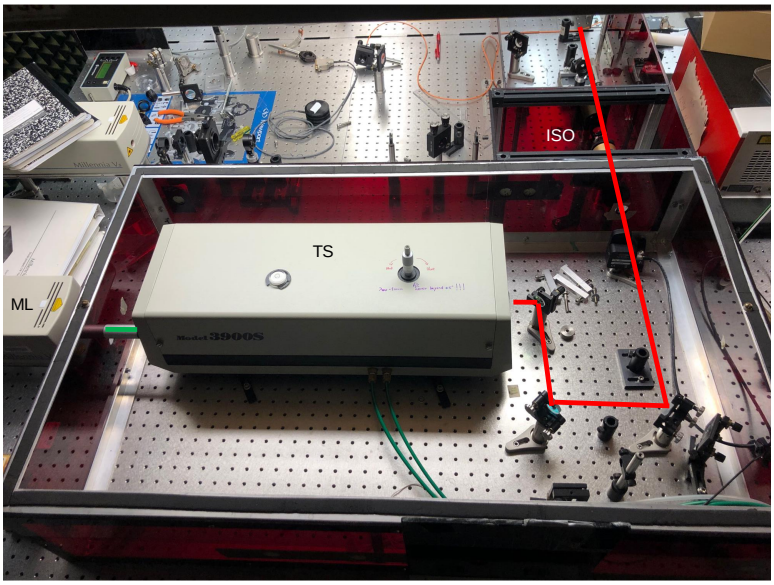

Figure 3.3: Image of the continuous wave Ti:sapphire near-infrared laser source used for optical trapping experiments. (ML) Diode-Pumped, continuous wave visible laser source. (TS) Ti:sapphire laser module. (ISO) Free-space optical isolator. The red line segments schematically depict the optical beam path.

Shown in Figure 3.4 is a diagram of the optical setup for optical matter and optical trapping experiments. The incoming collimated NIR laser light is first sent towards a pair of beam position stabilizing mirrors (Optics in Motion Analog Fast Steering Mirror). Because the Ti:sapphire laser source and the subsequent optical setup span two joined laser tables, any positional shifts due to vibrations, humidity, temperature, etc. need to be corrected. Together, the two beam position stabilizing mirrors ensure that the incoming NIR laser beam is traveling along a predesignated path. A partially reflective mirror deflects $\sim 4\%$ of the NIR beam towards a quadrant photodiode (QPD) which forms a feedback loop with the beam stabilizing mirror. As a result, if the beam is deflected away from the center of the QPD, the control module rapidly adjusts the beam stabilizing mirror's actuators so as to correct the beam.

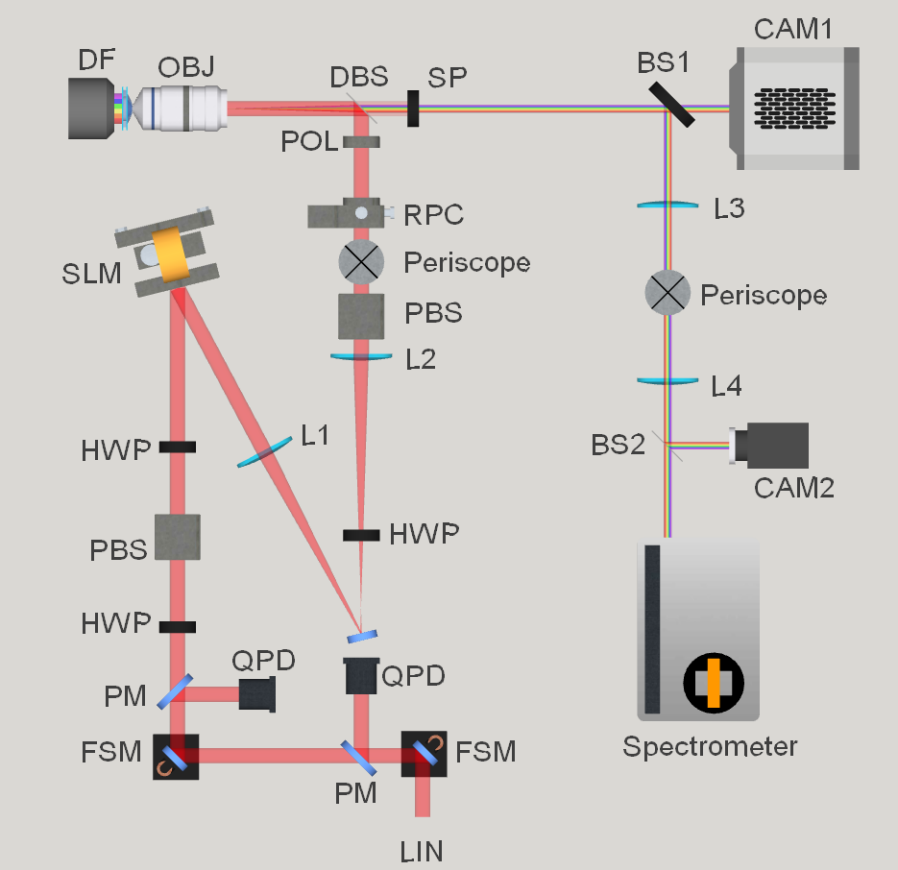

Figure 3.4: Schematic of the optical setup used for optical trapping experiments. (LIN) near-infrared laser from continuous wave Ti:sapphire laser source. (FSM) Beam stabilization mirror. (PM) Partially reflective mirror. (QPD) Quadrant photodiodes. (HWP) Half-wave plate. (PBS) Polarizing beam splitter. (SLM) Spatial light modulator. (L1-4) Lens. (RPC) Radial Polarization converter. (POL) Polarizer. (DBS) Dichroic beamsplitter. (OBJ) Microscope Objective. (DF) Dark-field condenser. (SP) Short-pass and notch filter. (BS1) 80:20 beamsplitter. (CAM1) sCMOS array detector. (BS2) 50:50 beamsplitter. (CAM2) CMOS color camera.

Once past the beam stabilization mirrors, the NIR laser is directed through a half-wave plate (HWP) and polarizing beam splitter (PBS). The HWP rotates the beam polarization, which was originally parallel to the laser table, to a user-defined orientation. The PBS transmits the component of light polarized parallel to the laser table and deflects the rest of the light to a beam dump. The two optics together allow the transmitted power to be

adjusted from the laser source maximum down to zero. A second HWP rotates the laser polarization to perpendicular to the laser table.

The laser beam is then reflected off a spatial light modulator (Meadowlark HSPDM512-785), which allows arbitrarily defined phase profiles to be added to the laser wavefront. However, for the majority of the trapping experiments described in this thesis, a simple uniform phase profile was applied, or the spatial light modulator (SLM) itself replaced with a mirror. After reflecting off the SLM, the beam is sent through a 4F lens system, as well as a HWP and a PBS to ensure linear polarization, before entering a Radial Polarization converter (RPC). The RPC is a commercial liquid crystal based converter (ARCoptix) that converts the beam polarization from linear to azimuthal or radial polarization. The azimuthal or radial polarization may be checked by placing a polarizer after the RPC and imaging resulting beam on the transverse plane while rotating the polarizer. If properly polarized, two bright lobes of equal intensity will appear, similar in shape to an atomic p-orbital, which will rotate with the polarizer.

The cylindrical vector beam enters the back of an inverted microscope (Nikon eclipse Ti-E) and is reflected by a dichroic beamsplitter (DBS) towards the microscope objective (Nikon Plan Apo IR NA 1.27 60x water immersion). The objective focuses the azimuthally polarized NIR beam onto a sample cell constructed from sandwiching an adhesive spacer (GRACE BIO–LABS) between two glass microscope coverslips. The sample is also illuminated by an incoherent white light source (i.e. lamp or white LED) focused through a dark-field condenser.

Both the backscattered NIR laser light and the incoherent white light scattered by the sample are collected by the microscope objective and directed back towards the DBS. The NIR light is blocked by the DBS, a 694 nm short pass filter (Semrock BrightLine 694nm/SP), and a 785 nm notch filter (Semrock Stopline 785nm). The remaining scattered light is split along two beam paths by a 80:20 beam splitter inside the microscope. Roughly 20% is

directed towards a sCMOS array detector (Andor Neo) for imaging, while the rest of the light is directed out of the microscope for spectroscopic measurements and further imaging. The sCMOS array detector would typically be cooled to -25 °C and is capable of high frame rates on the order of 100 fps.

After exiting the microscope, the scattered light is relayed by a 4F lens system towards a 50:50 beamsplitter. About half of the light is reflected towards a CMOS color camera (FLIR Grasshopper 3) in order to obtain color images of the sample in real time. The remaining half of the light is transmitted into a Czerny-Turner imaging spectrometer and recorded on an EM-CCD array detector (Andor Newton). The CMOS color camera is has no internal cooling mechanism and is capable of frame rates of 121 fps or less. Conversely, the EM-CCD array can be cooled to to -70 °C and has a proprietary electron multiplying readout to magnify weak input signal and improve image contrast.

3.5 Procedure for Spectroscopic Measurements

In general, the procedure for recording and processing spectral measurements was constant throughout this thesis, with some differences noted when applicable. First, the Czerny-Turner imaging spectrometer was calibrated using the emission of a Mercury-Argon lamp (Ocean Optics HG-1). Then, the spectrometer diffraction grating was rotated to produce a specular reflection, allowing the image of the entrance slit to be seen on the CCD array detector. The exterior optics would then be adjusted to align the the image of a given sample onto the entrance slit, and then the diffraction grating would be rotate back to its initial position to produce a diffracted reflection.

When taking spectra, an image spanning the full CCD array, or a select region of interest, would be recorded and saved. Shown in Figure 3.5 is one example of a raw image recorded on the CCD array after a measurement. In this case, the scattering of a silicon nanoparticle is being measured, and consequentially the diffracted image of the nanoparticle is being

recorded.

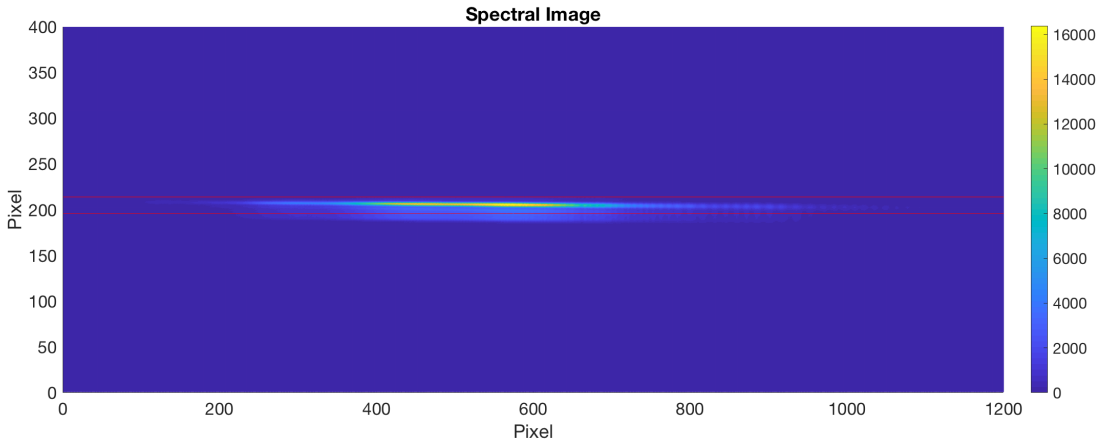

Figure 3.5: Raw image of diffracted scattering of a silicon nanoparticle as recorded directly on the CCD array detector. CCD region of interest is 400 x 1200 pixels, with the red horizontal lines indicating the pixels that will be binned together to derive the final scattering spectrum. Color bar indicates the electron counts recorded on each pixel.

After performing a similar measurement of the output of the Mercury-Argon lamp, it can be determined to which vertical column of pixels the scattered light of a given wavelength is falling on. Thus the pixel electron counts give the scattering intensity, and the pixel horizontal position gives the scattering intensity wavelength. During the post-processing, only the data from a select number of pixel rows around the diffracted image would be used in order to avoid including in further analysis the noise from pixels far from where the scattered light fell, which in principle contain no relevant data. The counts of the selected pixels would be horizontally binned together to give the final spectrum.

3.6 Setup and procedure for TCSPC measurements

For light-matter interactions occurring on the nanosecond to picosecond timescale, time-correlated single photon counting (TCSPC) and its related electronics where used to record these phenomena, especially the systems described in Chapter 6. While many excellent resources such as Refs. [46] and [47] have been published describing this method, a brief

summary is provided here. TCSPC involves (periodically) optically exciting a given system of interest with a pulse of light and then recording the time that a photon is emitted, returning the system to the ground state. The excitation power levels and pulse excitation frequency are kept to a low level in order to ensure that during each cycle of excitation and emission, ideally just one photon is detected. By recording the time delay between the excitation and emission and then binning the delay times into a histogram, a probabilistic decay curve may be generated showing the time-dependent nature of the system at hand. For fluorescence (or luminescence) measurements, the fitted decay time gives the excited state lifetime and insights into possible non-radiative relaxation processes.

Illustrated in Figure 3.6 are the major components of the TCSPC system used in the work of this thesis. The central component is the timing card (Picoquant TimeHarp 260 PICO Dual) which can record input timing pulses with a precision of 25 ps. It is driven by a periodic synchronization signal from the mode-locked oscillator of the excitation laser light source (Fianium, WL-SC400-4). The synchronization output from the laser source is a NIM compatible signal, so the voltage is first reduced using a 12dB attenuator (Mini-Circuits VAT-12) before reaching the timing card.

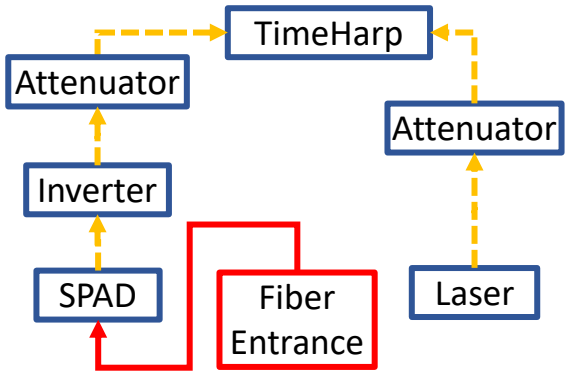

Figure 3.6: Schematic of the optical and electronic components of the time-correlated single photon counting setup. **(Blue)** Electronic modules and radio-frequency components. **(Red)** Fiber collimator and fiber optic cable. **(Gold)** Radio-frequency signal connections.

The emitted light from a given experiment was focused towards the entrance of fiber optic cable using a collimator. The light was guided by the cable to the active region of a single-photon avalanche diode (Perkin-Elmer SPCM-AQR-15-FC), which releases a pulsed TTL signal when triggered. In order to bring the output signal from the single-photon avalanche diode (SPAD) to an acceptable voltage range, an inverter (Picoquant SIA400 Inverter/Attenuator) and another 12db attenuator were connected to the SPAD before the timing card.

In a conventional TCSPC setup, the excitation laser light source is connected to the timing card using a long cable (on order of 100 ft) in order to delay the synchronization signal so that the emission is recorded before the excitation laser pulse timing signal [46, 47]. This configuration has become widely used because only a small fraction of excitation laser pulses would induce a detectable emission photon. Thus in this configuration, only laser pulse cycles where an emitted photon is detected are measured. However, the timing card in this work measures instead the delay between the most recent synchronization signal and the detector signal. Provided that the periodic synchronization signal used to drive the card is consistent, then the need for a delay cable is eliminated.

Furthermore, the timing card is capable of recording the absolute timestamp that the detector signal arrives, as well as the delay between the synchronization and detector signal. This feature allows for other analyses, such synchronizing the photon counting measurements with imaging measurements, to be conducted other than solely binning the delay times.

CHAPTER 4

MAGNETIC FIELD TRAPPING AND PHOTONIC HALL EFFECT OF SILICON NANOPARTICLES

Reproduced in part with permission from: Yanzeng Li, Emmanuel Valenton, Spoorthi Nagasamudram, John Parker, Muhua Biswas, Stuart A. Rice, Norbert F. Scherer. Magnetic field trapping and photonic Hall effect of Si nanoparticles. Manuscript in preparation.

Since its inception in the late 1900s [11], optical trapping has evolved into a significant area of study, catalyzing substantial advancements in diverse fields such as bio-medicine [48, 49, 50], material science [51, 52, 53, 54, 55, 56, 57], and macroscopic quantum physics [58, 59, 60]. Despite nearly five decades of research, optical trapping remains a critical topic of interest, with recent efforts shifting from investigating single-particle systems towards exploring many-body effects – the coherent electrodynamic coupling among multi-particles with light. This research has uncovered a multitude of fascinating physical phenomena, including optical matter formations [61, 20, 62, 63, 17], optical matter machines [9], symmetry-breaking electrodynamics [64, 65, 66, 14, 67, 68, 69, 70, 71, 15], and mesoscopic dipole interactions [72, 73, 74].

Indeed so, the mechanism underlying single-particle trapping has been extensively explored and matured into the foundation of complex trapping schemes [75, 76, 77]. Typically, metallic nanoparticles with inherent plasmonic resonances allow for strong interactions with the electric field of light, making them widely selected materials in modern nanoparticle-manipulation systems, such as Au and Ag. This trapping mechanism embodies the electricity aspect of light-matter interactions; however on the other side of the coin, how magnetism functions remains unsolved to date. Despite some recent theoretical works [78, 79] suggesting possible confirmatory experiments using magnetodielectric nanoparticles due to their inducible magnetizations in contrast to the polarizations of metallic particles, experimental

evidence still lacks. As Lukas Novotny notes in his book, at optical frequencies, induced magnetization is practically zero [2].

Nevertheless, he follows up with an interesting prediction: magnetization in optical trapping would function oppositely to what electrical polarization does. That is, a particle with a negatively induced magnetization will be attracted to magnetic field extremes. Obviously, this inference contradicts the hypothesis based on the point-dipole model [78], where the magnetic field-governed gradient or dipole force virtually shares the same characteristics with the electric version, meaning that the attraction should be attributed to positive magnetizations instead. These conflicting arguments form the central question that demands an urgent confirmation of the underlying mechanism of magnetic field trappings to ensure the integrity of optical trapping theory.

Here, we present the proof of a principle experiment demonstrating *magnetic field trapping* of nanoparticles in optical frequencies for the first time. Silicon nanoparticles, optically excited at their magnetic dipole modes, were observed to reach dynamic equilibrium in the most intense magnetic field region, albeit the electric field extreme present nearby, unambiguously manifesting the contribution of the magnetic field of light. More interestingly, however, such trapping behaviors cannot be appreciated simply by either the point-dipole model or the sign of magnetization, but rather a *photonic Hall effect* takes the responsibility. Our optical model, developed from the generalized Lorenz-Mie theory (GLMT), uncovers the essence of the photonic Hall effect-engendered optical force – that is, a nonconservative or scattering force featured by a quasi-anisotropy relevant to the polarization of excitation fields.

Remarkably, the quality of quasi-anisotropy converts the scattering force into a necessity for the stability enhancement of optical traps, which complements Ashkin and Gordon's Earnshaw theorem whereby only the dipole (conservative) force is deemed to be favorable for any successful optical trappings [80]. This discovery may pave a novel path toward the

study of mesoscopic quantum physics, for instance, in which the scattering (nonconservative) force almost always refers to as one of the primary factors hindering a single nanoparticle from arriving at a quantum motional ground state [81].

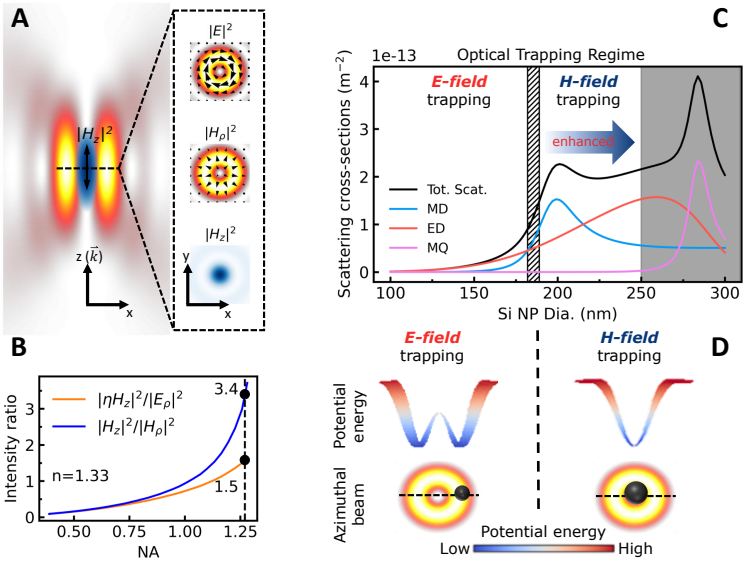

Figure 4.1: **Optical magnetic trapping of Si nanoparticles with azimuthal beam.** **(A)** The intensity profile of a tightly focused azimuthal beam as decomposed into three constituent fields: E (reddish), H_ρ (reddish), and H_z (blue) at focal volume, with black arrows representing their polarization directions. **(B)** The ratios of H_z to E and H_ρ intensity vary with the numerical aperture (NA) of the focusing lens. The black dots in the plot indicate the ratios at the NA of 1.27, which corresponds to the microscope objective used for trapping particles in water (n=1.33). **(C)** The Mie resonance of Si nanoparticles are analyzed in terms of their scattering cross sections in multipole modes at the excitation wavelength of 770 nm. The point of first intersection between MD and ED curves at Dia.=182 nm splits the optical trapping regime into E- and H-field-dominated trapping domains. The patterned and grey-colored spectral sections represent the transition stage (182-190 nm) and uninteresting region (>250 nm) of this study, respectively. **(D)** The calculated potential energy profiles, across the azimuthal beam, illustrate the trapping tendencies of Si nanoparticles in the E- and H-field trapping domains.

In our experiments, it is imperative to construct a spatially isolated magnetic field in order to demonstrate optical magnetic trapping unambiguously. This was achieved by using an azimuthal beam, which generates a longitudinally polarized magnetic field H_z at the beam center (where the electric field is absent) through the azimuthally polarized electric

component E of light following Faraday's law of induction, as seen in Fig. 4.1A. Additionally, the magnetic component of light with radial polarization H_ρ shares the annular region with the electric component. The intensity of the induced magnetic field H_z augments with the increase in the tightness of the beam focus, as seen in Fig. 4.1B where the ratios of $|\eta H_z|^2/|E|^2$ and $|H_z|^2/|H_\rho|^2$ vary as a function of an objective's numerical aperture (NA) ranging from 0.4 to 1.29. From the plots, when the azimuthal beam is tightly focused with an NA of 1.27, matching the microscope objective used in the experiments, the induced magnetic field H_z attains significant intensification, with an intensity 1.5 and 3.4 times greater than the intrinsic electric E and magnetic H_ρ fields, respectively. This trapping light source will strengthen the H_z-actuated optical force and reduces any competing forces due to other fields, enabling successful optical magnetic trapping. The calculation assumes water conditions (n=1.33) and normalizes the electric field ratio with the reversed wave impedance $\eta = \sqrt{\epsilon_w/\mu_w}$, where ϵ_w and μ_w are water's permittivity and permeability.

Besides the engineered trapping field, Si nanoparticles are the other crucial factor making this work possible as they are able to interact with the induced magnetic field H_z via Mie-type magnetic dipole (MD) resonances, acquiring magnetic field-mediated forces [21]. However, caution must be taken with regard to their electric dipole (ED) resonances, which can be excited by the annular-distributed electric field E and result in electric field-mediated forces acting on the particles simultaneously. The magnitude of these two competing forces depends not only on the intensity of the respective fields, as discussed previously, but also on the strength of the field-particle interaction, which can be deduced from the scattering properties of the particles. Figure 4.1C presents a scattering spectrum (in black) for Si nanoparticles with varying dimensions, calculated at an excitation wavelength of 770 nm using the GLMT method. The decomposed spectra for the fundamental modes of MD and ED are included to measure the relative strength of these modes. It is clear that the MD mode is dominant over the ED mode only in a narrow dimensional range centered at a diameter of 200 nm, which

corresponds to the MD peak. This resonant signature naturally constitutes our preliminary hypothesis: only when Si nanoparticles fall into this dimensional range should magnetic field trapping be achievable.

Verifying this conjecture and identifying optical magnetic trappings can be accomplished by observing where the illuminated Si nanoparticles reach their electrodynamic equilibrium in the trapping field, as a direct consequence of the disparity in the spatial distributions of the induced magnetic field H_z and the electric field E (see Fig. 4.1A). According to the potential energy profiles computed for various-sized Si nanoparticles in Fig. 4.1D, the shift in the low-energy valley from the azimuthal beam's annular zone to its center evidence light-particle interactions transitioning from being dominated by the ED mode to being dominated by the MD mode. Note that the inclusion of the magnetic quadrupole (MQ) mode in Fig. 4.1C is intended to mark the rightmost boundary of our interest. Optical forces due to higher-order modes become pronounced beyond this boundary and fall outside the scope of this study [82]. Moreover, we do not consider thermophoresis due to the relatively low absorption properties of Si nanoparticles at the excitation wavelength [82].

Figure 4.2A portrays the schematic diagram of our experimental trapping unit where a water-immersion microscope objective focuses an azimuthal beam into a water-filled chamber in which polydisperse Si nanoparticles diffuse. The close-up depicts the azimuthal beam focused near the top water-glass interface, with arrows indicating the polarizing directions and spatial distributions of both the induced magnetic H_z (blue) and electric E (red) fields. The putative particle trapped at the extreme of the induced magnetic field provides a visual representation of magnetic field trapping. For more details about the Si nanoparticle synthesis and the experimental implementation, please refer to the materials and methods [82].

As anticipated, a single Si nanoparticle was found to be stably confined at the azimuthal beam's central region, as shown in Fig. 4.2B where the dashed circle outlines the trap-

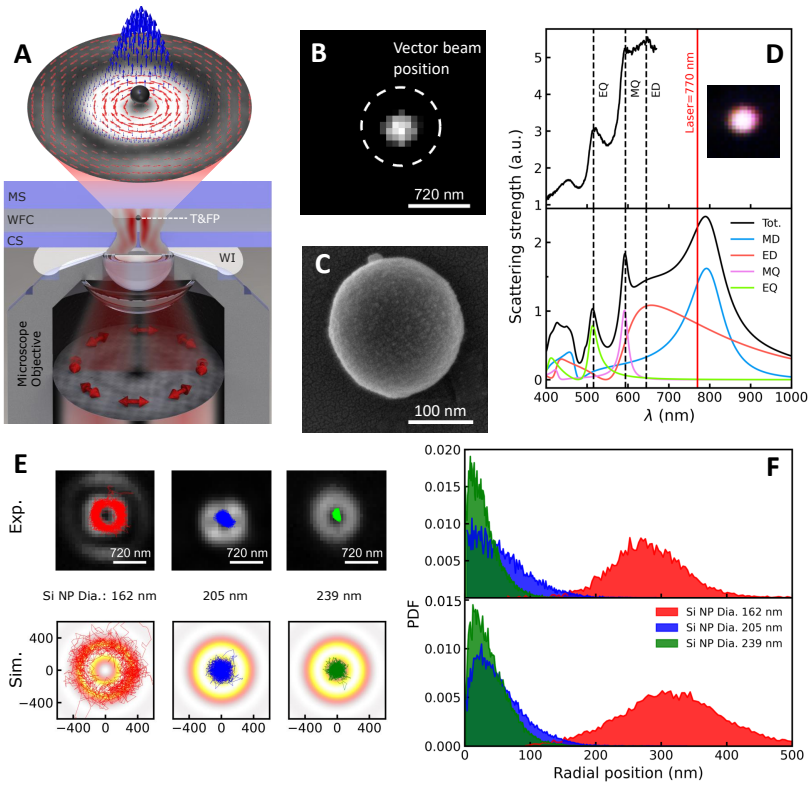

Figure 4.2: **Experimental evidence of optical magnetic trapping of Si nanoparticles being trapped in a space dominated by magnetic fields of light.** **(A)** Schematic representation of the microscope objective that is employed to generate a tightly focused azimuthal beam for trapping Si nanoparticles in a water chamber. The closeup displays a virtual azimuthal beam trapping a putative Si nanoparticle at the trapping plane, with animated arrows indicating the longitudinal and azimuthal polarization of H_z (blue) and E (red). **(B)** Far-field image of a representative Si nanoparticle with a diameter of 205 nm as being trapped at the center of the azimuthal beam delineated by the white dashed circle. **(C)** SEM micrograph of a drop-cast-prepared Si nanoparticle with the same dimension as the trapped one shown in panel **(B)**. **(D)** The Size of the Si nanoparticle shown in panel **(B)** is determined by comparing the particle's in-situ scattering measurement (upper panel) with the calculated Mie scattering spectra (lower panel) and aligning their respective scattering signatures featured by the multipole modes. **(E)** Trapping trajectories of three Si nanoparticles with different sizes are presented, overlaid with their trapping beam profiles in the background, where the upper and lower rows exhibit the experimental and GMT-Langevin dynamic simulation results, respectively. Their radial position distributions are displayed in panel **(F)**.

ping beam that was blocked with a notch filter (see fig. S3). When the particle was optically secured in position, an in-situ spectroscopic measurement was performed to obtain the

scattering spectrum of the particle (upper panel of Fig. 4.2D). Reproducing the measured scattering features in GLMT-calculated spectra (lower panel of Fig. 4.2D) allows for the determination of the particle's diameter which was about 205 nm. Such dimension indicates a nearly maximal MD resonance that the particle acquired at the excitation wavelength of 770 nm. Scanning electron microscopy (SEM) was also employed as an auxiliary tool to characterize the particle's quality. Figure 4.2C displays a separate Si nanoparticle that was prepared using drop-casting technique and exhibited the same scattering response as the one in panel B. The SEM measurement confirms that these two particles have identical dimensions with tolerance of ± 2 nm, further verifying the trapped particle's dimension as well as structural quality. More elaboration on the particle size determination can be found in fig. S6. The trajectories and probability density function (PDF) of the trapped particle along the radial direction are shown in Fig. 4.2E and F, respectively, represented by the blue color. Both statistical analyses, based on experimental (upper) and simulation (lower) results, provide evidence that the particle is trapped at the beam center, where the maximum induced magnetic field H_z is present. This observation confirms the magnetic field trapping effect. For more detailed information on the experiments and simulations, interested readers are directed to the materials and methods section [82].

With these experimental and simulation confirmations, we retrospected and questioned our initial assumption that magnetic field trapping is solely applicable to particles dominated by magnetic dipole (MD) modes. To examine this hypothesis, we selected two particles, with diameters of 162 nm and 239 nm, and subjected them to trapping experiments and simulations. The results are displayed in Fig. 4.2E and F for easy comparison. The smaller particle (162 nm in red) was successfully trapped in and underwent random walking along the ring-like region due to its dominant ED mode that leads to a robust interaction with the electric field E. This trapping mechanism can be adequately explained by the well-established point-dipole model based on electric light-matter interactions. However, the

larger particle (239 nm in green) defied our expectations by remaining at the center of the beam and exhibiting even tighter confinement, reflected in its narrower linewidth in the radial position distribution. This unexpected trapping scenario confuses as it starkly contrasts the 162 nm particle, even though they both have overwhelming ED modes, allowing them to interact with the electric component of the trapping light more effectively.

This confusion gets aggravated as one attempt was made to fathom the paradoxical observations via a force analysis with the point-dipole model. This is because the Si nanoparticles' magnetic polarizability (or magnetization), as excited by the current trapping laser frequency, is negative, resulting in a repulsive magnetic dipole or gradient force (see fig. S7). This implies that the magnetically polarized particles should behave as a magnetic field "ejector" rather than a "seeker," contradicting what we observed in the experiments. Therefore, an additional, unaccounted-for optical force must exist to reconcile the contradiction and dictate the particles' electrodynamics. We hence propose the inclusion of a *transverse scattering force* (TSF) in our model, as a result of the Si nanoparticles' photonic Hall effects.

As the name suggests, the TSF is a result of a biased scattering, in which the momentum carried away by the scattered radiation is counteracted by this reaction as per the law of conservation (see Fig. 4.3A). Therefore, the particles' scattering effects, especially in the cases of near- or on-resonance optical trappings, are of crucial importance. Peculiar attention should be given to Si nanoparticles in that, as previous studies point out, the photonic Hall effects make them scatter light differently based on the light's polarization states and the matter's refractive index gradients [83, 84, 85, 86, 87, 88]. Our further examination reveals two additional aspects – i.e., applied field and local field gradient – of the photonic Hall effects on Si nanoparticles, which are key factors in regulating the magnetic field trappings and can be demonstrated in the following simulation. Figure 4.3B simulates a tightly focused Gaussian with linear polarization where the electric and magnetic fields polarize in x- and y-direction, respectively. When placing the 205 nm Si nanoparticle at three representative

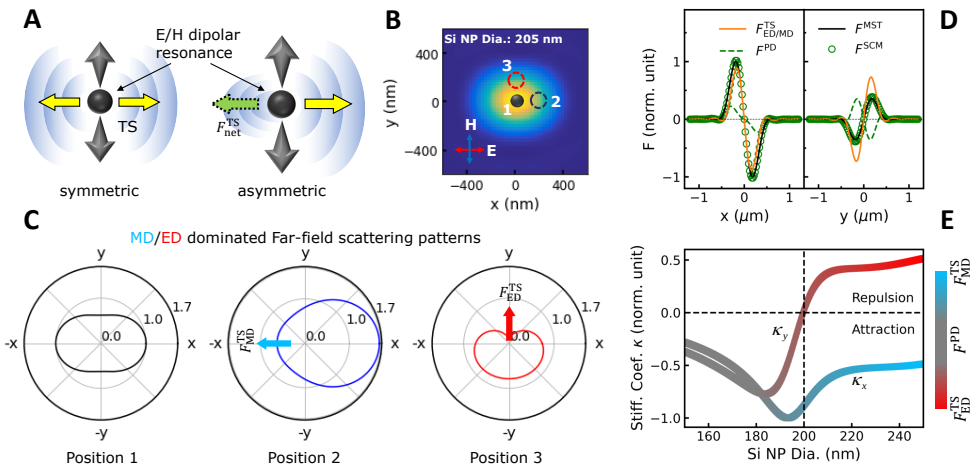

Figure 4.3: **Investigation of transverse scattering force due to Si nanoparticles' photonic Hall effect.** **(A)** Schematic diagram generalizes the Mie transverse scattering (TS) from a Si nanoparticle that is excited near its E/H dipolar resonance. Did its symmetric scattering (left) become asymmetric (right), a net force $F_{\text{net}}^{\text{TS}}$ arises to balance the momentum carried away by the biased fields in the opposite direction. **(B)** The photonic Hall effect in an exemplary Si nanoparticle (Dia.=205 nm) is demonstrated by characterizing its scattering properties at three designated positions (as labeled) in a linear-polarized, tight-focused Gaussian beam. **(C)** Normalized far-field radiation patterns of the Si nanoparticle at the different locations reveal that it scatters light differently depending upon the polarization states and intensity gradient of the exciting electric and magnetic fields, which follows the nature of photonic Hall effect. **(D)** Optical forces exerted on the Si nanoparticle calculated at various positions along x- and y-direction with four methods including transverse scattering (TS), point-dipole (PD) approximation, Maxwell stress tensor (MST), and scattering corrected model (SCM). Note, all forces are normalized to the maximum of the MST-calculated force. **(E)** Trapping stiffness coefficients of the Si nanoparticle in x- and y-direction for its various diameters. The color is encoded to indicate the prime contribution transitioning from dipole force to transverse scattering force as particle's dimension increases. The positive κ_y reflects a repulsion that repels the particle away from the central area of the Gaussian beam in the y-direction.

positions in the trapping field, one acquires three typical far-field scattering patterns shown in Fig. 4.3A. The scattering pattern of the particle at the origin displays a mirror symmetry, which means that no net TSF is generated. It is important to note that the light scattering originates mostly from both the ED and MD radiations. The excited dipole moments align with their respective exciting fields and radiate electromagnetic fields transversely (see Fig. 4.3A). This phenomenon explains why the particle scatters more intensely on the x-axis

due to its stronger MD mode (refer to Fig. 4.1C).

The mirror symmetry of the scattering is lost when the particle deviates from the "field axes," which refers to the axes of symmetry for both the intensity profile and polarization state of the field. The x- and y-axes serve as the field axes for the electric and magnetic components of the Gaussian beam, respectively. When the particle is placed at position 2, its deviation from the magnetic field axis leads to a breaking of field symmetry and affects the MD-mediated scattering in the x-direction. Similarly, the asymmetric ED-mediated scattering at position 3 is due to the particle's displacement from the electric field axis. However, these two configurations show different bias in scattering, with the ED mode scattering light along the local field gradient and the MD mode scattering light in the opposite direction, which is a manifestation of the photonic Hall effect in Si nanoparticles.

The nature of TSFs is a derivative of the biased scatterings. Based on the scattering tendencies related to the exciting fields, a general rule can be deduced: *MD-mediated TSFs (F_{MD}^{TS}) attract particles into magnetic field maxima, while ED-mediated TSFs (F_{ED}^{TS}) repel particles away from electric field maxima.* Numerically solving the net momentum carried by the unevenly scattered radiations leads to quantifying the TSFs [82]. In Fig. 4.3D, the TSFs were measured for the particle at various positions along the electric (left, x) and magnetic (right, y) field axes. The quasi-anisotropy, i.e., being attractive and a repulsive along the orthogonal axes, features the dipole-based scattering forces.

The optical forces, computed using both the Maxwell stress tensor (MST, in black) and point-dipole model (PD, in green dash), are also presented in addition to the TSFs. Comparing these forces explicitly reflects the significance of TSFs when optical trapping occurs in the optical resonant regime (see fig. S8 to examine thoroughly). Among them, the MST-computed forces accurately reflect the actual optical forces experienced by the particle. This is because the MST rigorously represents the particle's electromagnetic response by solving the full set of Maxwell's equations and the Lorentz force. The substantial discrepancies

between the MST-computed forces and the PD-computed forces highlight the inadequacy of the conventional point-dipole model in describing the particle's electrodynamics. Only by taking into account the TSFs can these misinterpretations be rectified (green circle). The resulting "Scattering Corrected Model" (SCM) is therefore deemed suitable for interpreting the electrodynamics of resonant optical trapping [82].

Leveraging the SCM to analyze the trapping efficiency for Si nanoparticles of varying sizes leads to comprehensively understanding the impact of the scattering force on magnetic field trapping. Figure 4.3E shows the trapping stiffness coefficients along the electric and magnetic field axes as a function of particle dimensions. The encoded colors indicate the shift in dominant force contribution from the dipole force (F^{PD}: gray) to the ED/MD-mediated TSF ($F^{\mathrm{TS}}_{\mathrm{ED}}/F^{\mathrm{TS}}_{\mathrm{MD}}$: red/blue) as optical resonances become pronounced (as seen in Fig. 4.1C). From the plots, two key observations can be made. Firstly, near the magnetic dipole resonance (vertical black dashed line), $|\kappa_x|$ reaches its minimum value while $|\kappa_y|$ is nearly zero, indicating that particles in this region are primarily controlled by the MD-mediated TSF. Secondly, as the particles grow larger, $|\kappa_x|$ and $|\kappa_y|$ become comparable in magnitude but with opposite signs, meaning that particles will experience commensurate attraction and repulsion from the magnetic- and electric-mediated TSFs in orthogonal directions, respectively.

The above summarized fundamental properties of the TSFs allow us to unravel the mechanism of the magnetic field trapping by schematically decomposing optical force exerted on a Si nanoparticle under illumination from an azimuthal beam, as shown in Fig. 4.4A. When the particle is excited near its magnetic dipole resonance, its being attracted toward the magnetic field maximum is primarily attributed to the $F^{\mathrm{TS}}_{\mathrm{MD}}$ (upper panel). As the particle with larger dimensions is excited beyond the magnetic dipole resonance peak, it experiences not only confining forces due to magnetic fields, but also a repulsion from the $F^{\mathrm{TS}}_{\mathrm{ED}}$ activated by the azimuthally polarized electric field, pushing it towards the beam center (lower panel).

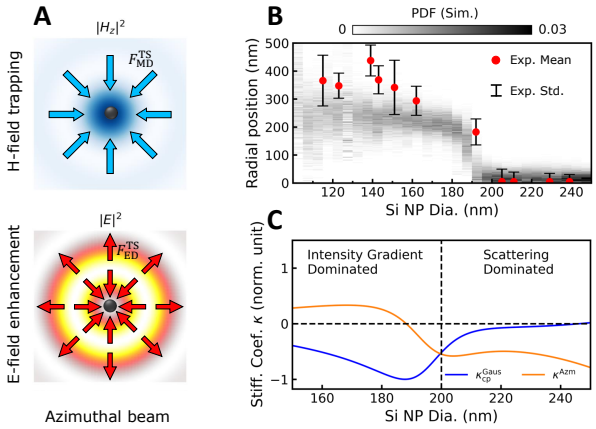

Figure 4.4: **Force analysis of Si nanoparticle trapped in the azimuthal beam for establishing optically magnetic trapping mechanism.** **(A)** The mechanism for an azimuthal beam stabilizing Si nanoparticles at its center principally relies on the magnetic field scattering force $F_{\mathrm{MD}}^{\mathrm{TS}}$ actuated by the magnetic field of H_z. This inward optical force drives particles to the most intense H_z region (upper panel). The electric scattering force $F_{\mathrm{ED}}^{\mathrm{TS}}$ actuated by the electric field E enhances the trapping stability by repulsion (lower panel). Note, this enhancement force is bi-directional on each side of the ring profile; therefore, the enhancement force itself will not be able to confine Si nanoparticles as firmly as the magnetic field scattering force $F_{\mathrm{MD}}^{\mathrm{TS}}$. **(B)** Radial distribution map of Si nanoparticles trapped in the azimuthal beam is plotted as a function of their diameters, ranging from 100 nm to 250 nm at a step of 5 nm. Experimental radial distributions of Si nanoparticles with selected dimensions are incorporated for comparison. **(C)** Comparison of the trap stiffness coefficient of different-sized Si nanoparticles trapped in azimuthal κ^{AZM} and circularly polarized Gaussian $\kappa_{\mathrm{CP}}^{\mathrm{Gaus}}$ beams provide a guidance of beam selection for trapping particles in the two distinct trapping regimes.

This is why both 205 nm and 239 nm Si nanoparticles were trapped at the induced magnetic field extreme, with the latter showing a tighter confinement. More quantitative details of the underlying mechanism can be found in fig. S10-12.

To gain a landscape of magnetic field trappings associated with Si nanoparticle's optical resonances, a radial position distribution map, as a function of particle diameters, was generated through GMT-Langevin dynamic simulations, as depicted in Fig. 4.4B. As expected, the simulation result indeed reveals an abrupt transition from electric field trapping to magnetic field trapping near the magnetic dipole resonance (Dia.=200 nm). Moreover,

The trapping efficiency unsurprisingly gets enhanced as reflected by the gradual decrease in the standard deviations of the distributions. Additionally, several experimental data from Si nanoparticles of various dimensions are incorporated for comparison and generally match the simulated trapping tendencies, further confirming the validity of our force analysis.

With this newfound mechanism of optical magnetic trapping, one can immediately recognize its advantage in constructing stable optical traps at or near trapping targets' optical resonances, despite the scattering forces being a "destroyer" for stable optical trap formations, as pointed out by the Earnshaw theorem. Dynamic simulation results, comparing the trapping stiffness of differently sized Si nanoparticles trapped in an azimuthal beam (κ^{Azm}) and a circularly polarized Gaussian beam ($\kappa_{\mathrm{cp}}^{\mathrm{Gaus}}$) in Fig. 4.4C, reveal that while the Gaussian beam provides stable trapping conditions for particles in the off-resonance domain, its performance degrades dramatically thereafter. In contrast, the azimuthal beam based on field-mediated scattering effects outperforms in the resonance domain. This outperformance will expand particle selection beyond the limits of small dimensions and low-index materials in order to detune the particles' optical resonances relative to laser frequencies, potentially benefiting relevant research areas, such as optical levitation, which is currently limited to the use of small-sized silica nanoparticles [89].

We have successfully shown the azimuthal beam trapping of Si nanoparticles to experimentally corroborate particle manipulations with magnetic field in optical frequencies for the first time. The failure to accurately explain the experimentally observed particles' electrodynamics with the point-dipole model led us to identify the ED- and MD-mediated TSFs and recognize their unique properties following Si nanoparticles' photonic Hall effect. Based on this breakthrough, we developed the SCM, enabling us to determine the TSFs' quantities via numerical computations and uncover the underlying principle of optical magnetic trapping. Although, in this work, the contributor to achieving the optical magnetic trappings is the scattering-type forces, it could be possible to realize the same phenomena with mag-

netic gradient forces if the trapped particles' electric and magnetic dipole resonances were well-separated since their MD had a greater strength even in the off-resonance regime. We predict that this proof-of-principle experiment could be accomplished by utilizing man-made meta-atoms [90]. Furthermore, this work provides a new platform to study many-body effects and optical matter formations resulting from magnetic light-matter interactions, whose mechanisms and scenarios remain largely unknown and warrant further exploration in the near future. Additionally, we have pointed out that under illumination of a nonuniform beam with linear polarization, the dipole-governed scattering forces exhibit quasi-anisotropy which can be leveraged to design optical-driven mechanical systems for a variety of applications such as particle sorting and optical conveyors as well as optofluidic wells.

CHAPTER 5

INTERACTIONS BETWEEN OPTICAL ELECTRIC AND MAGNETIC MODES IN DIELECTRIC NANOPARTICLES AND IMPERFECT MIRROR IMAGES

5.1 Introduction

The ability of metallic particles and structures, particularly ones based on noble metals, to manipulate light in the nanoscale regime has been deeply studied due to the numerous benefits and advances to be found in applications such as metamaterials, metafluids, sensing, solar energy collection, and nonlinear optics [3, 90, 91, 92, 93, 94, 95]. However, these metallic nanophotonic systems exhibit the serious drawbacks of dissipative loss and heating, so as a result a gradual shift to using semiconductor nanoparticles as building blocks for nanophotonic systems is taking place [7, 91, 96].

At the visible range of the electromagnetic spectrum, certain semiconductors have a large band gap and act as a dielectric medium with high index of refraction [96]. When these high index semiconductors are fabricated into nanoparticles with the correct particle dimensions, incident light can induce a circulating displacement current that gives rise to a large magnetic dipole and a strong magnetic response [21]. This feature opens up the possibility of manipulating magnetic light-matter interactions in order to promote specific photonic behavior [97, 98]. Furthermore, the facile manipulation of the overall photonic behavior of the nanoparticle by simply altering the dimensions and composition demonstrates that high index semiconductor nanoparticles are formidable building blocks for nanophotonic systems [91, 92, 96, 99, 100].

Now, despite the strong magnetic response of high index nanoparticles, they can still exhibit a comparable electric dipole Mie resonance that partially spectrally overlaps with the magnetic dipole mode [98]. One method to suppress the emission from the electric

dipole mode is to pair the nanoparticle with its electromagnetic mirror image—a concept from the method of image charges [13]. Essentially, the nanoparticle will be brought close to a conducting metal film (i.e. a mirror), and the induced electric and magnetic dipole moments in the nanoparticle will induce similar dipole moments (i.e. mirror images) in the metal film that will recursively interact with the nanoparticle [101, 102]. Due to the orientation of the electric and magnetic dipole moments of the nanoparticle and mirror images, the emission from the electric dipole can be reduced, while the magnetic field at the interface is enhanced [101, 103].

In fact, the combination of an optically magnetic high index nanoparticle with a conducting substrate has been widely explored in order to modify the photonic behavior of the nanoparticle or to induce new polariton phenomena. For example, the nanoparticle in combination with a conducting substrate or film can form a highly efficient antenna, capable of absorbing incident light over a large bandwidth [104, 105]. Once captured, the incoming electromagnetic radiation can be concentrated into the gap region between the nanoparticle and substrate for applications such as surface-enhanced Raman spectroscopy (SERS), or transmitted into the substrate as a surface wave with high directionality [105, 106]. Furthermore, the gap mode of the high index nanoparticle and conducting substrate system has the ability to couple to any fluorescent material present in the gap, increasing the photoluminescence rate without any of the loss or extinction normally attributed to plasmonic metal nanoparticles [92, 107, 108].

Given the wide use of a conducting substrate as a means of modifying the photonic behavior of optically magnetic nanoparticles, attempts have been made to create a theoretical framework to describe the interaction between the substrate and the optically magnetic nanoparticle based on the method of mirror images [101, 102, 109, 110, 111]. From basic electromagnetism, the method of mirror images indicates that when an electric charge or magnetic dipole distribution is placed near a semi-infinite conducting medium, the system

is mathematically similar to the original distribution and it's mirror image in place of the conducting medium (See Figure 5.1) [13, 112]. Extending this concept to the nanoparticle on a conducting surface, this system can be considered as consisting of just the original nanoparticle interacting with its mirror image [101, 102]. This approach has been used to explain new photonic behavior such as new scattering modes [101, 110], polarization-dependent scattering behavior [109, 111], and new forms of the magnetoelectric effect [113].

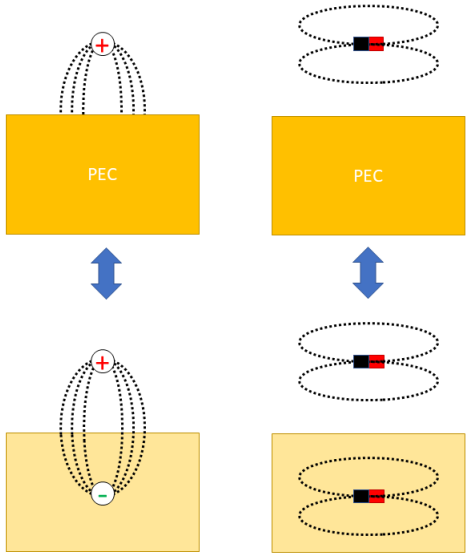

Figure 5.1: Cartoon representation of the method of mirror images. Near a perfect electric conductor (PEC), the fields of an electric charge and a parallel magnetic dipole **(Top Row)** are analogous to the fields of the same charge and dipole with the corresponding mirrored charge and dipole in place of the PEC **(Bottom Row)**.

However, the method of mirror images is based on the idea that the substrate is a perfect conductor and that the charge carriers of the conductor respond immediately to an external field without any retardation or dissipation [13, 112]. In contrast, many common metals used for plasmonics, such as copper, gold, and silver, have a large but finite conductance [45]. At optical frequencies, these metals would exhibit small, but nonzero, dissipative losses, phase delay, and skin depth [13]. Furthermore, when the method of mirror images is invoked to describe interactions between optically magnetic high index nanoparticles and conducting

substrates, frequently a qualitative description is given [101, 110, 102, 109].

Thus, the goal of this project is to quantitatively explore the effects of a substrate with finite conductivity on the behavior of a nanoparticle and conducting substrate nanophotonic system using the method of mirror images. First, a simple system consisting of a high index nanoparticle on a conducting metallic film will be fabricated. Then the photonic behavior of the system will be explored using optical scattering experiments and electrodynamic simulations, and the effect of the substrate will be analyzed using the method of mirror images. Due to the fact that the high index nanoparticle posses both electric and magnetic Mie resonances, the effect of the substrate due to magnetic and electric based phenomena may be analyzed simultaneously.

5.2 Simulation Methods

Towards analyzing the effect of the finite conductance of the substrate, two simulation methods were used: the finite-difference time-domain (FDTD) method and the software package SMUTHI [35].

The advantage of using FDTD stems from its versatility in simulating a wide variety of electromagnetic phenomena and photonic systems, as well as the ability to quickly calculate spectral information over a wide bandwidth after a single simulation in the time domain via the Fourier transform [37, 38]. In this Chapter, the three-dimensional (3D) software package, MEEP, was used for FDTD calculations [36].

Shown in Figure 5.2 is a typical high index nanoparticle on conducting substrate system simulated using MEEP. In this case, a 137 nm silicon nanoparticle was rendered on top of a 50 nm thick gold film, which was layered on top of a semi-infinite glass solid. The external environment was set to either vacuum or an optically dense medium, such as glycerol, and the incident light source was set to a plane wave. The materials and orientation of the system could be changed at ease, and instead of a gold film on glass substrate, a semi-infinite metal

solid may be rendered. Furthermore, a perfect electrical conductor (PEC) could be switched in place of the metal substrate, allowing the case of a high index nanoparticle with a perfect conducting substrate to be simulated.

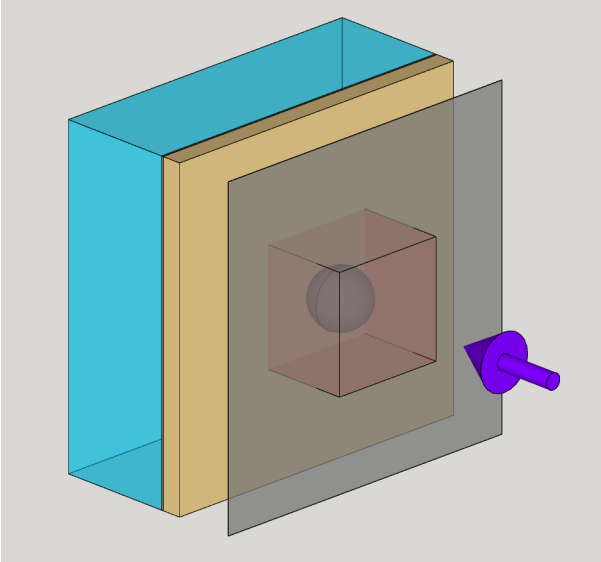

Figure 5.2: Schematic view of a nanophotonic system modeled in MEEP FDTD consisting of a high index silicon nanoparticle **(Grey Sphere)** on conducting gold film **(Gold Slab)** deposited on a semi-infinite glass solid **(Blue Slab)** with plane wave illumination **(Purple Arrow)**. Flux of scattered light is measured on a surface **(Red Box)** enclosing the nanoparticle, as well as through a plane behind the gold film and directly in front of the nanoparticle **(Grey Planes)**. System is bordered on all sides by absorbing layers (not shown here).

After much testing, the borders of the FDTD simulations were set to absorbing layers instead of perfectly matched layers (PMLs). PMLs are simulation constructs that gradually attenuate to zero any incoming radiation without reflection and are commonly used to enclose FDTD simulations since they mimic the scenario where scattered or emitted radiation is released into free space [36, 38]. Unfortunately, during testing it was discovered that evanescent waves created in dispersive media, such as gold, are not attenuated when they reach the PMLs, but instead grow to infinity. As such, absorbing layers, which have an absorbance that increases from zero to infinity from the front to the back of the layer, were

used. In principle, these absorbing layers prevent the finite simulation cell size from affecting the calculation of Maxwell's equations inside the cell by mimicking the scenario where emitted radiation can dissipate into free space. However, the absorbing layers have the downside of reflecting a fraction of incident radiation. This reflective property can be minimized by increasing the thickness of the layers and by setting the absorbance to gradually increase from the front to the back of the layer.

After testing and optimization, the FDTD mesh size was set to be 5 nm. This parameter was chosen to minimize the hardware requirements, while still obtaining converged FDTD results. The time step of the simulation, Δt, was determined by $\Delta t = S\Delta x$ where Δx is the mesh size in reduced units, and S is the Courant factor. A Courant factor of 0.5 was determined to provide good convergence of results. Unless noted later, the dielectric constants used for the metals and high index nanoparticle material were the ones that came default with the software package. Under these conditions, most FDTD simulations would take approximately two hours of real world time to finish when running on a home-build desktop machine with 128GB of RAM and a six-core processor (3.50 GHz).

In order to asses the spectral properties of the nanophotonic system, the flux of the scattered and incident light through different surfaces was measured. From the recorded flux, the scattering cross section may be calculated as follows,

$$\sigma_{\text{scatt}} = \frac{W_{\text{scatt}}}{I_{\text{src}}} \tag{5.1}$$

where W_{scatt} is the total power of the scattered field and I_{src} is flux (power per unit area) of the light incident on the nanophotonic structure. The surfaces for measuring the flux can be declared in arbitrary locations, and as shown in Figure 5.2, a planar surface would be set up in front of and behind the metal-film and nanoparticle system in order to measure the backward and forward scattering, as well as completely around the nanoparticle in order to measure the total scattering cross section.

The second simulation method used was the software package SMUTHI, which is designed to calculate the spectral properties of thin layers of arbitrary materials with user-defined, embedded nanostructures. Unlike FDTD, which involves numerically solving Maxwell's equations, SMUTHI is an analytical method based on the T-Matrix formalism and the Sommerfeld integrals [35]. Furthermore, the analytical method assumes that the layered medium consists of infinite layers (semi-infinite for the uppermost and bottommost layers and infinite in two dimensions for the other layers), so no surrounding absorbing layers or PMLs are required. The fact that the package is optimized to simulate nanophotonic structures on films of arbitrary material makes it highly suitable for this work.

Much of the same systems simulated with FDTD were also simulated using SMUTHI such as the silicon nanoparticle on a gold film on glass substrate (Figure 5.2). One subtlety that became apparent after testing was that converging results could not be obtained if the semi-infinite top and bottom layers were set to dispersive materials, such as metal. Thus, when a PEC or metal layer was used, it would be rendered as a layer of finite thickness on top of a semi-infinite dielectric substrate.

For the different materials present in simulations, the dielectric constants that came default with the generalized multiparticle Mie theory software package, MiePy, were used [33]. When running on the same desktop machine used for the FDTD simulations, the real world runtime of the simulations created with SMUTHI was on the order of minutes.

One major advantage of the SMUTHI simulations was that the spectral properties of individual Mie multipole modes may calculated. For example, the extinction cross section could be calculated for the overall electric and magnetic dipole moment of the silicon nanoparticle and gold film system shown in Figure 5.2. This feature would be utilized in understanding the fundamental cause of any substrate-induced phenomena.

5.3 Experimental Methods

To fabricate the nanophotonic system, gold was chosen as the conducting substrate due to ease of vacuum deposition as well as its non-reactivity. Silver is a better conductor than gold and more suitable for the construction of mirrors. However, Ag quickly reacts with oxygen and atmospheric sulfur dioxide, resulting in a dielectric layer of silver compounds, which would affect the photonic properties of a mirror made from Ag. As a result, Au was used to fabricate the substrate for the nanophotonic system. For the high index nanoparticles, silicon nanoparticles with diameters between 100-200 nm were utilized.

First, a glass coverslip was washed with ethanol and blow dried with N_2. Then 2 nm of Ti was deposited on top of the coverslip at a rate of 0.5 Å/s using an electron beam evaporator (AJA ATC-Orion 8E e-beam evaporation system) in order to assure adhesion between the Au layer and the glass substrate. Next, 50 nm of Au was deposited on top of the Ti layer at a rate of 1 Å/s using the electron beam evaporator. Once the Au film was fabricated, a polydisperse solution of silicon nanoparticles was shaken, sonicated for ~ 5 minutes, shaken again, and drop-casted on the Au film. The coverslip was then allowed to dry in a vacuum desiccator. Shown in Figure 5.3 are scanning electron microscope (SEM) and optical brightfield microscope images of a representative silicon nanoparticle on the gold film after the solution has dried.

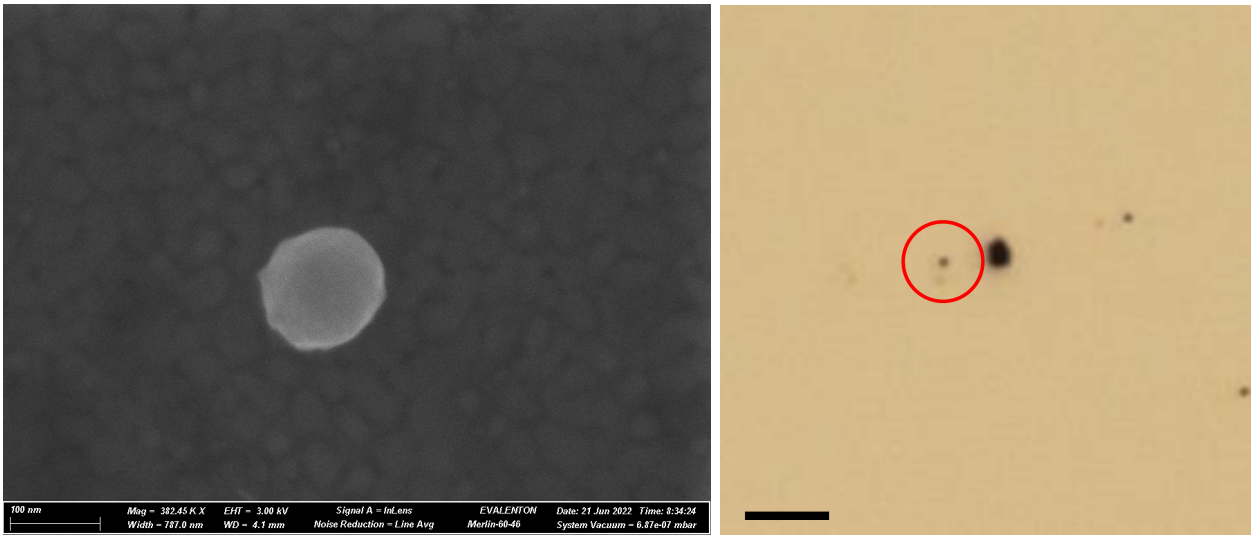

Figure 5.3: **(Left)** Scanning electron microscope image of 137 nm silicon nanoparticle on gold film. **(Right)** Brightfield optical microscope image of the same silicon nanoparticle **(Red Circle)** on the gold film. Scale bar is 2 μm.

After fabrication, the light scattering behavior of the nanophotonic system was probed using the optical setup shown in Figure 5.4. In summary, a suitable silicon nanoparticle was identified using brightfield microscopy. Then, a drop of glycerol was applied, as well as an additional glass coverslip so that the nanoparticle and gold film were sandwiched between two coverslips (see Figure 5.5). The sample was then mounted in the optical setup. A broadband laser light source was directed onto nanoparticle, and the scattered light was collected by an immersion objective and directed towards a spectrometer coupled to a CCD array detector.

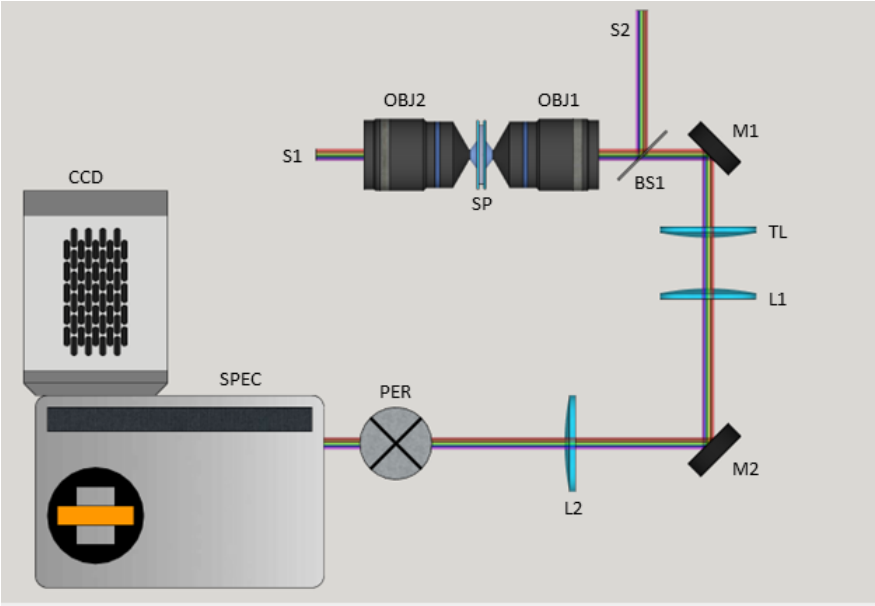

Figure 5.4: Experimental setup for scattering spectroscopy. For measurements in the transmission configuration, broadband laser light **(S1)** from a pulsed fiber-continuum laser is sent through an Olympus 100x oil immersion objective **(OBJ2)** towards the silicon nanoparticle and gold film sample **(SP)**. The scattered light is captured by a second Olympus 100x oil immersion objective **(OBJ1)** and directed by a mirror **(M1)** towards the spectrometer **(SPEC)** through a tube lens **(TL)** and a 4F system consisting of two lenses **(L1, L2)** and a mirror **(M2)**. After passing through a periscope **(PER)** and entering the spectrometer, the scattered light is recorded on a CCD array detector **(CCD)**. Note that for the transmission configuration, the 50:50 beamsplitter **(BS1)** is rotated out of the beam path. For measurements in the reflection configuration, broadband laser light **(S2)** from the same pulsed fiber-continuum laser is directed towards the Olympus 100x oil immersion objective **(OBJ1)** by the 50:50 beamsplitter **(BS1)** onto the sample. Backscattered light is collected by the same objective and directed towards the spectrometer in the same manner as the transmission configuration. For the reflection configuration, the second objective **(OBJ2)** is removed and the second broadband laser light path **(S1)** is not utilized.

In order to measure the forward and backward scattering, light from was collected from the top and bottom using two different objectives while the sample was flipped with respect to the incoming broadband laser. Thus, the sample was measured at four different configurations, summarized in Figure 5.5. The gold film was thick enough (50 nm) to reflect enough

light ($\sim$ 98% reflectivity at 800 nm) to act as an effective mirror, but still thin enough to allow sufficient light through for the transmission measurements ($\sim$ 2% transmission at 800 nm). During these measurements, the exposure time of the CCD detector needed to be adjusted and the broadband laser light attenuated in order to avoid saturating the detector. However, all other aspects of the measurement and the optical setup remained unchanged when switching between the different measurement configurations.

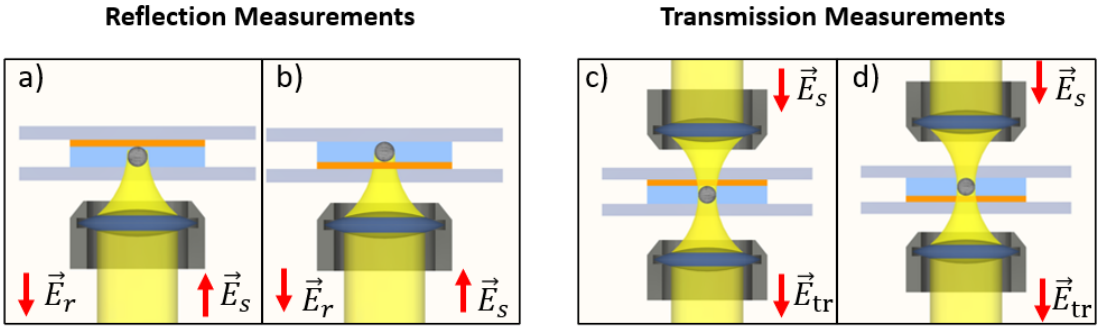

Figure 5.5: Orientations of silicon nanoparticle and gold film sample during the scattering spectroscopy measurements. For measurements in the reflection configuration, the sample was oriented so that the incoming broadband laser light would hit the silicon nanoparticle first and then the gold film **(a)**, as well as so that the incoming light would transmit through the gold film first and then fall incident on the nanoparticle **(b)**. In the same manner, for the measurements in the transmission configuration the sample was oriented so that the incoming laser light would transmit through the gold film first before falling incident on the silicon nanoparticle **(c)**, as well as so that the incoming light would hit nanoparticle first and then the gold film **(d)**.

5.4 Results

Before simulating the silicon nanoparticle on gold film system, the light scattering properties of a 137 nm silicon nanoparticle in air were simulated to ascertain the veracity of the simulation methods used. Both the MEEP FDTD and SMUTHI software packages were used, as well as the MiePy package. The results are summarized in Figure 5.6, where it can be seen that the total scattering from all three packages are in good agreement with each

other. In addition, the scattering per electric and magnetic dipole mode was calculated using SMUTHI and MiePy, with the results of both packages being in good agreement with each other (See Figure 5.6).

To test the simulation methods using the more pertinent case of a high index nanoparticle on a substrate, the scattering of a 137 nm silicon nanoparticle on a semi-infinite glass and silicon substrate was simulated. The resulting total scattering is summarized in Figure 5.6. For both cases, good agreement exists between the numerical MEEP and analytical SMUTHI packages.

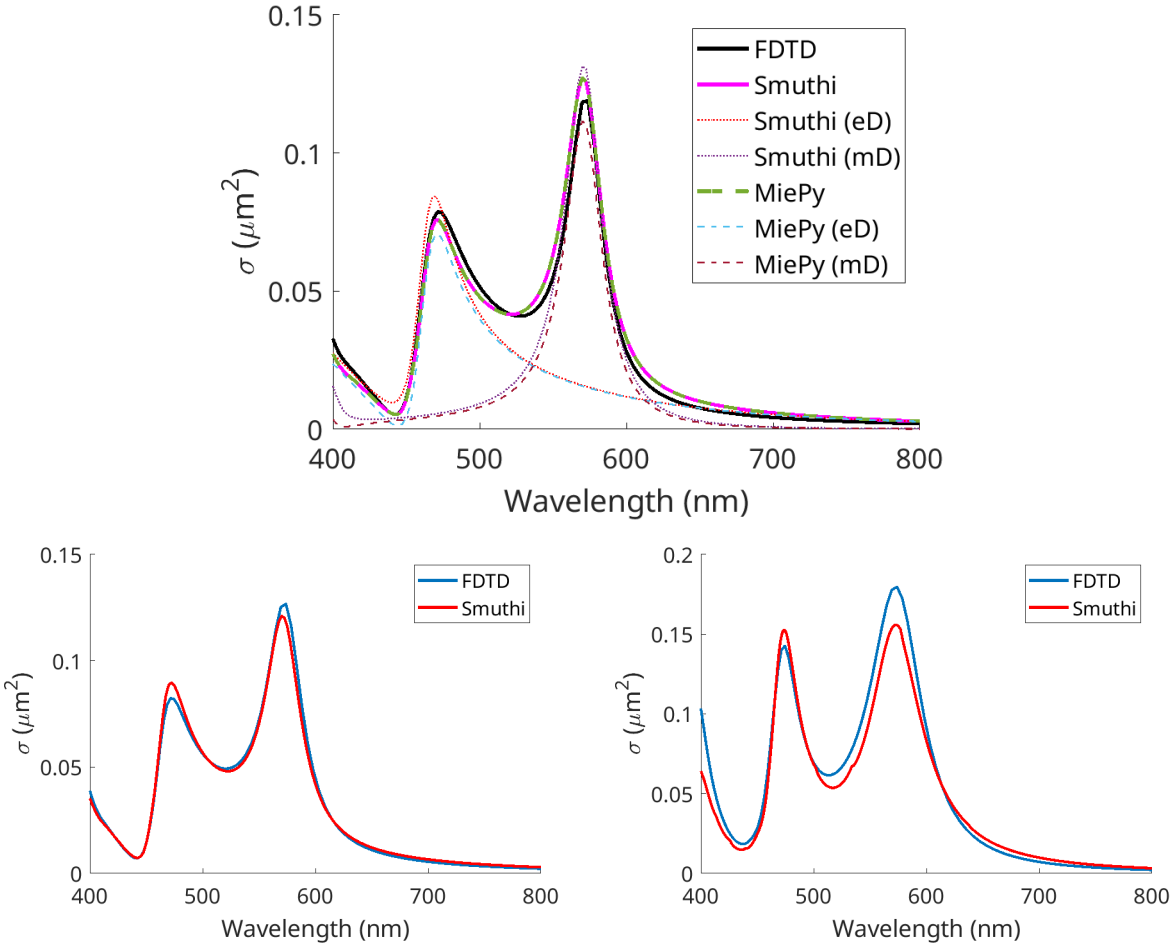

Figure 5.6: Scattering cross section simulations performed using MiePy, SMUTHI, and MEEP FDTD. **(Top)** Total scattering as well as scattering per electric and magnetic dipole mode for a 137 nm Si nanoparticle in air with no substrate. Total scattering for a 137 nm Si nanoparticle in air on a glass **(Left)** and silicon **(Right)** substrate.

After confirming the validity of the simulation methods, the light scattering properties of a high index nanoparticle with magnetic and electric resonance modes on both a perfect and imperfect mirror (conductor) were calculated. For the perfect case, a 137 nm silicon nanoparticle on a PEC substrate was simulated. For the imperfect case, a 137 nm silicon nanoparticle was instead simulated on a 50 nm thick gold film deposited on a semi-infinite glass substrate. The results are summarized in Figure 5.7. For the perfect case, two main peaks are observed at 478 nm and 573 nm. These peaks are at nearly the same locations as

the ones of the free particle (See Figure 5.6). However, the overall scattering cross section is greater, and the intensity of the peak at 573 nm is lower than the one at 478 nm, which is opposite to the free particle case. Furthermore when the total scattering of the nanoparticle on PEC substrate is decomposed into scattering per electric and magnetic dipole modes, it can be seen that both modes contribute to the intensity of the two main peaks. In contrast, with the free particle case the two main peaks in the total scattering are distinctly either magnetic or electric dipole in nature.

With regards to the imperfect case of a silicon nanoparticle on a gold film, two main peaks are also observed in the scattering spectrum, one at 484 nm and one at 585 nm. Unlike the perfect case with the PEC substrate, these peaks are shifted further away from the ones in the free particle case. Furthermore, when the scattering spectrum is decomposed into electric and magnetic modes, it is seen that both modes contribute to the intensity of the two main peaks, just like the perfect case. However, the scattering spectrum of the silicon nanoparticle on gold film is dominated primarily by the electric dipole mode, which deviates from the scattering behavior of the free particle, as well as the silicon nanoparticle on PEC case.

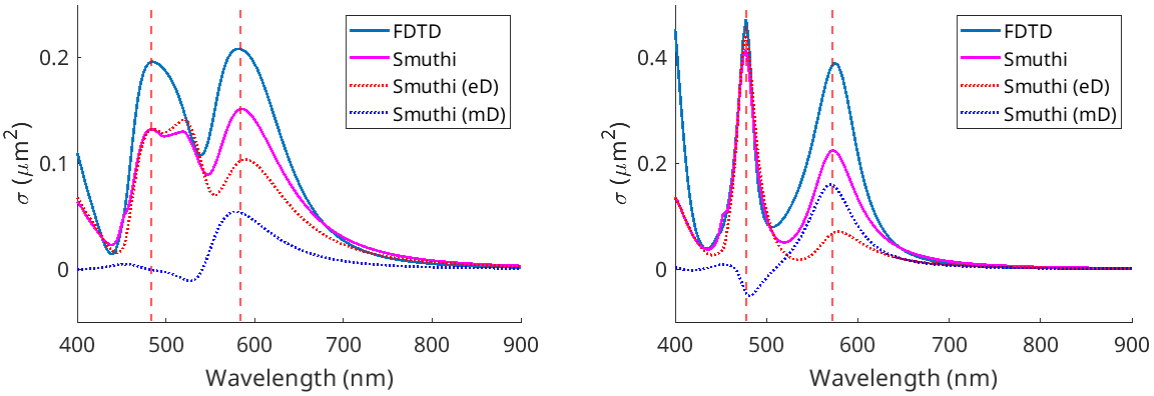

Figure 5.7: Total scattering cross section and scattering cross section per electric and magnetic dipole mode calculated for a 137 nm Si nanoparticle on 50 nm Au film on glass substrate **(Left)**, with peaks at 484 nm and 585 nm **(Red Vertical Lines)**, and a 137 nm Si nanoparticle on a perfect electrical conductor semi-infinite substrate **(Right)**, with peaks at 478 nm and 573 nm **(Red Vertical Lines)**. These calculations were performed using both the analytical SMUTHI and numerical MEEP FDTD packages.

In addition to the simulations, the scattering spectrum of the 137 nm silicon nanoparticle on a 50 nm thick gold film on glass substrate was experimentally measured. Both the scattering in the backwards and forwards directions were measured (See Figure 5.5) in order to quantify the total scattering as best as possible. To account for the spectral power distribution of the laser light source, the scattering spectra were normalized by the scattering spectrum of a bare region of the gold film. The results of the measurements are summarized in Figure 5.8.

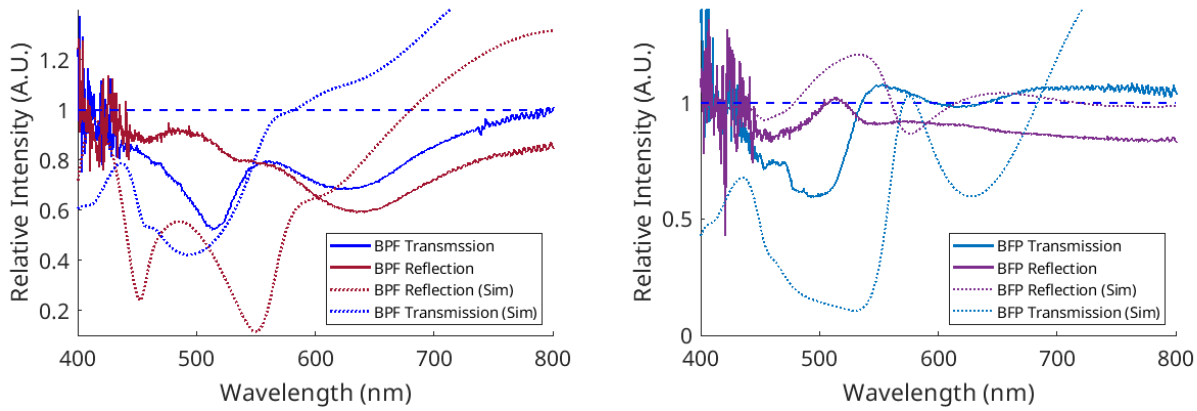

Figure 5.8: Experimentally measured scattering spectra *(Solid Lines)* of a 137 nm silicon nanoparticle on a 50 nm thick gold film on glass substrate, as well as numerically simulated scattering spectra *(Dotted Lines)*. **(Left)** Reflected and transmitted scattering for the case where source beam impinges on the nanoparticle first and then the Au film. **(Right)** Reflected and transmitted scattering for the case where the source beam transmits through the Au film first and then impinges on the nanoparticle. All spectra were normalized by the scattering of the bare gold film.

Based on the optical theorem [114], the presence of the silicon nanoparticle would scatter light away from the detection beam path for both the reflection and transmission configurations. Thus, any strong scattering resonances would manifest themselves as a decrease in recorded intensity. Since the scattering spectra are normalized with respect to a bare gold film, then a strong scattering resonance would appear as a large dip, as opposed to a peak, in the relative scattering intensity, whereas the lack of scattering resonances would appear as a relative intensity value close to unity.

For the experimental configuration where the incoming laser light source impinged upon the nanoparticle first and then the film, particularly strong resonances are observed around 638 nm for the reflection measurement and the 516 nm and 626 nm for the transmission measurement. The presence of the second dip at 516 nm in the transmission measurement suggests an anisotropy at this wavelength where the nanoparticle scatters only in the transmission (forward) direction.

Conversely, with the configuration where the incoming laser light transmitted through the gold film first and then impinged upon the nanoparticle, dips are seen at approximately 495 nm and 618 nm for the transmission measurement and at approximately 460 nm and 545 nm for the reflection measurement. Once again, the presence of dips in the transmission measurement and not the reflection measurement (and vice-versa) indicate an anisotropy in the scattering direction. Furthermore, the transmission measurement has peaks above unity at 553 nm and 687 nm, as also does the reflection measurement at approximately 515 nm. The presence of a relative intensity above unity indicates that the combination of the silicon nanoparticle and gold film together is more efficient at channeling light towards the detector than just the bare gold film alone. Thus at these wavelengths, there is a sort of anti-scattering regime for the nanoparticle and gold film system [115].

Also summarized in Figure 5.8 are the initial attempts made to compare the experimental scattering spectra with the numerically simulated ones. To mimic the experimental conditions, numerical simulations using MEEP FDTD were performed for the silicon nanoparticle on gold film system, but with the scattered flux measured through a plane directly in front and behind the nanoparticle and gold film (See Figure 5.2). Thus, the transmitted and reflected scattered light could be analyzed just as in the experiment. Furthermore, the simulated scattering spectra were also normalized by the transmitted and reflected spectra of a bare gold film without the nanoparticle. These resulting simulated scattering spectra show some resemblance to the experimental spectra (such as for the shape of the transmission scattering spectrum of the case where the light source transmits through the film to then impact the nanoparticle), but there are many differences which will be addressed in the following sections.

5.5 Discussion

Much of the groundwork for a full quantitative treatment of a high index nanoparticle with magnetic and electric resonances on a conducting substrate using the method of mirror images have been incrementally set up by previous authors, and in this section those different pieces will be brought together. The starting point would be to first consider the nanoparticle as a collection of point multipole moments [2, 13, 113]. Confining the analysis to just the visible regime and the initial multipole terms, the nanoparticle may be reduced to the induced electric and magnetic dipole moments,

$$\mathbf{p} = \epsilon_0 \alpha_E \mathbf{E}_t \tag{5.2}$$

$$\mathbf{m} = \alpha_H \mathbf{H}_t \tag{5.3}$$

where ϵ_0 is the vacuum permittivity and α_E and α_H are the dipole polarizabilities derived from the the scattering coefficients, a_1 and b_1, from Mie theory,

$$\alpha_E = \frac{6i\pi a_1}{k^3} \tag{5.4}$$

$$\alpha_H = \frac{6i\pi b_1}{k^3} \tag{5.5}$$

and where k is the wavenumber and $\mathbf{E}_t$ and $\mathbf{H}_t$ are the total electric and magnetic fields. The total field can be calculated numerically using FDTD or analytically as in [113].

The resulting scattered field from the effective magnetic and electric dipole moments of the nanoparticle can be then calculated using the Green's function approach. Since the nanoparticle is on a substrate, both the electromagnetic field from the nanoparticle that reflects off the substrate, as well as the one radiating directly from the particle into free space, need to be accounted for [2, 113]:

$$\mathbf{E}_{scatt}(\mathbf{r}) = \left[\hat{\mathbf{G}}_p^E(\mathbf{r},\mathbf{r}_0) + \hat{\mathbf{G}}_p^{E_r}(\mathbf{r},\mathbf{r}_0)\right]\mathbf{p} + \left[\hat{\mathbf{G}}_m^E(\mathbf{r},\mathbf{r}_0) + \hat{\mathbf{G}}_m^{E_r}(\mathbf{r},\mathbf{r}_0)\right]\mathbf{m} \tag{5.6}$$

$$\mathbf{H}_{scatt}(\mathbf{r}) = \left[\hat{\mathbf{G}}_p^H(\mathbf{r},\mathbf{r}_0) + \hat{\mathbf{G}}_p^{H_r}(\mathbf{r},\mathbf{r}_0)\right]\mathbf{p} + \left[\hat{\mathbf{G}}_m^H(\mathbf{r},\mathbf{r}_0) + \hat{\mathbf{G}}_m^{H_r}(\mathbf{r},\mathbf{r}_0)\right]\mathbf{m} \tag{5.7}$$

Both $\hat{\mathbf{G}}_j^E$ and $\hat{\mathbf{G}}_j^H$ are the dyadic Green's functions corresponding respectively to the electric and magnetic field scattered directly by the dipole moment ($j = p, m$) of the nanoparticle, and $\hat{\mathbf{G}}_j^{E_r}$ and $\hat{\mathbf{G}}_j^{H_r}$ are the dyadic Green's functions corresponding respectively to the electric and magnetic field scattered by the dipole moment ($j = p, m$) of the nanoparticle and then reflected off the substrate. The coordinate system is set with the z = 0 plane at the interface between the substrate and free space, with the origin at the point of contact between the nanoparticle and the substrate. The nanoparticle center is located at $\mathbf{r}_0 = z_0\hat{\mathbf{z}}$.

In the far-field regime with $|\mathbf{r}| \to \infty$, the dyadic Green's functions take on the following asymptotic forms [2, 113],

$$\hat{\mathbf{G}}_p^E = \frac{k^2}{\epsilon_0}\left(\frac{e^{ikr}}{4\pi r}e^{-ik(\mathbf{n}\cdot\mathbf{r}_0)}\begin{bmatrix} 1-\sin^2\theta\cos^2\phi & -\sin^2\theta\cos\phi\sin\phi & -\sin\theta\cos\theta\cos\phi \\ -\sin^2\theta\cos\phi\sin\phi & 1-\sin^2\theta\sin^2\phi & -\sin\theta\cos\theta\sin\phi \\ -\sin\theta\cos\theta\cos\phi & -\sin\theta\cos\theta\sin\phi & \sin^2\theta \end{bmatrix}\right) \tag{5.8}$$

$$\hat{\mathbf{G}}_p^H = -i\omega\left(ik\frac{e^{ikr}}{4\pi r}e^{-ik(\mathbf{n}\cdot\mathbf{r}_0)}\begin{bmatrix} 0 & -\cos\theta & \sin\theta\sin\phi \\ \cos\theta & 0 & -\sin\theta\cos\phi \\ -\sin\theta\sin\phi & \sin\theta\cos\phi & 0 \end{bmatrix}\right) \tag{5.9}$$

$$\hat{\mathbf{G}}_m^H = k^2\left(\frac{e^{ikr}}{4\pi r}e^{-ik(\mathbf{n}\cdot\mathbf{r}_0)}\begin{bmatrix} 1-\sin^2\theta\cos^2\phi & -\sin^2\theta\cos\phi\sin\phi & -\sin\theta\cos\theta\cos\phi \\ -\sin^2\theta\cos\phi\sin\phi & 1-\sin^2\theta\sin^2\phi & -\sin\theta\cos\theta\sin\phi \\ -\sin\theta\cos\theta\cos\phi & -\sin\theta\cos\theta\sin\phi & \sin^2\theta \end{bmatrix}\right) \tag{5.10}$$

$$\hat{\mathbf{G}}_m^E = i\omega\mu_0\left(ik\frac{e^{ikr}}{4\pi r}e^{-ik(\mathbf{n}\cdot\mathbf{r}_0)}\begin{bmatrix} 0 & -\cos\theta & \sin\theta\sin\phi \\ \cos\theta & 0 & -\sin\theta\cos\phi \\ -\sin\theta\sin\phi & \sin\theta\cos\phi & 0 \end{bmatrix}\right) \tag{5.11}$$

$$\hat{\mathbf{G}}_p^{E_r} = \frac{k^2}{\epsilon_0}\frac{e^{ikr}}{4\pi r}e^{ik(\mathbf{n}\cdot\mathbf{r}_0)}\left(r^s\begin{bmatrix} \sin^2\phi & -\cos\phi\sin\phi & 0 \\ -\cos\phi\sin\phi & \cos^2\phi & 0 \\ 0 & 0 & 0 \end{bmatrix} - r^p\begin{bmatrix} \cos^2\phi\cos^2\theta & \cos\phi\sin\phi\cos^2\theta & \sin\theta\cos\theta\cos\phi \\ \cos\phi\sin\phi\cos^2\theta & \sin^2\phi\cos^2\theta & \sin\theta\cos\theta\sin\phi \\ -\sin\theta\cos\theta\cos\phi & -\sin\theta\cos\theta\sin\phi & -\sin^2\theta \end{bmatrix}\right) \tag{5.12}$$

$$\hat{\mathbf{G}}_p^{H_r} = \omega k \frac{e^{ikr}}{4\pi r} e^{ik(\mathbf{n}\cdot\mathbf{r}_0)} \left(r^s \begin{bmatrix} \sin\phi\cos\phi\cos\theta & -\cos^2\phi\cos\theta & 0 \\ \sin^2\phi\cos\theta & -\sin\phi\cos\phi\cos\theta & 0 \\ -\sin\theta\sin\phi & \sin\theta\cos\phi & 0 \end{bmatrix} - r^p \begin{bmatrix} -\sin\phi\cos\phi\cos\theta & -\sin^2\phi\cos\theta & -\sin\theta\sin\phi \\ \cos^2\phi\cos\theta & \sin\phi\cos\phi\cos\theta & \sin\theta\cos\phi \\ 0 & 0 & 0 \end{bmatrix} \right) \tag{5.13}$$

$$\hat{\mathbf{G}}_m^{H_r} = k^2 \frac{e^{ikr}}{4\pi r} e^{ik(\mathbf{n}\cdot\mathbf{r}_0)} \left(r^p \begin{bmatrix} \sin^2\phi & -\cos\phi\sin\phi & 0 \\ -\cos\phi\sin\phi & \cos^2\phi & 0 \\ 0 & 0 & 0 \end{bmatrix} - r^s \begin{bmatrix} \cos^2\phi\cos^2\theta & \cos\phi\sin\phi\cos^2\theta & \sin\theta\cos\theta\cos\phi \\ \cos\phi\sin\phi\cos^2\theta & \sin^2\phi\cos^2\theta & \sin\theta\cos\theta\sin\phi \\ -\sin\theta\cos\theta\cos\phi & -\sin\theta\cos\theta\sin\phi & -\sin^2\theta \end{bmatrix} \right) \tag{5.14}$$

$$\hat{\mathbf{G}}_m^{E_r} = -\omega\mu_0 k \frac{e^{ikr}}{4\pi r} e^{ik(\mathbf{n}\cdot\mathbf{r}_0)} \left(r^p \begin{bmatrix} \sin\phi\cos\phi\cos\theta & -\cos^2\phi\cos\theta & 0 \\ \sin^2\phi\cos\theta & -\sin\phi\cos\phi\cos\theta & 0 \\ -\sin\theta\sin\phi & \sin\theta\cos\phi & 0 \end{bmatrix} - r^s \begin{bmatrix} -\sin\phi\cos\phi\cos\theta & -\sin^2\phi\cos\theta & -\sin\theta\sin\phi \\ \cos^2\phi\cos\theta & \sin\phi\cos\phi\cos\theta & \sin\theta\cos\phi \\ 0 & 0 & 0 \end{bmatrix} \right) \tag{5.15}$$

with ω being the electromagnetic frequency, μ_0 as the vacuum permeability, and $\mathbf{n}(\theta,\phi) = \mathbf{r}/r$ being the direction of field propagation. The Fresnel reflection coefficients, r^s and r^p, are given as follows [2, 113],

$$r_E^s(k_x, k_y) = r_H^p(k_x, k_y) = \frac{\mu_s k_z - \mu k_z^s}{\mu_s k_z + \mu k_z^s} \tag{5.16}$$

$$r_E^p(k_x, k_y) = r_H^s(k_x, k_y) = \frac{\epsilon_s k_z - \epsilon k_z^s}{\epsilon_s k_z + \epsilon k_z^s} \tag{5.17}$$

with $k_z(k_x, k_y)$ and $k_z^s(k_x, k_y)$ being the normal components of the wavevector of light outside and inside the substrate, respectively, and μ_s and ϵ_s being the relative permeability and permittivity of the substrate, respectively. The relative permeability and permittivity of the free space, μ and ϵ, are assumed to be unity.

Assuming the incoming light is a plane wave at normal incidence and after applying the dyadic Green's functions to Equations 5.6 and 5.7, the scattered electric field in the far-field regime in spherical coordinates is found to be as follows [2, 113],

$$\begin{bmatrix} E_\theta \\ E_\phi \end{bmatrix} = \frac{k^2 e^{ikr}}{4\pi\epsilon_0 r} \begin{bmatrix} \Phi^{(2)}(p_x \cos\phi + p_y \sin\phi)\cos\theta + \Phi^{(1)}(m_y \cos\phi - m_x \sin\phi)/c \\ \Phi^{(3)}(p_y \cos\phi - p_x \sin\phi) - \Phi^{(4)}(m_x \cos\phi + m_y \sin\phi)\cos\theta/c \end{bmatrix} \tag{5.18}$$

where the coefficient functions are as follows,

$$\Phi^{(1)} = e^{-ikz_0\cos\theta} + r^p e^{ikz_0\cos\theta} \tag{5.19}$$

$$\Phi^{(2)} = e^{-ikz_0\cos\theta} - r^p e^{ikz_0\cos\theta} \tag{5.20}$$

$$\Phi^{(3)} = e^{-ikz_0\cos\theta} + r^s e^{ikz_0\cos\theta} \tag{5.21}$$

$$\Phi^{(4)} = e^{-ikz_0\cos\theta} - r^s e^{ikz_0\cos\theta} \tag{5.22}$$

By inspection, it can be seen that the second exponential terms of the coefficient functions (Equations 5.19 - 5.22) are similar to the first exponential terms, with the only differences being the negation of the coordinate value, z_0, and the inclusion of the Fresnel reflection

coefficients. Thus, Equation 5.18 could be rewritten in the following form,

$$\begin{bmatrix} E_\theta \\ E_\phi \end{bmatrix} = \frac{k^2 e^{ikr}}{4\pi\epsilon_0 r} e^{-ikz_0\cos\theta} \begin{bmatrix} (p_x\cos\phi + p_y\sin\phi)\cos\theta \\ (p_y\cos\phi - p_x\sin\phi) \end{bmatrix} + \tag{5.23}$$

$$\frac{k^2 e^{ikr}}{4\pi\epsilon_0 r} e^{-ikz_0\cos\theta} \begin{bmatrix} (m_y\cos\phi - m_x\sin\phi)/c \\ -(m_x\cos\phi + m_y\sin\phi)\cos\theta/c \end{bmatrix} +$$

$$\frac{k^2 e^{ikr}}{4\pi\epsilon_0 r} e^{ikz_0\cos\theta} \begin{bmatrix} -r^p & 0 \\ 0 & r^s \end{bmatrix} \begin{bmatrix} (p_x\cos\phi + p_y\sin\phi)\cos\theta \\ (p_y\cos\phi - p_x\sin\phi) \end{bmatrix} +$$

$$\frac{k^2 e^{ikr}}{4\pi\epsilon_0 r} e^{ikz_0\cos\theta} \begin{bmatrix} r^p & 0 \\ 0 & -r^s \end{bmatrix} \begin{bmatrix} (m_y\cos\phi - m_x\sin\phi)/c \\ -(m_x\cos\phi + m_y\sin\phi)\cos\theta/c \end{bmatrix}$$

or in short,

$$\mathbf{E}_{scatt} = -\mathbf{E}_p + \mathbf{E}_m - \hat{\mathbf{R}}\mathbf{E}'_p - \hat{\mathbf{R}}\mathbf{E}'_m \tag{5.24}$$

where $\mathbf{E}_p$ and $\mathbf{E}_m$ are the fields of the electric and magnetic dipole in free space and $\mathbf{E}'_p$ and $\mathbf{E}'_m$ are the fields of an identical electric and magnetic dipole, just shifted by $2z_0$ distance along the z-axis towards the substrate and with the phase and amplitude adjustments embodied in the operator, $\hat{\mathbf{R}} = \begin{bmatrix} -r^p & 0 \\ 0 & r^s \end{bmatrix}$.

With Equation 5.24 in mind, the case of a high index nanoparticle on top of a perfectly conducting substrate can be considered. For this substrate, the Fresnel reflection coefficients

take on the following form,

$$\hat{\mathbf{R}} = \begin{bmatrix} -r^p & 0 \\ 0 & r^s \end{bmatrix} = \begin{bmatrix} -1 & 0 \\ 0 & -1 \end{bmatrix} \tag{5.25}$$

$$= -\hat{\mathbf{I}} \tag{5.26}$$

with the scattered field now as,

$$\mathbf{E}_{scatt} = -\mathbf{E}_p + \mathbf{E}_m + \mathbf{E}'_p + \mathbf{E}'_m \tag{5.27}$$

which is just the original dipole moments of the nanoparticle, together with mirror copies of those dipoles shifted away by the distance $2z_0$. Thus it can be seen that the underlying physical picture for the simulation of the silicon nanoparticle on the PEC substrate shown in Figure 5.7 is that of the original dipole moments of the nanoparticle interacting with their mirror images.

The picture changes when the case of a good, but not perfect, conducting substrate is considered. Because of the finite conductivity and dispersive properties of the substrate, the Fresnel coefficients do not reduce to positive and negative unity, resulting in the Fresnel reflection coefficient operator being $\hat{\mathbf{R}} = \begin{bmatrix} -r^p & 0 \\ 0 & r^s \end{bmatrix}$, where r^p and r^s are complex numbers with absolute values varying from 0 to 1 (for most metals in free space). Applying the operator, $\hat{\mathbf{R}}$, back to Equation 5.24, we see that the effect of the tensor products, $\hat{\mathbf{R}}\mathbf{E}'_p$ and $\hat{\mathbf{R}}\mathbf{E}'_m$, is to reduce the amplitude of the electric and magnetic image dipoles, respectively, as well as to shift the phase of those same dipoles with respect to the original dipole moments.

As such, the image dipole moments in Equation 5.24 are not perfect mirror images of the original dipole moments when the substrate is a good, but not perfect, conductor. As summarized in Figure 5.9, the system of electric and magnetic dipole moments next

to the conducting substrate can still be considered as a system of electric and magnetic dipoles interacting with their image dipole moments. However, the phase and amplitude of those image dipole moments are modified by the operator, $\hat{\mathbf{R}} = \begin{bmatrix} -r^p & 0 \\ 0 & r^s \end{bmatrix}$, with the Fresnel reflection coefficient values determined by the properties of the substrate (i.e. the permeability and permittivity).

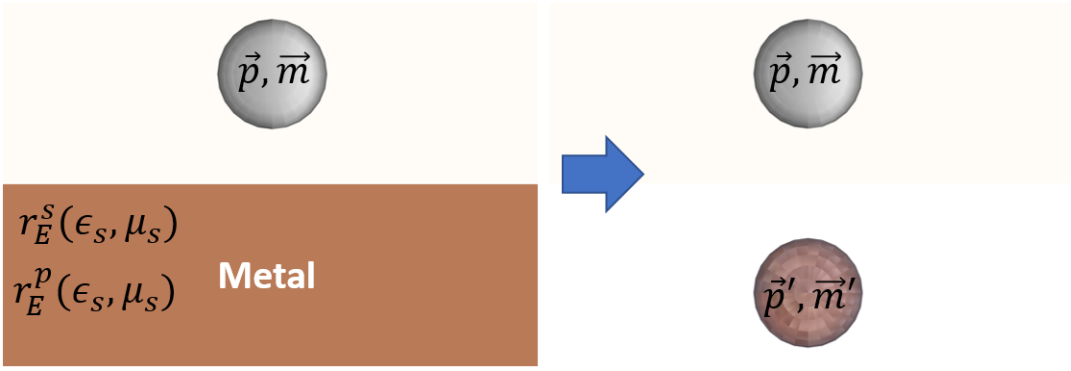

Figure 5.9: Cartoon representation of the method of mirror images generalized to account for the finite conductivity of mirror substrates made from real world metals. A nanophotonic structure with electric and magnetic dipole moments, $\vec{p}$ and $\vec{m}$, on a conducting substrate with permittivity and permeability, ϵ_s and μ_s, can be reduced to the same nanophotonic structure with its original dipole moments, $\vec{p}$ and $\vec{m}$, interacting with image dipole moments, $\vec{p}'$ and $\vec{m}'$, that are modified in amplitude and phase by Fresnel reflection coefficients, r_E^s and r_E^p.

It is believed that this physical picture is explanation behind the the scattering of the silicon nanoparticle on the gold substrate system summarized in Figures 5.7 and 5.8 and that it also explains the difference in scattering between the silicon nanoparticle on a PEC substrate and the silicon nanoparticle on a gold substrate shown in Figure 5.7. Essentially, the substrate supports a set of image dipoles, which interact with the original dipole modes of the nanoparticle. If the substrate is a perfect conductor, then the image dipoles have the same amplitude magnitude as and are in phase (or antiphase) to the original ones (similar to the situation in Figure 5.1). Then, the electromagnetic fields from both sets of dipoles

constructive and destructive interfere to give the scattering shown in Figure 5.7. However, if a substrate with a finite conductivity is used, such as gold, then the image dipole amplitude magnitude and phase are attenuated and adjusted, respectively. The electromagnetic fields of the image dipoles would then interfere differently with the fields of the original dipoles, giving rise to a new scattering spectrum, as shown in Figure 5.7. In fact, depending on the phase difference between the two sets of dipole modes, it is believed that a Kerker effect is possible and that the interference between the two sets of dipoles gives rise to the anisotropic scattering observed in Figure 5.8 [116].

To test these ideas, the scattering spectra can be calculated from the electric and magnetic dipole modes of the nanoparticle and the corresponding mirror images. First, the nanoparticle dipole moments were obtained using the procedures described by Ref. [113]. From these dipole modes, the image dipoles may be calculated using the generalized mirror image framework described in Equations 5.18 to 5.24. Using the same framework, the scattered electromagnetic field and the total power of the scattered field can be calculated. After dividing the scattered field power by the source beam flux (as in Equation 5.1), the scattering spectrum may be obtained. By obtaining the same scattering spectra as shown in Figure 5.7 using this outlined approach, the cause of the scattering behavior of the nanoparticle on gold film system may be attributed to the interference between the original nanoparticle electric and magnetic dipole modes and their corresponding image dipoles, modified by the substrate.

During this process, many difficulties arose in calculating the electric and magnetic dipole moments. This step required numerical integration, as described in Ref. [113], and it was challenging achieving convergence despite the use of popular scientific integration software packages [117]. Shown in Figure 5.10 is a representative result of attempting to calculate the scattering spectra of the electric and magnetic dipole modes of the nanoparticle and gold film system using the generalized mirror image approach just described. The effect of non-

convergence in the numerical integration, required for obtaining the electric and magnetic dipole moments, would appear as discontinuities in the scattering spectra, as can be seen in Figure 5.10. Addressing these numerical issues are part of the future directions that will be discussed in the next section.

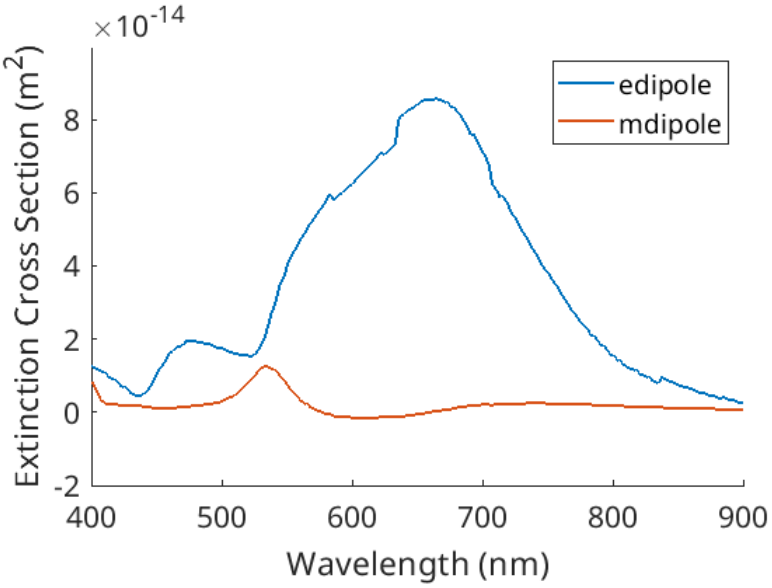

Figure 5.10: Scattering spectrum of the electric and magnetic dipole modes of a 137 nm Si nanoparticle on gold substrate system, calculated using the generalized mirror image approach (Equations 5.18 to 5.24). Effects of non-convergence in the numerical integration can be see in the discontinuities at 583 nm, 634 nm, 710 nm and 836 nm.

5.6 Conclusion and Future Work

In this Chapter, the effects of a good (but not perfect) conducting substrate on the photonic properties of a system consisting of a high index silicon nanoparticle with magnetic and electric Mie resonances on conducting substrate were explored. First, the system was investigated by simulating the scattered electromagnetic fields using using numerical methods, where Maxwell's equations were iteratively solved and propagated forward in time. In tandem, the fields were also simulated and examined using analytical methods based on Mie theory in order to understand the more fundamental aspects of the light scattering proper-

ties. A significant difference was observed in the total scattering behavior, as well as in the scattering contributions of the electric and magnetic dipole modes, when the substrate was set to gold, as opposed to PEC.

In addition to the simulations, the actual silicon nanoparticle on gold substrate system was fabricated. A 50 nm thick Au film was deposited, which was thick enough to act as an almost opaque mirror but still thin enough to let light through for transmission measurements. The scattering in the forwards and backwards direction was measured for the configuration where the light source transmitted through the film and then hit the nanoparticle, as well as for configuration where the light source hit the nanoparticle first and then the film.

A theoretical framework was drawn up that generalizes the method of mirror images to include mirrors composed of good (but not perfect) conductors. In this framework, the high index nanoparticle is treated as a collection of electric and magnetic point dipoles, and the effect of the substrate is to produce another set of dipoles that mirror the ones from nanoparticle. When a PEC substrate is assumed, then the theory recapitulates the textbook formalism for charge distributions and currents near a perfect conductor, and it is seen that the resulting field is the same as the combined fields of the original dipoles and the mirror image of those dipoles, shifted in space. However, if the substrate is not made from a perfect conductor, those image dipoles are attenuated and phase shifted with respect to the originals. The resulting interaction between the original dipoles and the phase shifted and attenuated ones is what gives rise to differences in scattering behavior between the silicon nanoparticle on PEC and the silicon nanoparticle on Au.

Now, it is to be noted that the experimental scattering spectra of the silicon nanoparticle on gold film differed significantly from the scattering spectra of the same system calculated through numerical simulations. This difference persisted even after the measurement configurations, limited light collecting abilities, and normalization procedures of the experiment were taken into account in the simulations. It is believed that two factors were responsible

for these results. The first relates to the relative permittivity values used for the materials in the simulations. It may be seen in Figure 5.3 that the gold substrate is quite granular, suggesting that the film is not a single crystal. As a result, the relative permittivity could differ significantly from the published permittivity values used, which were measured from films that were more crystalline [118]. Along the same lines, the presence of chemical residue on the surface is possible due to the manner in which the silicon nanoparticles were deposited on the gold film. The presence of residue would manifest itself as an additional layer of material with a relative permittivity different from gold. Finally, it was not possible at this time to measure how crystalline the silicon nanoparticle was. As a result, it is not clear whether the nanoparticle was composed primarily of amorphous or highly crystalline silicon, each with a different relative permittivity. This variance in relative permittivity values would strongly affect the photonic properties of the experimental silicon nanoparticle on gold film system and could result in very different scattering behavior than the one in simulation.

The other factor is the manner in which the numerical FDTD simulations were set up. As mentioned before, the simulation system boundaries were set to absorbing layers with an absorptivity that increases from zero to infinity from the inner to outer surface. These absorbing layers were used as opposed to the more commonly used PMLs because of the potential for evanescent waves to create non-physical fields in the PMLs. However, the absorbing layers have the tendency to partially reflect incident light resulting in artifacts in the overall simulation results. It is possible that the absorbing layers were inducing cavity-related effects on the nanoparticle and gold substrate system, resulting in an overall scattering behavior that was different from experiment.

Future work consists first in reconciling the experimental scattering results with the calculated spectra from simulation. Towards that goal, it is believed necessary to first experimentally measure the relative permittivity values of all materials in order to create an accurate system in simulation. The gold film permittivity would have to be measured, as

well as the permittivity of the silicon nanoparticle. In addition, the surface of the gold film would need to be washed without disturbing the nanoparticle or the Au surface in order to address the effect of the chemical residue layer.

To account for the issues pointed out with the FDTD simulation boundaries, the simplest solution is to use relatively thick absorbing layers. At very large or infinite thickness, the reflectivity of the absorbing layers approaches zero, and the effect of the layers on the scattering results becomes negligible. The primary downside to this approach is the memory and processing resources needed to run this simulation, which would increase with absorbing boundary layer thickness. One way to mitigate this drawback would be to use an adaptive mesh with fewer grid points inside the thick absorbing layers, thus reducing the number of calculations need to be completed with each timestep.

The most salient future direction for this work would be to investigate the anisotropy in the experimental scattering spectra of the silicon nanoparticle on gold film. As shown in Figure 5.8, the scattering properties of the system change when the system is flipped such that the light source transmits through the film before impinging upon the nanoparticle, as opposed to impinging upon the nanoparticle first and then reaching the film (see Figure 5.5 for the different configurations). In addition for both cases, the scattering spectra in the forward and backward directions are different. While only speculative investigations have been done, it is expected that the magnetic resonance modes of the silicon nanoparticle are behind the new scattering properties of the system. It is known from basic electromagnetism that the magnetic field acts on matter at right angles (e.g. see Equation 2.31) and that most magnetic-related phenomena mathematically involve a cross product, introducing chirality and anisotropy. Thus, it is believed that the interplay between the magnetic and electric resonances of the system is imparting new chiral properties into the scattering behavior and that the fundamental cause may be found from a close examination from the chiral magnetic field point of view.

CHAPTER 6

ENHANCING LANTHANIDE ION MAGNETIC DIPOLE TRANSITIONS USING NANOPARTICLE-BASED MIE RESONANCES

6.1 Introduction

Advances in plasmonics and nanostructure fabrication methods have allowed the manipulation of electromagnetic fields beyond the diffraction limit, as well as the fine control of light-matter interactions at the nanoscale [7, 91]. As a result, new opportunities have opened up for applications in areas such as sensing, photovoltaics, biomedical therapies, and nonlinear optics [3, 7, 91, 92]. Further research in this area has potential to produce results in even more novel areas such as cloaking [7, 119].

Of particular interest to Chemistry is the use of nanophotonics to manipulate the electronic states of atoms, as well as the HOMO-LUMO levels of molecules. Indeed, it has been demonstrated that cavities with high Q-factors have the ability to shift the energy levels in certain molecules to the point where the rates of isomerization can be manipulated [120, 121, 122], as well as to influence the reaction pathway and product outcome of unimolecular reactions [121, 123]. In general, a predominant feature of these works is strong coupling between molecules and a nanophotonic structure, such as a cavity. This strong coupling is characterized by a hybridization of the former molecular energy levels and cavity states to produce new molecular states with properties and energy levels different from the original molecular states [124, 120, 123]. Strong coupling is in contrast to weak coupling, which manifests itself in the increase or decrease of rates of change [124, 125, 126].

Much work involving strong coupling focus on an electric field mediated interaction, due in large part to the fact that magnetic dipole electronic transitions are orders of magnitude slower than electric dipole transitions [124, 22, 23]. However, recent work has been performed

which theoretically demonstrate the ability to create polaritons by manipulating the magnetic field of light [127, 128, 129, 130]. Furthermore, it was illustrated that the presence of a lattice of magnetic dipole scatterers can influence the local density of states of the surrounding area [127]. In addition, similar Purcell enhancements to the local density of states for magnetic dipole based electronic transitions have been calculated for a single dielectric particle with magnetic Mie resonances [129]. In particular, this last case is of interest due to the prominent role of magnetism in both the field-based coupling and the constituent elements of the system.

Experimentally, magnetic field based coupling has been explored in various photonic systems. First, the ability of the magnetic field component of light to drive electronic transitions was demonstrated in experiment [131]. Then the ability of simple nanophotonic structures such as mirrors to manipulate, in a local density of states fashion, magnetic dipole electronic transitions was experimentally explored [132, 133]. Finally, the magnetic field based coupling between the resonant modes of lattice photonic structures and electronic transitions was demonstrated [8, 134]

Indeed, while much work has demonstrated coupling between electronic transitions and nanophotonic structures, the goal of this project is to explore coupling based primarily on the magnetic field. In this case, the different elements of the system–the nanophotonic structure resonant modes, the field-based coupling, and the electronic transition–will be primarily magnetic in nature. Towards this end, the coupling between the magnetic Mie resonances of a spherical dielectric particle with high index of refraction, and the magnetic dipole-based electronic transition of a lanthanide element will be investigated. First, spherical silicon nanoparticles with diameters of the 100 nm order will be obtained since they exhibit magnetic Mie resonances at optical frequencies [21]. These magnetic Mie resonances have comparable strength and cross section to the electric Mie resonances also present in the nanoparticle and are largely spectrally separate, creating the opportunity to selectively excite specific Mie resonance modes using light with the appropriate wavelength.

The electronic transitions of the lanthanide ion, Eu^{3+}, will be chosen since Eu^{3+} supports electric and magnetic transitions with comparable cross section and strength, due to Eu^{3+} f-orbital symmetry and selection rules based on Judd-Ofelt theory [132, 135]. Furthermore, these magnetic dipole transitions occur in the visible regime, allowing for ease of detection.

In short, the coupling between an optically magnetic high index Si nanoparticle and the magnetic dipole transitions in Eu^{3+} ions will be explored via optical methods and simulation.

6.2 Simulation Methods

Potential coupling between the optically magnetic Si nanoparticle and Eu^{3+} ions present nearby can be viewed as a process where the nanoparticle modifies the environment that the Eu^{3+} ions radiate into. In essence, the ability of an Eu^{3+} ion in the excited state to relax to the ground state by emitting a photon is influenced by the photon states present in the environment, which in turn are affected by the physical composition of the environment itself [2, 136]. The effects of the environment composition, including the presence of the Si nanoparticle, on the photon states can be summarized by a parameter known as the local density of states (LDOS).

The radiative rate of an emitter is determined in large part by the local density of states of the environment. In more detail, the power (P_α) emitted by a dipole under continuous excitation is given as follows [137]:

$$P_\alpha = \hbar\omega_\alpha \Gamma_{0\alpha} F_\alpha \tag{6.1}$$

$$F_\alpha = \int_0^\infty \tilde{\rho_\alpha}(k)dk \tag{6.2}$$

where $\Gamma_{0\alpha}$ is the spontaneous emission rate in a homogeneous medium and F_α is the integral over the density of states, $\tilde{\rho}_\alpha$. Furthermore, these equations hold for both electric and magnetic dipole emitters ($\alpha = e, m$).

Equation 6.1 gives a useful empirical method for quantifying the LDOS, and thus the coupling present between a Si nanoparticle and nearby Eu^{3+} ions. By finding the power radiated by a single dipolar emitter in this system, and then comparing to the power emitted by the same emitter in vacuum, the relative local density of states may be calculated (rLDOS):

$$\text{rLDOS} = \frac{P'_\alpha}{P_\alpha} = \frac{\int_0^\infty \tilde{\rho'_\alpha}(k)dk}{\int_0^\infty \tilde{\rho_\alpha}(k)dk} \tag{6.3}$$

Based on this approach, the electromagnetic fields of a dipolar emitter in vacuum and in an environment where a Si nanoparticle is present were calculated using MiePy, an in-house software package based on generalized multiparticle Mie theory (GMMT) [33]. From those fields, Poynting's vector was calculated and integrated over a suitable reference surface. Thus, the power radiated by a dipolar emitter in vacuum and in the presence of a Si nanoparticle may be calculated, which would allow the calculation of the rLDOS and thus give a quantifiable metric of the coupling.

6.3 Experimental

To investigate the coupling mediated by the silicon nanoparticle magnetic Mie resonances, silicon nanoparticles were first embedded in gelatin films in which an Eu(III) complex was dissolved as in [136]. Then, the photoluminescence from the Eu^{3+} around the Si nanoparticle was optically investigated. This procedure was performed in the following stages:

6.3.1 Synthesis of $[Eu(Bpy)_2](NO_3)_3$

To synthesis the Eu(III) complex, europium(III) nitrate pentahydrate was purchased and dissolved as-is in ethanol. 2,2"-Bipyridyl was purchased and dissolved as-is in ethanol likewise. The two solutions were then mixed in proportions such that the Bpy and $Eu(NO_3)_3$

were at a 2:1 molar ratio. The solution was then stirred for several hours until crystals formed and then allowed to settle for several hours in a refrigerator. The supernatant was decanted off, and the $[Eu(Bpy)_2](NO_3)_3$(s) was rinsed twice with chilled ethanol.

6.3.2 Creation of Eu(III) thin films

Gelatin was added to water, heated to 60 °C, and stirred until dissolved. $[Eu(Bpy)_2](NO_3)_3$(s) was dissolved in water and then added to the gelatin solution and mixed thoroughly. At first, this Eu(III)-gelatin mixture was dropcasted onto a suitable substrate, such as a microscope coverslip, and allowed to dry. However as will be discussed in the Results section, the resulting film was over 1 μm thick as measured on a laser scanning microscope (Olympus LEXT OLS5000). Thinner films were desired in order to ensure that the dissolved Eu^{3+} ions were within near-field proximity to the embedded Si nanoparticles. As such, the Eu(III)-gelatin mixture was spin coated onto the glass coverslip. The weight percent of gelatin, spin speed, and aliquot amount were adjusted until 200-300 nm films were achieved. A summary of this empirical process is shown in Table 6.1

Run	Gelatin (w/w%)	Deposition RPM	Deposition time (s)	Drying RPM	Drying time (s)	Aliquot (mL)	Film Thickness (μm)
1	15.1	0.05	6	0.05	30	1	3.500
2	15.1	6.00	6	4.00	30	1	1.500
3	15.1	10.00	6	4.00	30	1	1.470
4	15.1	6.00	6	4.00	30	0.25	2.270
5	15.1	6.00	6	6.00	30	0.25	2.270
6	15.1	6.00	6	8.00	30	1	-
7	3.03	6.00	6	8.00	30	1	-
8	3.03	6.00	6	6.00	30	1	0.058
9	3.03	6.00	6	6.00	30	1	0.096
10	7.55	6.00	6	3.00	30	1	0.403
11	7.55	6.00	6	4.00	30	1	0.352

Table 6.1: Summary of spin coating parameters and the resulting gelatin film thickness. Note: the RPM values are the values that the dials of the spin coater instrument were set to, which due to the archaic nature of the machine, are not the actual RPM speeds.

In addition, films were also created using the precursor $Eu(NO_3)_3{\cdot}5H_2O$ as opposed to the $[Eu(Bpy)_2](NO_3)_3$(s) complex.

6.3.3 Creation of Eu(III) thin films with Si nanoparticles

First, an aqueous solution of silicon nanoparticles was sonicated and then drop-casted on a glass coverslip and left to dry in a vacuum desiccator. Then, $[Eu(Bpy)_2](NO_3)_3$(s) was dissolved in water, and then mixed with the heated Gelatin solution. This gelatin mixture was spin coated over the silicon nanoparticles so as to create a film of Eu^{3+} impregnated gelatin around the nanoparticles. A cartoon representation of a silicon nanoparticle embedded in

the Eu(III) film is shown in Figure 6.1.

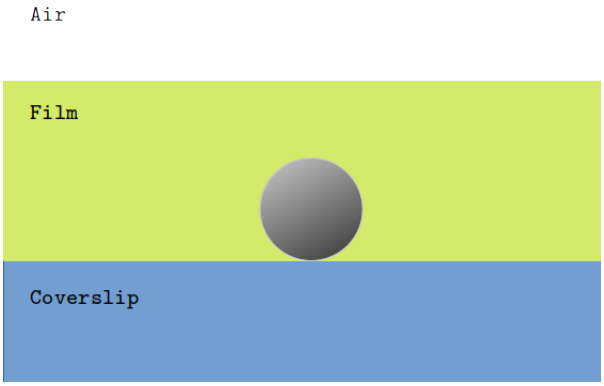

Figure 6.1: Cartoon representation of a silicon nanoparticle (nominally 100-200 nm in diameter) embedded in a gelatin film (nominally 300 nm thick), in which $[Eu(Bpy)_2](NO_3)_3$ has been dissolved.

6.3.4 Scattering Spectral Measurements

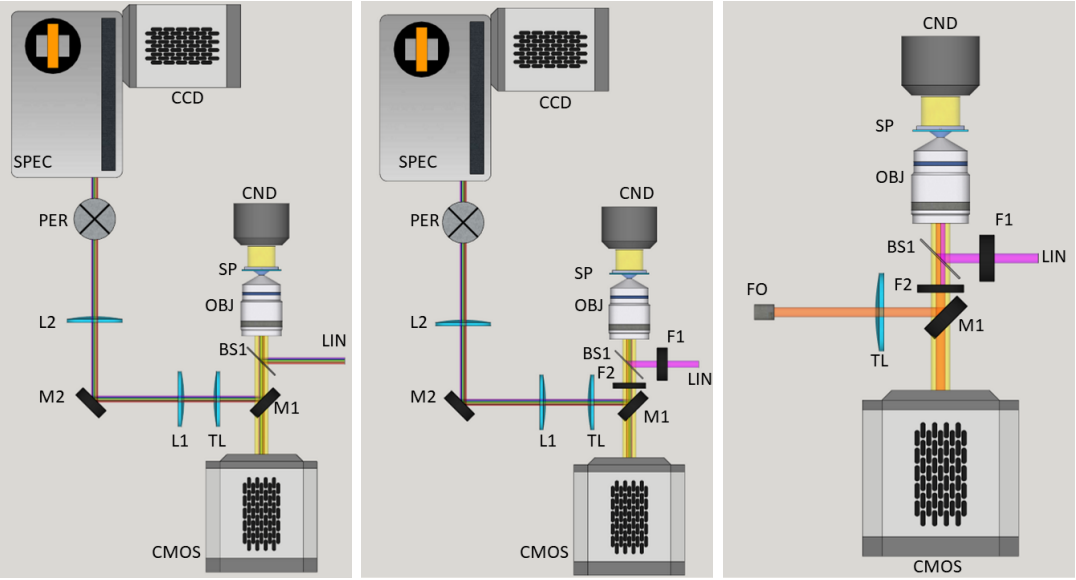

Figure 6.2: Experimental setup for optical measurements of Eu(III) complex embedded in thin films near silicon nanoparticles. Configuration for **(Left)** scattering spectral measurements, **(Center)** fluorescence spectral measurements, and **(Right)** fluorescence lifetime measurements. (LIN) Broadband or 468 nm laser light source, (F1) 468 nm bandpass filter, (BS1) 50:50 beamsplitter or 509 nm dichroic beamsplitter, (OBJ) 60x water immersion objective, (SP) sample of silicon nanoparticles embedded in thin gelatin film with Eu(III) complex, (CND) incoherent white light source, (F2) 500 nm long-pass filter and 532 nm long-pass filter, (M1) rotating mirror, (CMOS) CMOS camera, (TL) microscope tube lens, (L1 and L2) lenses for 4F system, (M2) mirror, (PER) periscope, (SPEC) spectrometer, (CCD) CCD camera, and (FO) entrance to fiber optic connected to avalanche photodiode.

Because the silicon nanoparticles and the glass substrate are non-conductive, it is not possible to use electron microscopy to image the nanoparticles in order to determine their size before they are embedded in the Eu(III) thin film. A thin conductive coating would need to be applied to the nanoparticles, which would drastically alter their optical properties. As a result, the same method described in Chapter 4 was used to determine the nanoparticle diameter by measuring the scattering spectrum.

Scattering spectra were measured using the the optical setup shown in Figure 6.2. With

the rotating mirror (M1) moved to the side, embedded silicon nanoparticles could be imaged using the incoherent white light source (CND) and then moved into the focus of the broadband laser. Then, the rotating mirror would be moved into the microscope and the white light source turned off so that the broadband laser light backscattered from the nanoparticles may be collected and measured. Each scattering spectrum was normalized by the scattering spectrum of the air-glass interface of a bare coverslip mounted in the same setup.

6.3.5 Measurements of Fluorescence Spectra and Fluorescence Lifetimes

Should the presence of the silicon nanoparticle affect the LDOS that the Eu^{3+} ions can emit into, it is expected that the fluorescence power and rate would be adjusted as explained in Section 6.2. Thus, the fluorescence spectrum of Eu^{3+} embedded in thin gelatin films near silicon nanoparticles was measured using the setup shown in Figure 6.2 with special attention paid to the intensity of the peaks corresponding to magnetic and electronic transitions. Likewise, the fluorescence lifetime of Eu^{3+} was measured using the TCSPC setup shown in Figure 6.2.

6.4 Results and Discussion

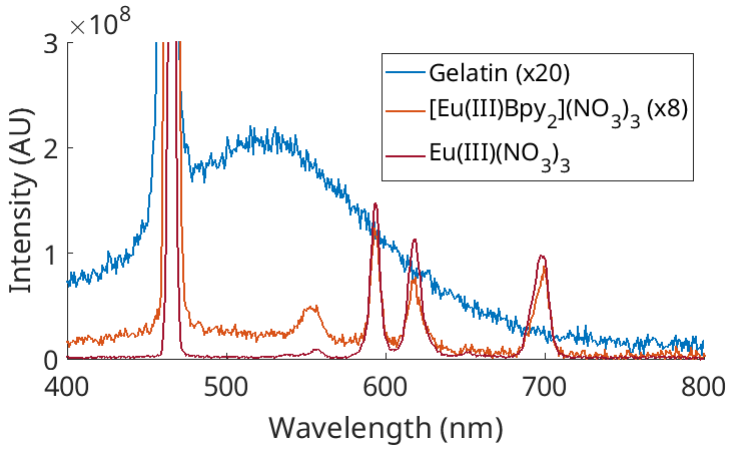

Figure 6.3: Fluorescence spectra of $[Eu(Bpy)_2](NO_3)_3$(s), $Eu(NO_3)_3{\cdot}5H_2O$(s), and Gelatin with excitation wavelength at 468 nm.

After synthesizing the $[Eu(Bpy)_2](NO_3)_3$(s), fluorescence measurements were taken under 468 nm light and compared to the original starting material, $Eu(NO_3)_3{\cdot}5H_2O$(s) as shown in Figure 6.3. Attempts were made to normalize the spectra by the different concentrations used during these measurements. Approximately five peaks can be seen at 468 nm, 555 nm, 593 nm, 618 nm, and 698 nm. The first two features at 468 nm and 555 nm are respectively due to Rayleigh and Raman scattering of the excitation beam. Using the energy levels of Eu^{3+}(aq) calculated by Carnall et al., the remaining features of fluorescence spectra can be assigned to different transitions [135]. Thus, peaks at 593 nm, 618 nm, and 698 nm correspond respectively to the $5D_0 \rightarrow 7F_1$ transition, the $5D_0 \rightarrow 7F_2$ transition, and the $5D_0 \rightarrow 7F_4$ transition. Shown in Figure 6.4 is a summary of the relevant Eu^{3+} energy levels.

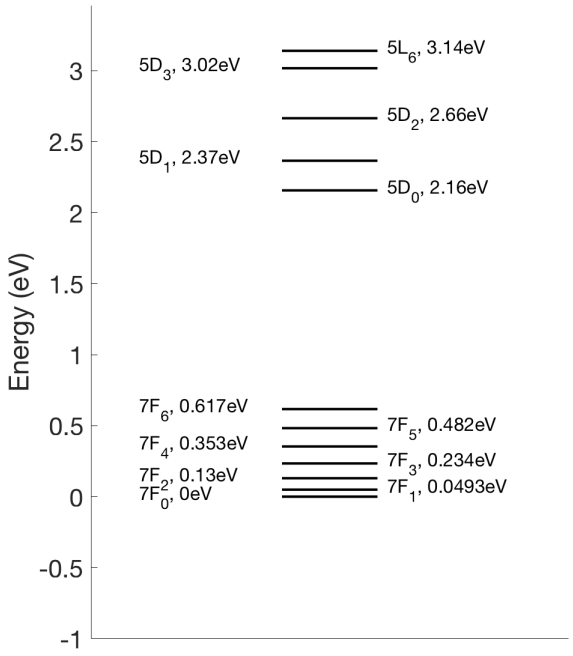

Figure 6.4: Electronic energy levels of aqueous Eu^{3+} near HOMO-LUMO gap [135]. Note that the $5D_0 \rightarrow 7F_1$ transition is magnetic dipolar in nature and the $5D_0 \rightarrow 7F_2$ is electric dipolar in nature.

As can be seen from Figure 6.3, the fluorescence intensity of the starting material $Eu(NO_3)_3{\cdot}5H_2O(s)$ is comparable to the fluorescence intensity of $Eu(NO_3)_3{\cdot}Bpy_2(s)$, after accounting for the differences in concentration. The purpose of complexing Eu^{3+} with 2,2'-Bipyridine was to enable the Bpy moiety, which is highly absorptive of low wavelength photons, to absorb the excitation light, after which the photon energy would transfer to the Eu^{3+} ion with high efficiency [136]. However, as can be seen from the two fluorescence spectra in Figure 6.3, the two Eu(III) complexes are equally responsive to 468 nm light, and as a result both were used to to make Eu(III) thin films for the the proceeding experiments.

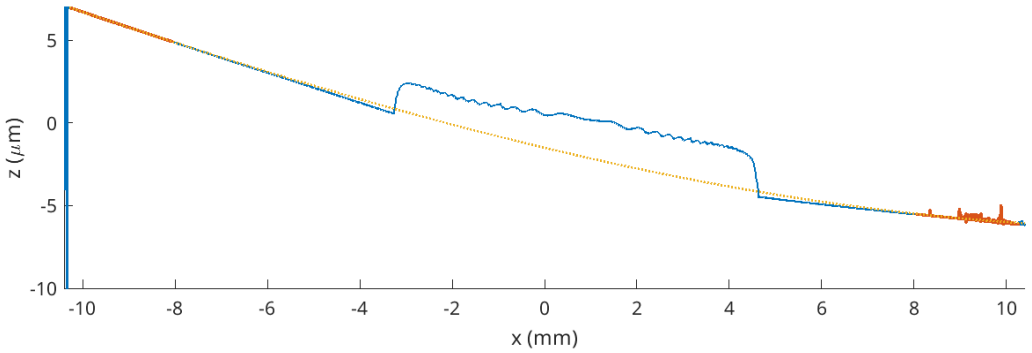

Figure 6.5: Side profile of $Eu(NO_3)_3{\cdot}Bpy_2(s)$ and gelatin mixture after being dropcasted on a glass coverslip and allowed to dry. **(Blue)** Profile of gelatin drop after drying. **(Orange)** Profile of glass coverslip.

At first, the mixture of gelatin with $Eu(NO_3)_3{\cdot}Bpy_2(s)$ was dropcasted on a glass coverslip and allowed to dry. However as can be seen in a representative sample in Figure 6.5, the resulting film was quite thick, with a height of approximately 2 μm. Note that the overall curvature of the profile is due to a slight curve in the glass coverslip from the manufacturing process. A film with a thickness close to the diameter of the nanoparticles, similar to Figure 6.1, was desired in order to ensure that Eu^{3+} ions were near the silicon nanoparticles, at least in the vertical direction.

After switching to spin coating, gelatin films with thicknesses of a few hundred nanometers were obtained (see Table 6.1). The primary factors which led to films with the correct thickness were using a more dilute solution of Gelatin (7.55 w/w%) and increasing the drying spin speed. With these conditions, films with a thickness around 352 nm were produced.

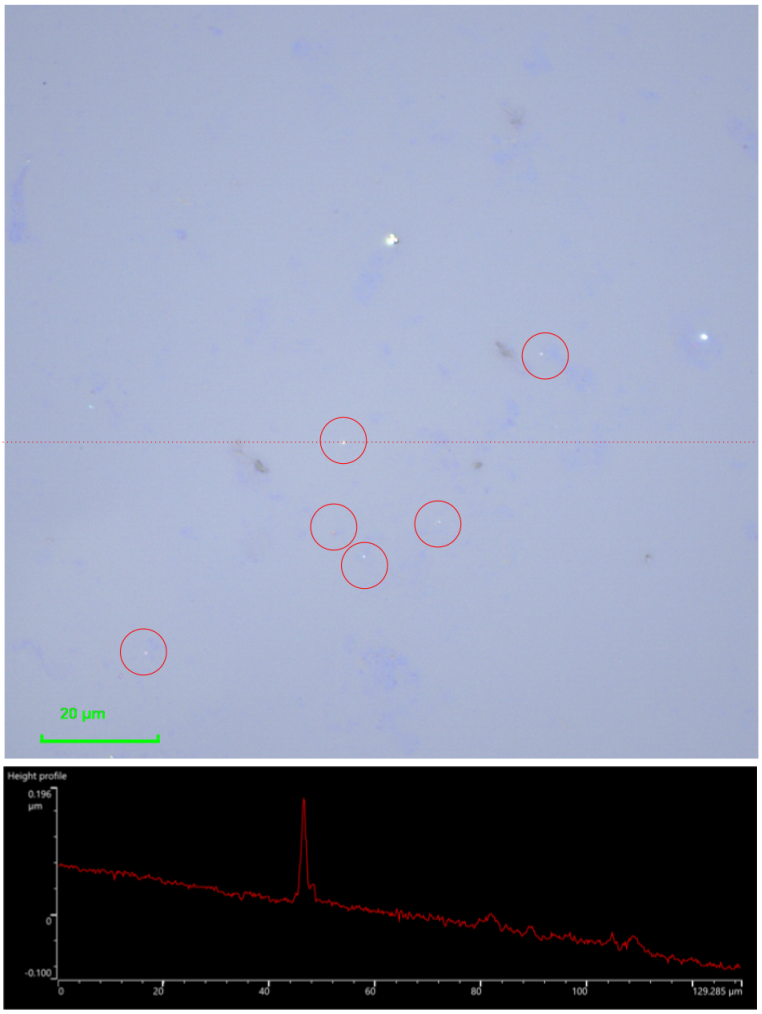

Figure 6.6: **(Top)** Top-down brightfield microscope image of gelatin film with Eu(III) complex and silicon nanoparticles. Red circles are drawn around select silicon nanoparticles. Red dashed line shows region where profile was measured. **(Bottom)** Height profile measurement of the same sample. Note the lack of significant features at x = 60 μm where a silicon nanoparticle is located, indicating that the nanoparticle is not causing the film to bulge. The large peak at x = 43 μm is due to a debris particle.

A brightfield microscope image and profile measurement of one such sample is shown in Figure 6.6. Due the silicon nanoparticles' strong Mie resonances, the nanoparticles show up brightly colored, in contrast to the background. From the images, no evidence of any streaks or air pockets forming within the film around the nanoparticles can be seen, indicating that the nanoparticles are completely embedded within the gelatin film. In addition, the

profile measurements indicate that no humps were forming on the surface of the film above the nanoparticles, indicating that the presence of the nanoparticles would not disturb the surface quality of the film. Furthermore, any Eu^{3+} ions in the region of the film above a given nanoparticle would be within near-field proximity of the nanoparticle due the fact that the thickness of the film is approximately one wavelength.

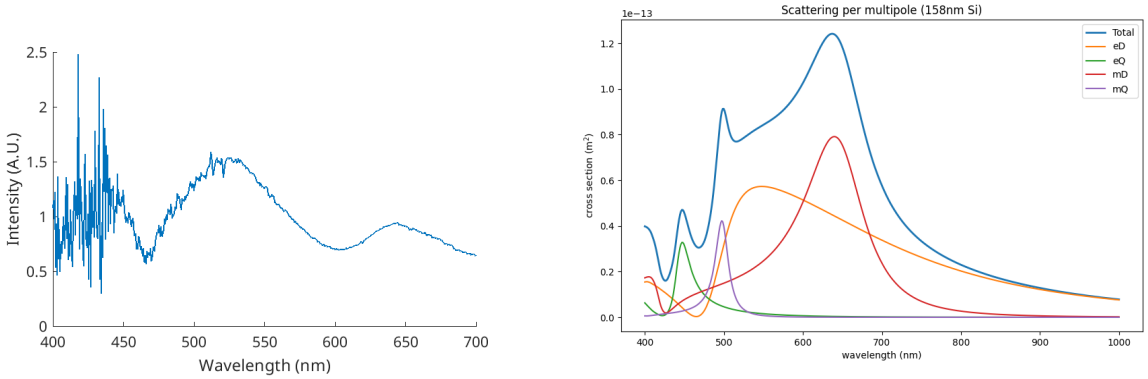

Figure 6.7: **(Left)** Normalized scattering spectrum of a silicon nanoparticle embedded in the gelatin film. **(Right)** Calculated scattering cross section of a 158 nm silicon nanoparticle in gelatin medium. Both the total cross section and the cross section per multipole mode are shown.

Silicon nanoparticles were identified using the brightfield images, and then the scattering spectra of these particles were taken to obtain their size. By comparing the scattering peaks to the spectra calculated using GMMT, the nanoparticle diameter may be found. Shown in Figure 6.7 is a representative scattering spectrum of a silicon nanoparticle inside the gelatin film. In order to account for the power spectrum of the broadband laser light source, the raw scattering spectrum of the nanoparticle was normalized by the scattering off the air-glass interface of a coverslip. Also shown in Figure 6.7 is the total scattering cross section and scattering cross section per multipole calculated using GMMT for a 158 nm silicon nanoparticle in a gelatin medium. The most prominent features are the magnetic dipole peak at 640 nm and the electric dipole peak at 544 nm. By comparing the peaks of the experimental spectrum to the simulated one, it is inferred that the embedded silicon nanoparticle is

likewise 158 nm in diameter. Note that in the experimental scattering measurement, only the backscattered light is collected over the limited numerical aperture of the microscope objective (see Figure 6.2). As a result, while the peak positions measured would be at the same location as ones in the corresponding GMMT calculations, the shapes would be different. Nonetheless, measuring the scattering spectrum and comparing to the one calculated via GMMT is an effective method for determining the particle shape.

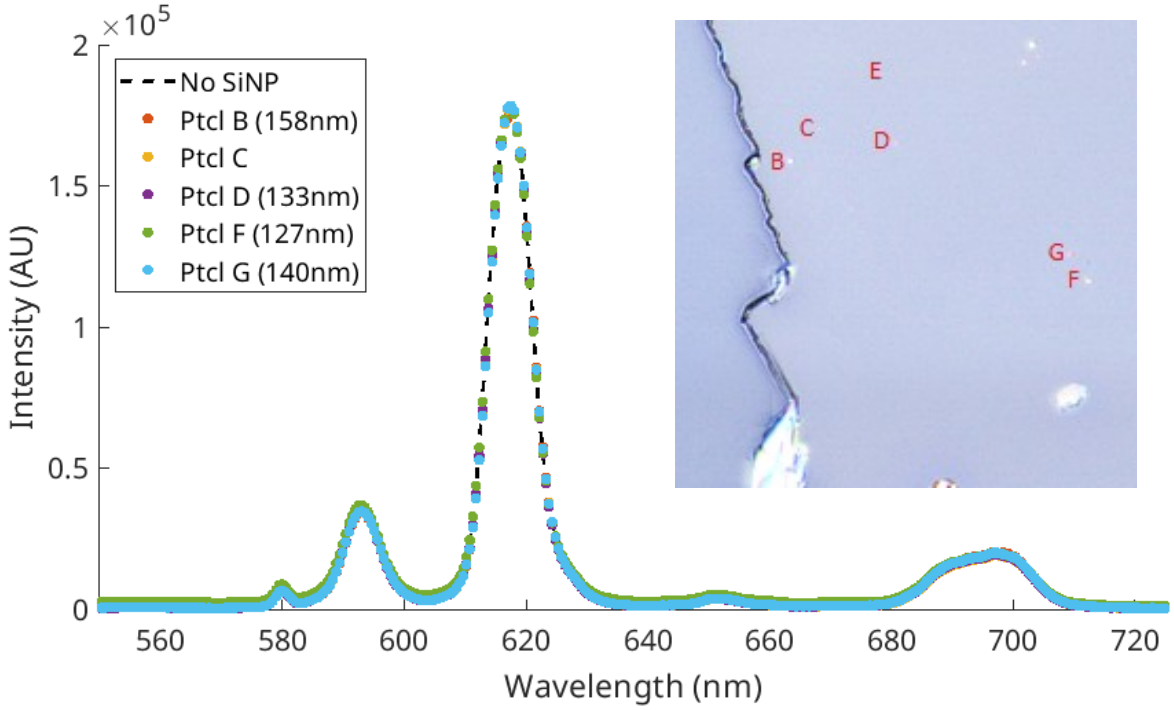

Figure 6.8: Fluorescence spectra of Eu(III) complex embedded in gelatin film near select silicon nanoparticles. Each spectrum has been normalized so that all maxima are at the same intensity. Black dotted line is the spectrum of a region of film without any nanoparticle present. **(Inset)** Brightfield microscope image of the corresponding gelatin film embedded with Eu(III) complex and silicon nanoparticles. Jagged edge in image is a scratch made in the film as a place marker.

The fluorescence of Eu(III) complex embedded in the gelatin film was measured near a number of silicon nanoparticles with varying sizes. Figure 6.8 shows representative fluorescence spectra of Eu(III) complex near several silicon nanoparticles. Each spectrum was normalized so that the maximum of each was at the same intensity. Note that for Particle

C (Ptcl C), the size could not be resolved from the experimental scattering spectrum. From a initial examination, the spectra are all very similar in peak position, shape, and intensity after the normalization.

The features of the fluorescence spectra can be assigned to different electronic transitions within Eu^{3+} (see Figure 6.4). First at 580 nm, appears the $^5D_0 \rightarrow {}^5F_0$ transition. The small peak intensity is due to the fact that this transition is forbidden and occurs due to environment induced relaxation of the selection rules [138, 139]. At 593 nm and 618 nm are the $^5D_0 \rightarrow {}^5F_1$ and $^5D_0 \rightarrow {}^5F_2$ transitions, respectively. The former occurs primarily by a magnetic dipole transition, whereas the latter occurs primarily by an electric dipole one. At 651 nm is the $^5D_0 \rightarrow {}^5F_3$ transition. Just like with the $^5D_0 \rightarrow {}^5F_0$ transition, the $^5D_0 \rightarrow {}^5F_3$ transition is forbidden and has a very weak intensity [140]. Finally at 694 nm is the $^5D_0 \rightarrow {}^5F_4$ transition. These peak assignments are summarized in Table 6.2.

Transition	Calculated ΔE (eV)	Observed Spectral Position
$^5D_0 \rightarrow {}^5F_0$	2.16	580 nm
$^5D_0 \rightarrow {}^5F_1$	2.11	593 nm
$^5D_0 \rightarrow {}^5F_2$	2.03	618 nm
$^5D_0 \rightarrow {}^5F_3$	1.93	651 nm
$^5D_0 \rightarrow {}^5F_4$	1.81	694 nm

Table 6.2: Summary of electronic transitions observed in Eu^{3+} fluorescence spectra.

With regards towards coupling between the electric and magnetic dipole-based electronic transitions of Eu^{3+} ions and the magnetic Mie modes of silicon nanoparticles, special attention was paid to the peak intensities of the $^5D_0 \rightarrow {}^5F_1$ and $^5D_0 \rightarrow {}^5F_2$ transitions. When occurring in the presence of a silver mirror, the peak intensities were significantly modified, and the intensity of the electric dipole transition was reduced with respect to the magnetic dipole transition [136]. In a like manner, it was expected that the presence of a silicon

nanoparticle would induce a difference between the relative peak intensities of the magnetic and electric dipole transitions. It was expected that the electric and magnetic dipole transitions of the Eu^{3+} ions in the near-field vicinity of the nanoparticle would couple, respectively, to the nanoparticle Mie electric and magnetic dipole resonances, which vary in strength with the nanoparticle size. However as can be seen in Figure 6.8, the $^5D_0 \rightarrow {}^5F_2$ transition peak and the $^5D_0 \rightarrow {}^5F_1$ transition peak have the same relative intensities regardless whether a nanoparticle is present (Colored dots) or not (Black dashed line). Furthermore, the fluorescence of Eu^{3+} ions near silicon nanoparticles of different sizes (127 nm - 158 nm) was measured. While the intensity and spectral position of the Mie resonances change significantly with nanoparticle diameter [21], the $^5D_0 \rightarrow {}^5F_1$ and $^5D_0 \rightarrow {}^5F_2$ transition peaks do not show any difference in relative intensity over this nanoparticle size range.

To further investigate possible coupling between the electric and magnetic dipole-based electronic transitions of Eu^{3+} and the Mie resonances of silicon nanoparticles, fluorescence lifetime measurements were taken after directly exciting the $^5D_0 \rightarrow {}^5F_1$ and $^5D_0 \rightarrow {}^5F_2$ transitions with 590 nm and 614 nm light, respectively. In this situation, the effect of the silicon nanoparticle would be twofold. First, the Mie dipole modes of the nanoparticle would concentrate the laser pulse in the near-field regime in a selective fashion. For example, the magnetic dipole mode of the silicon nanoparticle calculated in Figure 6.7 would selectively concentrate light at approximately 638 nm, whereas the electric dipole mode would selectively concentrate light at 554 nm. Thus for an appropriately sized nanoparticle, the probability of nearby Eu^{3+} absorbing a photon via the $^5D_0 \rightarrow {}^5F_1$ or $^5D_0 \rightarrow {}^5F_2$ transition is increased. Secondly, the presence of the nanoparticle is expected to modify the rLDOS, as mentioned in Section 6.2. It is expected that both these effects would manifest themselves in a change to the fluorescence lifetime of the Eu^{3+} ions.

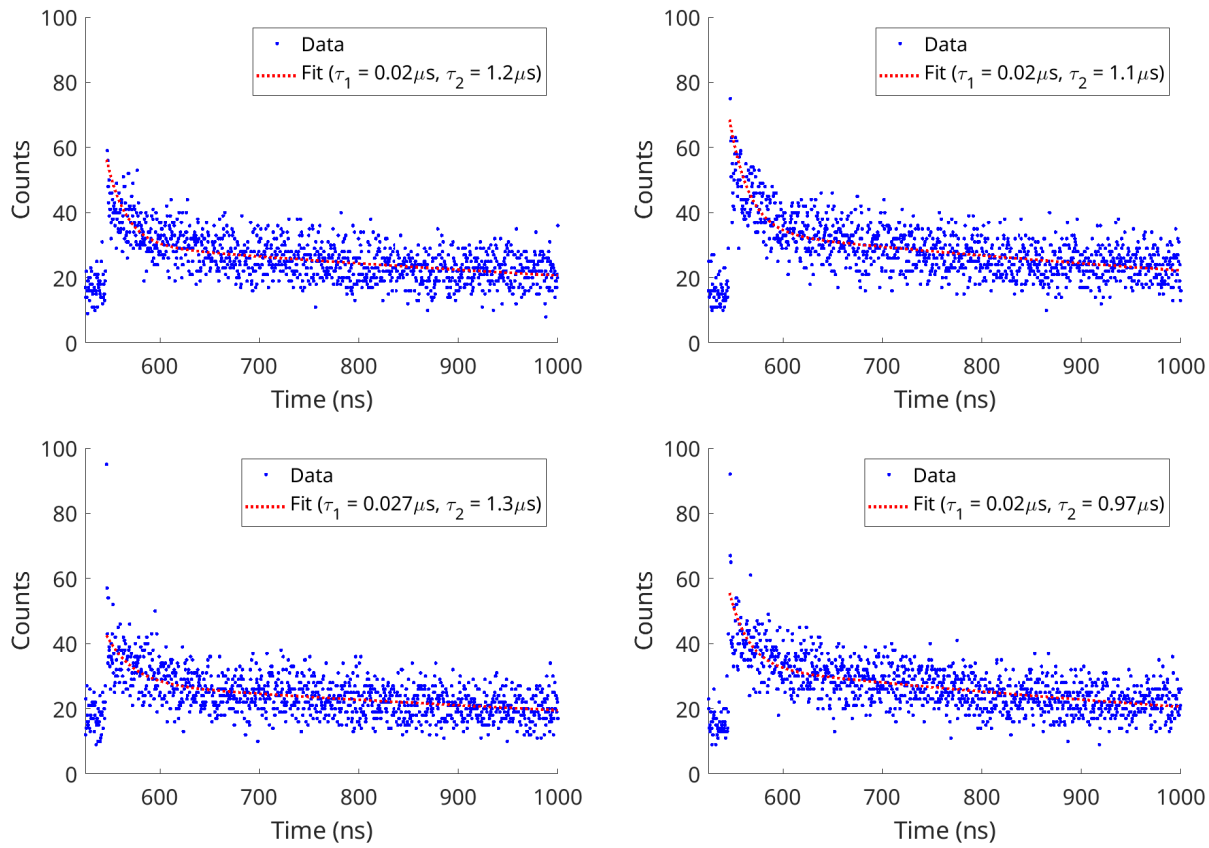

Figure 6.9: Fluorescence lifetimes and corresponding biexponential fits of Eu(III) complex embedded in gelatin film near Particle G (See Figure 6.8) after exciting with **(Top Left)** 590 nm and **(Top Right)** 614 nm light, as well as fluorescence lifetimes and biexponential fits of Eu(III) complex in a silicon nanoparticle-free region of the gelatin film after excitation with **(Bottom Left)** 590 nm and **(Bottom Right)** 614 nm light. Excitation laser is incident at 503.6 ns.

Shown in Figure 6.9 are representative fluorescence lifetime measurements of the same sample of silicon nanoparticles and Eu(III) complex embedded in gelatin film described in Figure 6.8. The lifetimes of Eu^{3+} ions embedded near a silicon nanoparticle are shown for excitation with both 590 nm and 614 nm pulsed light. For comparison, lifetime measurements were also taken of Eu^{3+} in a region of the gelatin film without a nanoparticle.

Comparing the lifetimes of Eu^{3+} both with and without the presence of a silicon nanoparticle, a difference cannot be clearly seen. Biexponential functions were fitted to the lifetimes

of Eu^{3+} near the nanoparticle, and the resulting time constants were $\tau_1 = 0.020\mu$s and $\tau_2 = 1.2\mu$s for 590 nm excitation light and $\tau_1 = 0.020\mu$s and $\tau_2 = 1.1\mu$s for 614 nm excitation light. In contrast, the biexponential fits to the lifetimes of Eu^{3+} without the nanoparticle yield time constants of $\tau_1 = 0.027\mu$s and $\tau_2 = 1.3\mu$s for 590 nm excitation light and $\tau_1 = 0.020\mu$s and $\tau_2 = 0.97\mu$s for 614 nm excitation light.

To explain the results from all these optical measurements, the relative density of states around a silicon nanoparticle can be simulated as described in Section 6.2. First, GMMT was used to calculate the power radiated by a point dipole in free space and in the environment near a given silicon nanoparticle. Then the two powers were divided as described in Equation 6.3 in order to obtain the rLDOS difference between the two situations.

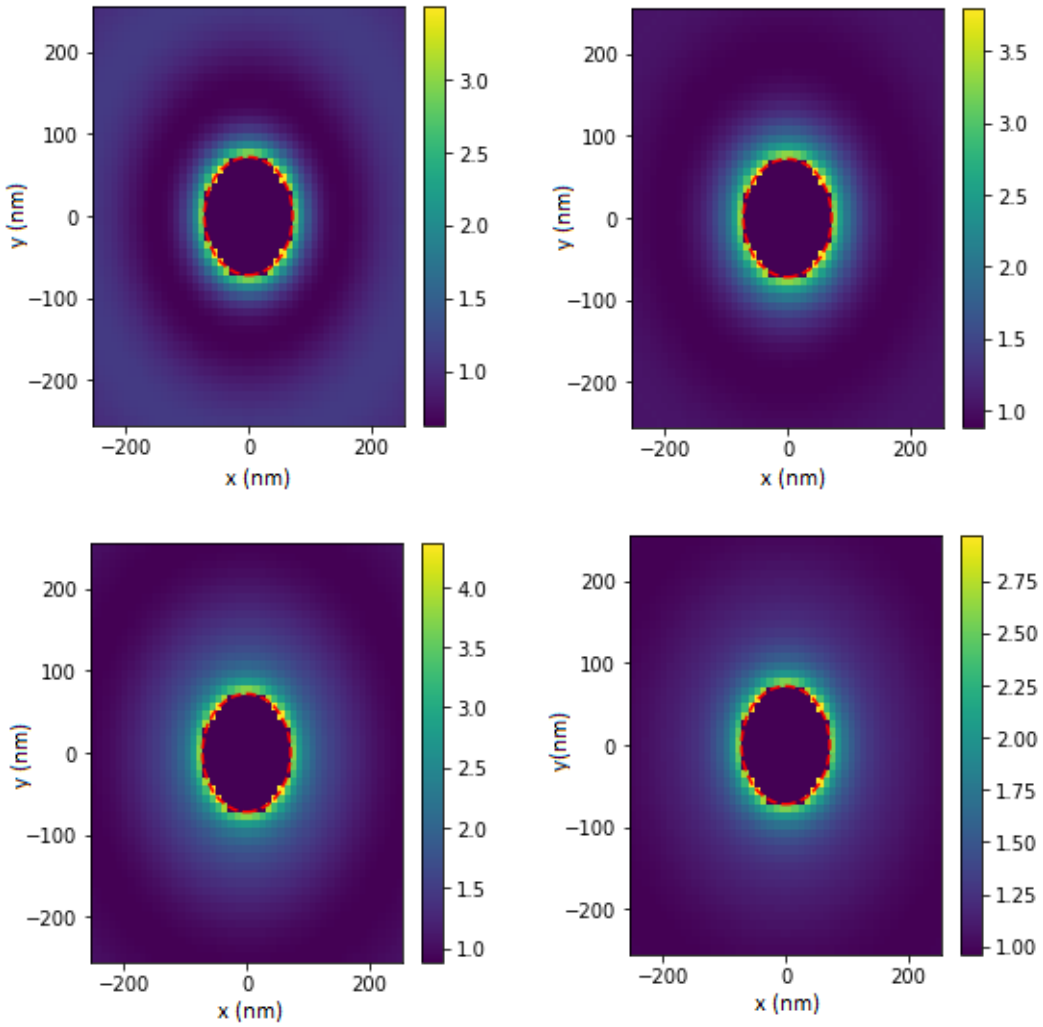

Figure 6.10: Simulated relative local density of states in the spatial region around a 144 nm silicon nanoparticle for an electric dipole at **(Top Left)** 590 nm and **(Top Right)** 615 nm, as well as a magnetic dipole at **(Bottom Left)** 590 nm and **(Bottom Right)** 615 nm. Red dashed line indicates boundary of the nanoparticle and colorbar gives the rLDOS scale.

Illustrated in Figure 6.10 are the results of rLDOS simulations for an electric and magnetic dipole at 590 nm and 615 nm, the wavelengths at which the europium $^5D_0 \rightarrow {}^5F_1$ and $^5D_0 \rightarrow {}^5F_2$ transitions occur, respectively. As can be seen, the maximum magnetic dipole rLDOS is higher at 590 nm than at 615 nm. Furthermore at 590 nm, the maximum magnetic dipole rLDOS is higher than the maximum electric dipole rLDOS. This trend can be explained by

the fact that the 144 nm silicon nanoparticle has a Mie magnetic dipole resonance at 590 nm, as calculated by GMMT (See Figure 6.11).

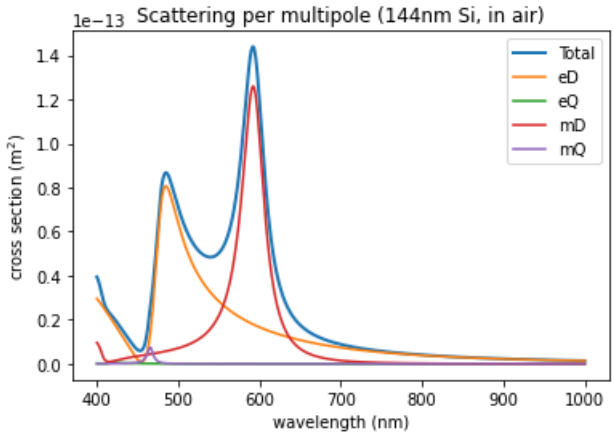

Figure 6.11: Total scattering cross section and scattering cross section per Mie multipole of a 144 nm silicon nanoparticle.

However as illustrated by Figure 6.10, the maximum rLDOS enhancement calculated in these simulations is approximately 4x compared to free space. Furthermore, the spatial region where a rLDOS enhancement greater than 1x occurs seems to be limited to the region within approximately 70 nm of the nanoparticle surface.

The rLDOS enhancement can also be averaged over a given volume enclosing the nanoparticle in order to consider the effect that all Eu^{3+} radiating within that volume has on the total fluorescence of the Eu(III) complex and Si nanoparticle system. This approach is different from the simulation shown in Figure 6.10, where the rLDOS at particular spatial points are calculated.

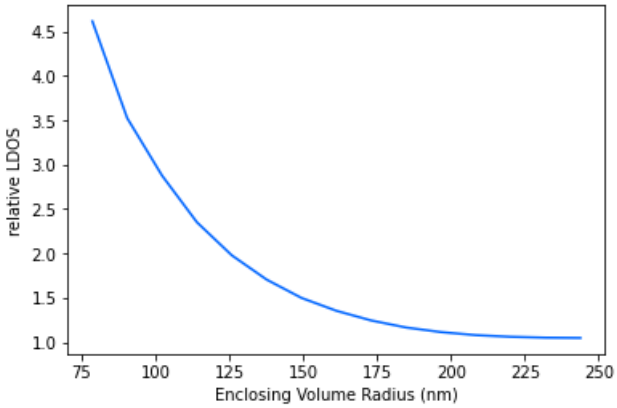

Figure 6.12: Relative local density of states averaged over a spherical volume enclosing a 144 nm silicon nanoparticle. Note that at a volume radius of 72 nm, the spherical volume is just as large as the nanoparticle itself.

Shown in Figure 6.12 is the result of averaging the simulated rLDOS within a given spherical enclosing volume. As is expected, the average rLDOS is largest when the enclosing volume is encompassing the spatial region close to the nanoparticle. In this situation, just the Eu^{3+} ions near the nanoparticle, which would be the europium ions most affected by the nanoparticle presence, are being measured. As the enclosing volume radius gets larger and larger, more Eu^{3+} further away from and less affected by the nanoparticle is encompassed and thus the average rLDOS decreases. It is interesting to note how fast the average rLDOS decreases. Once the spherical volume boundary is approximately 75 nm away from the nanoparticle surface (Enclosing Volume Radius = 150 nm in Figure 6.12), the average rLDOS has decreased to 1.5x.

With this in mind, the lack of any apparent effects of the silicon nanoparticles on the fluorescent behavior of the Eu^{3+} could be attributed to the fact that only the Eu^{3+} very close to the nanoparticle surface was undergoing any sort of coupling, and the modified fluorescence of these Eu^{3+} ions were being overshadowed by the behavior of the Eu^{3+} ions in the bulk of the gelatin film. As indicated by Figure 6.12, the Eu^{3+} under observation has to be within a few tens of nanometers of the silicon nanoparticle. While this condition

may be met for the Eu^{3+} vertically above and below the nanoparticle due to how the gelatin film was constructed (see Figure 6.1), the Eu^{3+} laterally to the side of the nanoparticle will behave as in free space if they are in regions further than a few tens of nanometers away.

A second reason to explain the lack of any apparent effects would the the magnitude of the simulated rLDOS enhancement. As shown in Figure 6.10, the maximum enhancement for either magnetic dipole and electric dipole is approximately 4x even at the surface of the nanoparticle. In comparison, investigations of similar systems of fluorescent emitters and plasmonic structures have seen fluorescent enhancements at least an order of magnitude larger, or even spectral peak splitting due to strong coupling [6, 141, 142, 143, 144, 145, 146, 147]. For example, heterodimers constructed from 80 nm and 50 nm Au nanoparticles with gaps of 4.2 and 5.0 nm between the nanoparticles by Jiajing Li and others can be considered [6]. Experiments and simulations of the heterodimers indicate a surface-enhanced Raman scattering (SERS) enhancement factor (EF) on the order of 10^5–10^6. Furthermore in another work, Waks and others quantum mechanically analyzed the interaction between a metal nanoparticle and dipole-like emitter [141]. When the separation between the nanoparticle and emitter was smaller than 5 nm, a Purcell enhancement on the order of 10^2 was observed. In addition, Okamoto and others deposited CdSe quantum dots on a thin gold film in order to use surface-plasmon coupling to enhance the photoluminescent behavior of the quantum dots [142]. An enhancement by a factor of 23 in the photoluminescence was observed. Finally, Chen and others analyze the light-mediated interactions between an arbitrary cluster of metal nanoparticles and a two-level quantum emitter [143]. These authors observed a Purcell enhancement on the order of $10^1 - 10^2$ when the emitter was placed between a dimer of two gold prolate spheroids. A summary of these results is shown in Table 6.3.

System	Calculated or Observed Enhancement
Heterodimers with Sub-5 nm Nanogaps[6]	On the order of $10^5 - 10^6$ (SERS enhancement)
Metal nanoparticle and dipole emitter[141]	On the order of 10^2 (when separation is very small)
Quantum Dots on Au film[142]	23x enhancement of photoluminescence intensities
Two level emitter between two gold prolate spheroids[143]	On the order of $10^1 - 10^2$

Table 6.3: Summary of nanophotonic systems comparable to the Eu^{3+} and silicon nanoparticle system and their corresponding enhancement factors.

6.5 Conclusion

In summary, the coupling between the electronic transitions of the Lanthanide ion, Eu^{3+}, and the Mie electric and magnetic dipole modes of a silicon nanoparticle was explored. A thin layer of gelatin was created with both Eu^{3+} ions and silicon nanoparticles embedded inside. The quality of the film and and the Eu(III) complex was checked using laser profilometry and fluorescence spectroscopy. Then, TCSPC and fluorescence spectroscopy were used to optically study the Eu^{3+} and silicon nanoparticle system. When compared to a control sample consisting of just Eu^{3+} embedded in the gelatin film, very little difference was observed in the fluorescence lifetime and spectral measurements. Further analysis using simulations of the Eu^{3+} and silicon nanoparticle system, as well as calculations of the rLDOS, were performed, and a maximum rLDOS enhancement of 4x compared to the control was found. Thus, the potential coupling would be small compared to similar photonic systems. Furthermore, the simulations indicated that the fluorescent behavior of any Eu^{3+} coupling to the nanoparticle would be overshadowed by the photoluminescence of the Eu^{3+} in the

bulk of the film.

Future directions would be focused around first isolating the photoluminescence of Eu^{3+} that is near the silicon nanoparticle in order to see the effect of any possible coupling. For example, the use of a gelatin film can be avoided by sputter coating Eu_2O_3 onto the silicon nanoparticles. This method would ensure that the Eu^{3+} ions are in very close proximity to the nanoparticles. Furthermore with this approach, the lack of a gelatin film with embedded Eu^{3+} ions would prevent bulk Eu^{3+} from overshadowing the photoluminescence of Eu^{3+} near the nanoparticle.

The next major future direction is increasing the strength of the coupling between the silicon nanoparticles and nearby Eu^{3+}. One method would be to use regular arrays of silicon nanoparticles, similar to the work by Castellanos and others [8]. Such an array of silicon nanoparticles would exhibit a strong grating mode, which is more likely to couple to the electronic states of Eu^{3+}. Another method would be to use closely spaced silicon nanoparticle dimers, similar to the work by Li and others [6]. It is anticipated that a strong electromagnetic field enhancement would occur in the dimer gap, allowing for better coupling to any Eu^{3+} ions present.

APPENDIX A

ELECTRODYNAMIC INTERFERENCE AND COUPLING IN NANOPARTICLE-BASED OPTICAL MATTER ARRAYS

Reproduced in part with permission from: Curtis Peterson, John Parker, Emmanuel Valenton, Yuval Yifat, Stuart A. Rice, and Norbert F. Scherer. Electrodynamic Interference and Coupling in Nanoparticle-based Optical Matter Arrays. Manuscript in preparation.

The understanding of light-matter interactions in nanophotonics and optical matter has for the most part focused mainly on the electric field and the electric properties of matter. One example of this perspective is our recent work studying the interaction between the nanoparticles of an optical matter array.

Introduction. In general, multiple particles simultaneously present in optical traps interact electrodynamically with one-another, and these interactions produce optical binding forces. As a result the particles tend to self-organize into ordered optical matter (OM) arrays with preferred inter-particle separations at (near) integer multiples of the incident laser wavelength[61, 20, 148, 149, 150]. The optical binding forces arise from the interaction between the polarization induced in each particle by the light incident and scattered from other particles[151, 149]. OM arrays are open, nonequilibrium systems because the coherent light source that mediates the optical binding forces also causes a constant flux of electromagnetic energy through the system[19]. Conversion or redirection of the momentum from the incident laser light makes possible phenomena such as non-reciprocal forces[19, 14, 15], negative optical torque[152, 16, 70, 17, 9], and nanoscale light sails.[153] Therefore, a full description of an OM array requires knowing the detailed properties of both the incident and scattered electromagnetic fields in addition to the positions, sizes, shapes, and composition of each particle.

While there has been steady progress toward understanding how tailoring the phase and

intensity profiles of the incident fields can affect the dynamics and structures formed by optically trapped plasmonic nanoparticles[154, 75, 155, 156, 77, 157, 158, 159], the characteristics of coherent light scattered by OM arrays is an area of current research[160, 161, 9, 162]. The periodic wavelength-scale structures of OM arrays[163] suggest that electromagnetic interference plays an important role in the properties of the light they scatter. In addition, the large scattering cross sections of the plasmonic nanoparticles that OM arrays are often comprised of[164, 150] suggest that electrodynamic coupling may also be important, leading to potentially new forces and behavior extrinsic to the properties of the light source[165, 166]. However, the respective roles of electromagnetic interference and electrodynamic coupling with respect to the coherent light scattered by OM arrays and their interdependency has received little attention.

By electrodynamic coupling, we mean the polarization induced in one particle due to light scattered by another particle, and which can be categorized into two regimes[167, 168, 169]. In near-field coupling the interaction between particles with separations much smaller than the wavelength of light is treated as a quasi-static[170, 171]. In far-field coupling objects interact with one-another through scattered radiation. In large arrays far-field coupling dramatically affects each particle's polarization; the interaction between particles is frequently treated analogously to methods in solid-state physics, *i.e.* with an approach that invokes the periodicity of the array[172, 173, 174, 175]. Both types of coupling modify the induced polarization of a particle in the array due to light scattered by other nearby particles. Near-field coupling is significantly stronger than far-field coupling and is often studied on a pairwise basis[170, 171]. Far-field coupling is usually studied in the limit of very large arrays, although some research has examined finite-size effects[176]. The approaches typically used in the near- and far-field coupling regimes are not suitable for describing coupling in small OM arrays: a quasi-static approach is inappropriate because retardation is significant over the wavelength-scale distances characteristic of OM arrays, and the edges and boundaries

of finite size arrays precludes momentum space representations. However, it is important to note that coupling (and the associated induced polarizations give rise to the many-body nature of OM arrays.

In this paper we show that optical matter arrays exist in a regime where interference determines the spatial profile of the light scattered by the array, but coupling (and multiple scattering) enhances the polarization induced in the array's constituent material elements (*e.g.* metal or dielectric nanoparticles). We show that the images obtained with coherent backscattered light (termed coherent imaging) from OM arrays contrast strongly with those obtained with incoherent light. While diffraction and fringe patterns visible in the coherent images characterize the electric field intensity surrounding the OM arrays, the more striking finding is the replacement of particle-centric images obtained with incoherent light illumination with images where the intensity is shifted between particles when visualized with coherent light. We investigate the directional scattering of coherent light over polar angles by performing generalized multiparticle Mie theory (GMMT) calculations of ordered OM arrays with 1-7 particles. In contrast to the largely dipolar scattering of a single particle[177, 2], the light scattered from ordered OM arrays develops a lobed structure with maxima in specific sideways, forward, and backward directions. This scattering can also be described in terms of collective modes that arise from multi-particle coupling[176, 9].

We find that the total scattering of small OM arrays at the trapping laser wavelength grows super-extensively (*i.e.* faster than linear) when nanoparticles are added to the array. The super-extensive growth of the scattering is the result of electrodynamic coupling. We quantify the strength of electrodynamic coupling in OM arrays at the trapping laser wavelength by calculating the ratio of the total electric field intensity to the incident intensity at a vacant site in the array, finding that the contribution from neighboring particles becomes significant even for small (1-6 neighboring particles) OM arrays. The measured scattering and local density of states (LDOS) enhancement for a range of wavelengths shows that both

increase near the trapping laser wavelength as more particles are added to the OM array, and a collective resonance develops at the expense of the single-particle Mie resonance scattering from individual particles[176]. We also show simulated and experimental backscattered spectra that demonstrate the scattering enhancement of a coherent light source by OM arrays. Finally, we extend our investigation to larger hexagonal arrays to show the connection between OM arrays of plasmonic nanoparticles and surface lattice resonances (SLR's; also known as lattice plasmons)[178, 179, 168, 172, 173, 174]. Specifically, the sharp resonances that yield scattering enhancement in large regular arrays of nanoparticles occurs concurrently with enhancement of the induced polarization similar to that seen in small OM arrays.

We interpret our results in the context of analytical theory in the point-dipole approximation and show that electrodynamic coupling in OM arrays is strengthened by constructive interference. Specifically, the large scattering cross sections of the plasmonic particles often used in OM experiments, the emergent periodic structures that self-organize, and the wavelength-scale separations between the particles all play important roles. Our work demonstrates that collective excitations in OM arrays are equivalent to SLR's in the small lattice-size regime.[176]

Experimental setup. Our experiments were conducted with a single-beam optical tweezers in an inverted microscope as described previously[76]. A schematic of the experimental set-up is shown in Figure A.1. A dilute aqueous solution of PVP-coated 150 nm Ag nanoparticles was placed inside a sample chamber made from an adhesive spacer sandwiched between two glass cover-slips. A cw Ti-sapphire laser was nearly collimated at the back aperture of a 60x microscope objective (Nikon SAPO 60x water; $NA = 1.27$), creating a converging beam that pushed and trapped a small number of particles close to the top glass surface of the sample chamber. The focus of the optical trapping beam was adjusted with a spatial light modulator (SLM; Meadowlark) to create an inward directed phase gradient at the trapping

plane that increased the confinement of the nanoparticles[155, 9]. Electrostatic repulsion between the ligands on the nanoparticles and the charged glass cover-slip balance the radiation pressure, resulting in nanoparticle trapping in a 2D plane. The trapping laser was circularly polarized in all experiments and calculations.

To image the coherent back-scattered light, we employed a 2-channel configuration where one channel accepted 470 nm incoherent LED darkfield illumination, and the other channel filtered out the LED light and accepted the backscattered laser light but with significant attenuation ($OD = 5$). The two channels form spatially separated images on the same CMOS detector (Andor Neo). The simultaneous measurements are necessary because the particle positions are not obvious from the images of backscattered coherent light as can be seen in Figure A.1b-g. No additional field stops or aperture stops were introduced to the optical path so the nominal numerical aperture is that of the objective.

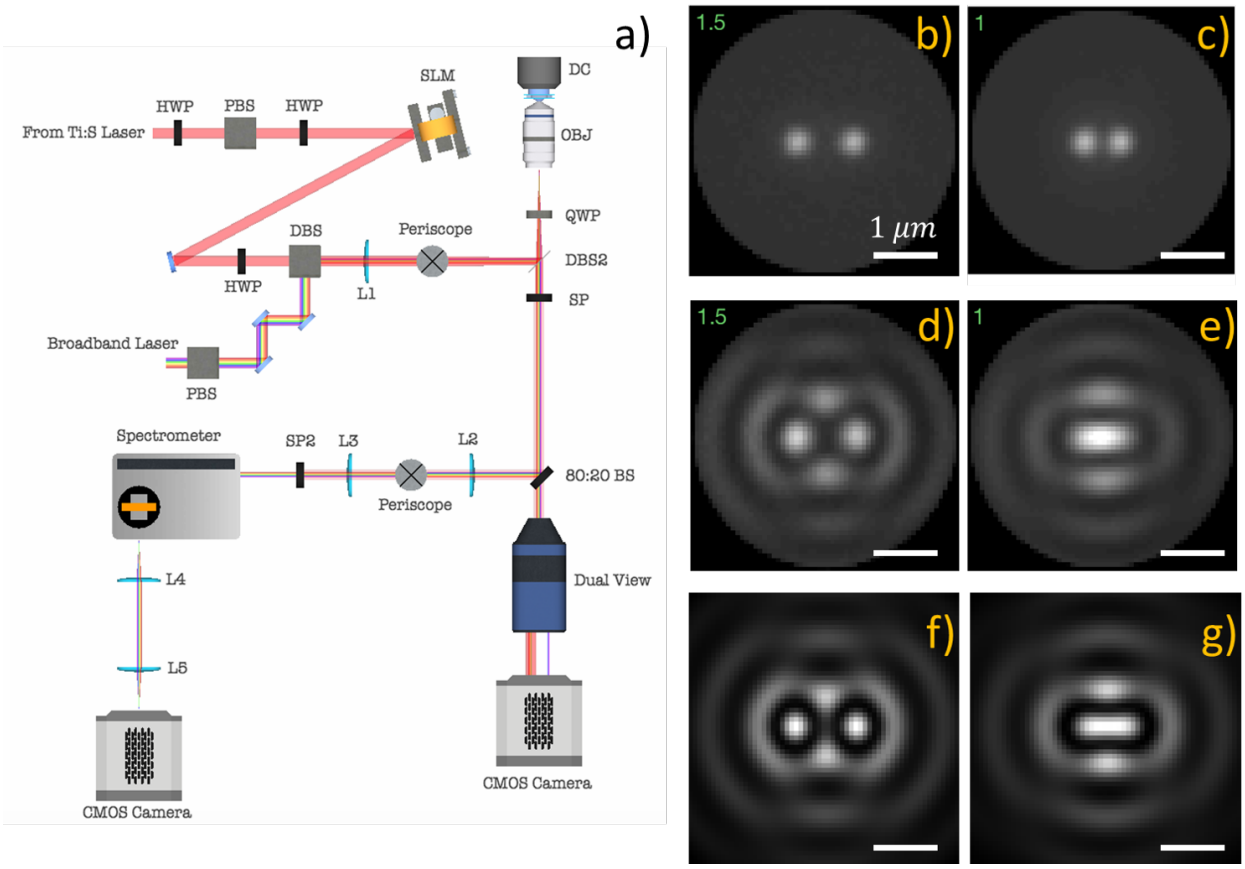

Figure A.1: **(a)** Optical trapping setup with simultaneous video microscopy and backscattered spectral measurements. HWP - half wave plate; QWP - quarter wave plate; SLM - spatial light modulator; DBS - dichroic beam splitter; PBS - polarizing beam splitter; SP - notch filter. **(b-c)** Incoherent light darkfield (NA = 1.27) images of a NP dimer at separations of 1.5λ (b) and λ (c). **(d-e)** Coherent light backscattered (NA = 1.27) images of NP dimer at separations of 1.5λ (d) and λ (e). **(f-g)** Simulated coherent light backscattered (NA = 1.00) images of NP dimer at separations of 1.5λ (f) and λ (g). See supplementary Videos 2 and 3 for a sequence of images for different inter-particle separations obtained with incoherent and coherent light [180].

Coherent imaging of OM arrays. The optically trapped 150 nm diameter Ag nanoparticles in our experiments rotate, translate, and dynamically reconfigure in the water solution due to thermal energy of the solution (*i.e.* undergo Brownian motion)[76, 160, 9]. Therefore, darkfield microscopy videos (*e.g.* see Supplementary Video 1 [180]) typically show particle arrays with fluctuating configurations where the probability of each specific configuration depends on the inter-particle forces. Particle separations with integer multiples of the trap-

ping wavelength in the solvent medium $\lambda = \lambda_{laser}/n$, where n is the index of refraction, are favored due to optical binding[61, 20, 148, 149, 150].

The individual images containing two randomly fluctuating particles in the optical trap were processed by the following protocol: (i) the particle pair was tracked in the images obtained with incoherent light using Mosaic (ImageJ); (ii) the particles were centered with respect to their "center of mass" and rotated with respect to the orientation of the pair; (iii) the oriented images were averaged in bins conditioned on inter-particle separation to dramatically improve the signal-to-noise ratio of the images. See the Supplementary Information for further details[180]; see Video 1 for the raw data and Videos 2, 3 for averaged and aligned videos measured with incoherent and coherent light, respectively.

Figures A.1b,c show averaged dark-field images measured with incoherent light where the pair of particles is separated by 1.5λ and λ, respectively. The images show that the incoherent light scattered from each of the particles is manifested as well-defined Gaussian spots regardless of inter-particle distance to separations as small as 300 nm. Figures A.1d,e show averaged images measured with coherent light are shown for the same separations. The images for particles separated by $r = 1.5\lambda$ show two distinct spots, ostensibly near the particle locations, and a pattern of interference fringes around the dimer with two brighter spots on the perpendicular bisector between the particles. The image for $r = \lambda$ shows a single elongated spot between the particle locations that is reminiscent of σ-bonding orbitals in diatomic molecules[181]. The fringe pattern also changes at $r = \lambda$ compared to $r = 1.5\lambda$ with the first ring of fringes becoming ellipsoidal.

We performed GMMT calculations to generate simulated images for the particle configurations shown in Figure A.1b-e ($\lambda = 800$ nm). The simulated images closely match each of our experimental results measured with coherent light scattered from the OM arrays when the simulated numerical aperture (NA) is set to 1.00. Fresnel reflection losses at high NA inside the objective may reduce the effective NA of the experimental image. Also, the particle

images may be displaced from their true positions due to spin-to-orbit angular momentum conversion of scattered light and the associated tilt of the scattered wavefront and shifting of the particle images in the transverse plane[182]. Our imaging may capture an aspect of this displacement that blurs the averaged images. The image averaging procedure will also cause blurring. Nevertheless, Figure A.1 demonstrates that the image of a pair of nanoparticles illuminated by coherent light depends on the distance between them.

We also recorded images of small 2D OM arrays illuminated by spatially coherent light. Figure A.2a-c shows aligned and averaged coherent images for three different arrays; the associated averaged incoherent darkfield illumination images are shown in the insets. A real-space lattice fitting procedure was employed to detect ordered arrays and define the rotation and translation required for the averaging of each raw experimental image (see SI for details)[180]. The OM array in Figure A.2a is a 6-particle triangular configuration, as shown by the incoherent darkfield image in the inset. The positions of the corner particles are bright in the coherent image, while the positions of the three interior particles are dimmer by comparison. Moving away from the array, bright fringes are visible with maximum intensity located outward from the three central particles in the triangle. The array in Figure A.2b is a different six-particle arrangement (termed a chevron) with a concave edge as shown in the inset. Its coherent image contains a smooth bright fringe following the arc of positions of the outer particles with the center particle appearing dark. There are exterior fringes projected outward from the bisectors of each of the 5 exterior edges of the array, and a bright spot located at the 3 o'clock position. Figure A.2c shows the coherent image for the 7-particle hexagonal array obtained by adding a particle to the array in Figure A.2b. The coherent image is annular with a dark center that resembles a benzene π-orbital[181]. There are fringes arranged parallel to each edge of the hexagon. The images in Figure A.2 a, b, and c have 3-fold, 2-fold, and 6-fold rotational symmetry, respectively, which matches the symmetry of each particle array. Figures A.2d-f show simulated coherent backscattering images ($\lambda = 800$

nm; $NA = 1.00$) for each of the experimentally measured arrays in Figure A.2a-c. The agreement between the measured and simulated images is very good.

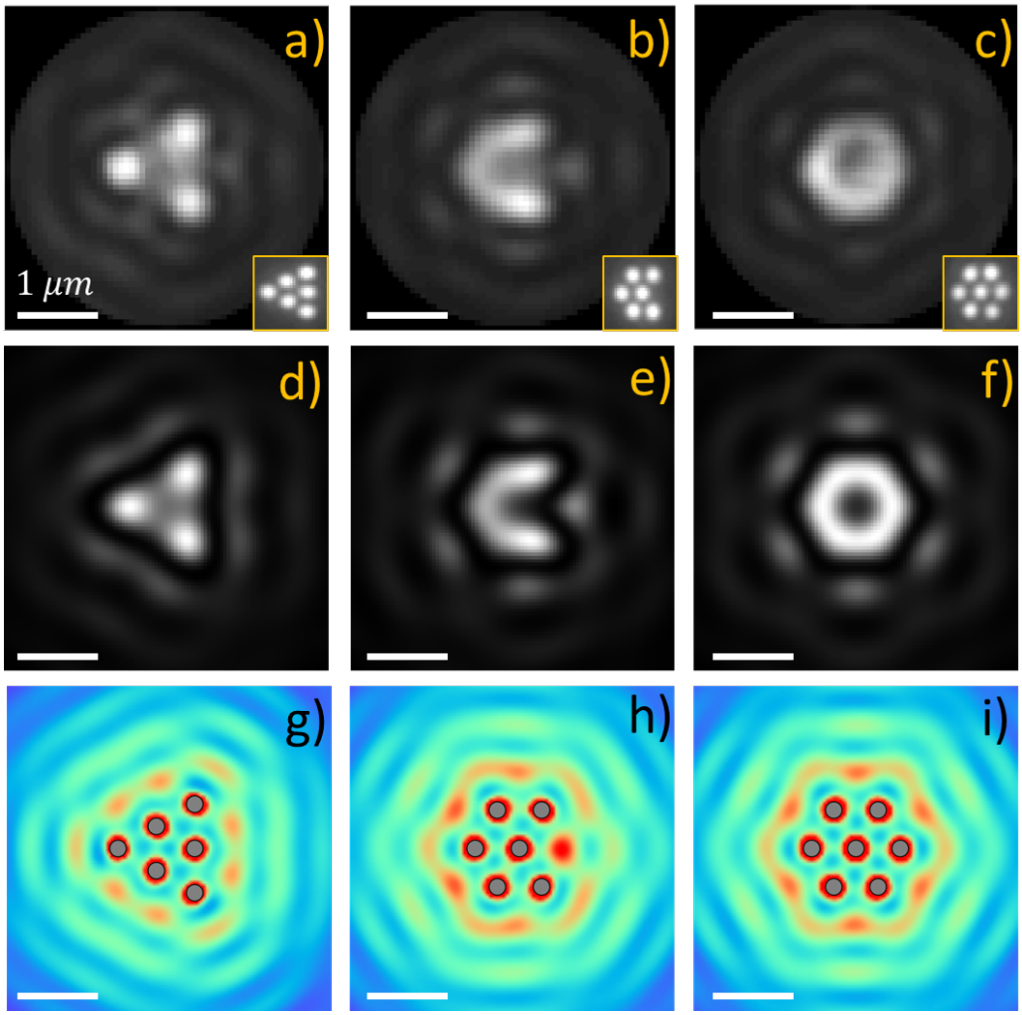

Figure A.2: OM arrays imaged with coherent light and comparison to the simulated electric field intensity. **(a-c)** Experimental coherent backscattered images of OM arrays with 6 (a-b) and 7 (c) particles. The insets show the corresponding averaged incoherent (darkfield) images. **(d-f)** Simulated coherent backscattered images each of the three OM arrays as panels a, b, and c, respectively. **(g-i)** Simulated electric field intensity (color: red to blue) at and around each of the OM arrays (near-field and far-field) for comparison with the results of coherent imaging. The nanoparticles are gray filled circles.

Figures A.2g-i show the simulated electric field intensity, $|E|^2$ at and around each of the three arrays for comparison with the experimental and simulated coherent backscattering images. Comparison of the coherent images in Figures A.2a-c (experimental) and d-f

(simulated) with the electric field distributions in Figures A.2g-i shows that they are clearly different inside the OM array, but become more similar moving outward. Figure A.2g exhibits two local intensity maxima outside each edge of the triangle that are in a similar location to bright fringes in the experimental and simulated coherent images. The intensity maxima just outside the array in Figure A.2h-i are also coincident with fringes in the measured and simulated coherent images.

The electric field intensity distribution is related to the coherent images of OM arrays by far-field interference[183]. For plane-wave illumination with incident electric field E_0 and wavevector k the electric field intensity at a point (ρ, ϕ) in the transverse plane is given by[2]

$$I(\rho, \phi) = E_0^2 + 2E_0|\tilde{A}|\frac{\cos(k\rho + \varphi_s)}{k\rho} \tag{A.1}$$

where $\tilde{A}$ is a complex constant related to the nanoparticle's polarizability and φ_s is a phase shift factor. Meanwhile, the field in the image plane scattered by a point dipole $\boldsymbol{\mu}_i$ located at the origin (in the paraxial limit) is[2]

$$\boldsymbol{E}(\rho, \phi) = \tilde{B}\frac{J_1[k\rho\sin(\theta_{\mathrm{obj}})]}{k\rho}\boldsymbol{\mu} \tag{A.2}$$

where $\tilde{B}$ is a complex constant, J_1 is a Bessel function, and θ_{obj} is the collection angle of the microscope objective. Replacing the Bessel function by its asymptotic form and including the electric field reflected off the water-glass interface, $\boldsymbol{E}_r$, the intensity is

$$I(\rho, \phi) \propto E_r^2 + 2Re(\boldsymbol{E}_r \cdot \tilde{B}^*\boldsymbol{\mu})\frac{\cos(k\rho\sin(\theta_{\mathrm{obj}}) + \pi/4)}{(k\rho)^{3/2}} + O\left(\frac{1}{(k\rho)^3}\right) \tag{A.3}$$

Comparing equation A.3 to equation A.1 (and ignoring the $|\mu|^2$ term) shows that for a perfect objective ($sin(\theta_{obj}) = 1$; $N.A. = 1.33$) the coherent images and the electric field intensity for a single particle have identical features up to a constant phase shift, although the image intensity modulation falls off faster as $\rho^{3/2}$. Equations A.1-A.3 apply to single particles.

The difference between the coherent images and the near-field intensity in the interior of the array are due to the limited NA of our experimental coherent images.

Multi-particle scattering, induced polarization, and coupling in OM arrays. Figure A.1 and Video 3 demonstrate that the separation between particles has a dramatic effect on the images of coherent light scattered by a pair of particles. Figure A.2 demonstrates that the size and shape of the OM array does as well. However, the relative importance of interference and coupling in various characteristics of OM arrays needs to be established. We performed GMMT calculations at a wavelength of 800 nm (600 nm in water) for ordered OM arrays with a lattice spacing of 600 nm with 1-7 particles to facilitate a quantitative comparison between the light scattered by OM arrays with different numbers of particles. The simulated OM arrays have the structures and orientations shown in Figure A.3a. Projections of the scattered intensity onto the y-z plane are shown in Figure A.3b-c when normalized to 1 (A.3c), and by the number of particles (A.3b). The full 3D far-field scattering profiles for 1-7 particles are shown in the SI [180]. A single particle scatters in all directions, although there is a greater scattering intensity in the forward and backward ($\pm z$; up/down) directions than in the sideways (y; left/right) directions. The pattern is reminiscent of a dipole emitter oriented perpendicular to the incident beam propagation direction. However, it is altered due to the higher order (*e.g.* quadrupole) modes of the generalized Mie theory description of a single 150 nm diameter Ag NP, and by the broken symmetry between forward and backward scattering. As more particles are added to the OM array, the scattering intensity develops a strong lobe-structure with maxima in the forward ($+z$) and backward ($-z$) directions, and smaller maxima in the sideways ($\pm y$) directions. The change going from 2 to 3 particles is particularly striking and notable because this is the first array where a particle is added offset from the x axis and also where multi-particle scattering and many-body induced polarizations occur.

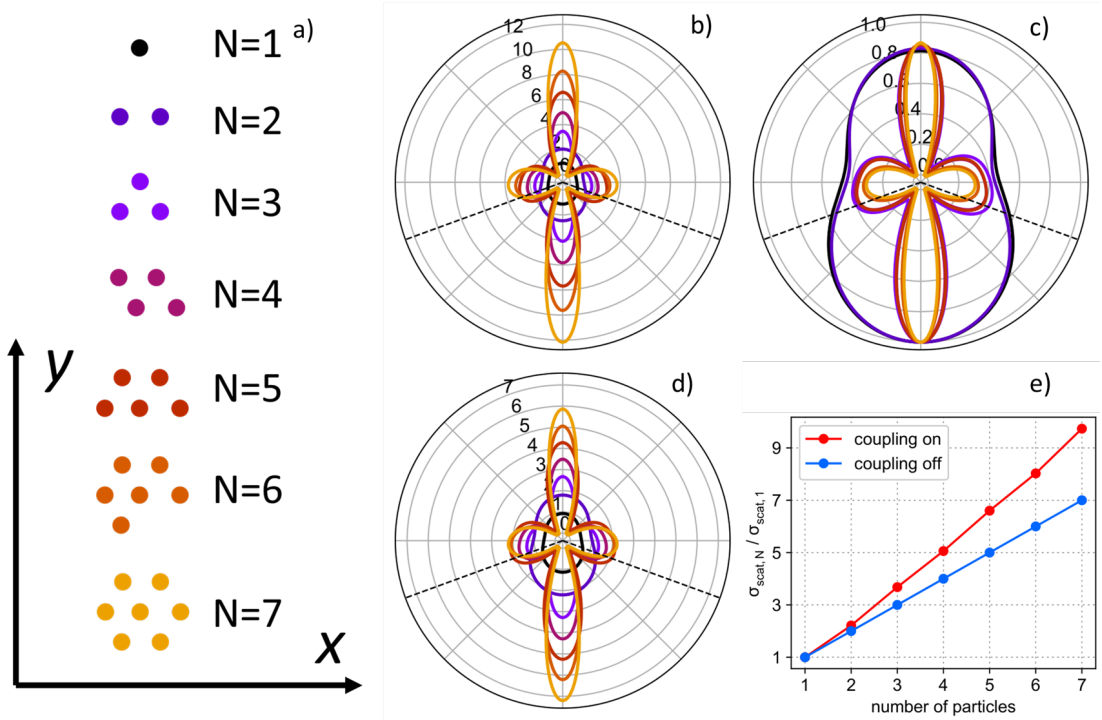

Figure A.3: The effect of electrodynamic coupling as seen in projections of the far-field angular scattering (λ = 800 nm; 600 nm in water) onto the yz plane from NP arrays with 1-7 particles. (a) OM arrays (lattice spacing = 600 nm) and color coding for (b-d). The incident field propagates along the z direction (upward on the page). (b) Angular scattering normalized by the number of particles in the array. (c) Angular scattering normalized to unity. (d) The same as (b), but with interparticle coupling disabled. Comparing (b) to (d) shows that coupling increases the strength of the far-field scattering. On the other hand, coupling does not significantly change the shape of the angular fields. (e) Total scattering normalized by single particle scattering with coupling enabled (red) and disabled (blue). In simulations where coupling is enabled, the scattering increases super-extensively

Figures A.3b-c show that the directional scattering from an OM array is altered significantly compared to a single particle. We modified the calculations in Figures A.3b, c by disabling coupling (*i.e.* induced polarization from particle-particle scattered fields) between the particles so that the polarization induced in each particle is only due to the incident field. The results are shown in Figures A.3d, e. The shape of the angular scattering profile is nearly identical, but the magnitude is 2-fold smaller than when coupling is allowed. Specifically, the total scattering cross section, σ_N, (at a wavelength matching the lattice spacing) of an OM array with N particles is directly proportional to N ($\sigma_N = N\sigma_1$) with coupling

disabled, while σ_N grows super-extensively (*i.e.* faster than N) with coupling enabled.

We also repeated our calculations of coherent images with coupling disabled to determine if the images are affected. We find that the resulting images are nearly identical to the results shown in Figures A.1-A.2 with coupling enabled (see SI) [180]. Essentially, only the total scattered intensity changes (increases) with coupling.

The results in Figures A.1 through A.3 demonstrate that the imaging and directionality of light scattered by OM arrays are primarily influenced by interference, and that electrodynamic coupling changes the magnitude but not the spatial characteristics of the scattered coherent light. There are two (limiting) cases where electrodynamic coupling between nanoparticles is particularly important: (i) when inter-particle separations are small compared to the wavelength of light, retardation can be neglected and the interaction between particles can be treated as quasi-static; *i.e.* as between the surface charges of the two particles in a pair or dimer[170, 171]; (ii) on the other hand, large field enhancements can occur in extended, regularly spaced arrays of particles at wavelengths near the array spacing due to constructive interference[184, 172].

Spectral dependence of electrodynamic coupling. We have shown that electrodynamic coupling, where the induced polarization is influenced by the fields scattered between particles, leads to increased scattering of coherent light at the trapping laser wavelength (800 nm; 600 nm in water) in OM arrays, and now turn our attention to the origin of the coupling. We carried out GMMT calculations to study the effects of the number of particles, size of particles, and excitation wavelength on the coherent light scattered by OM arrays. Figure A.4a shows the ratio of the total field to the incident field at the (empty) location of the center particle in a hexagonal 6-particle OM array for wavelengths of 800 nm (violet), 760 nm (blue), and 580 nm (red). For $\lambda = 800$ nm and $\lambda = 760$ nm the enhancement is small (≈ 7 percent) with a single particle nearby. However, every particle added to the

array contributes to a growing enhancement so that the scattered field is approaching half the magnitude of the incident field for 6 nearby particles, and the growth from 1 to 6 is nonlinear. Conversely, at $\lambda = 580$ nm the total field at the location of the vacant site at the center of the OM array diminishes monotonically with increasing particle number.

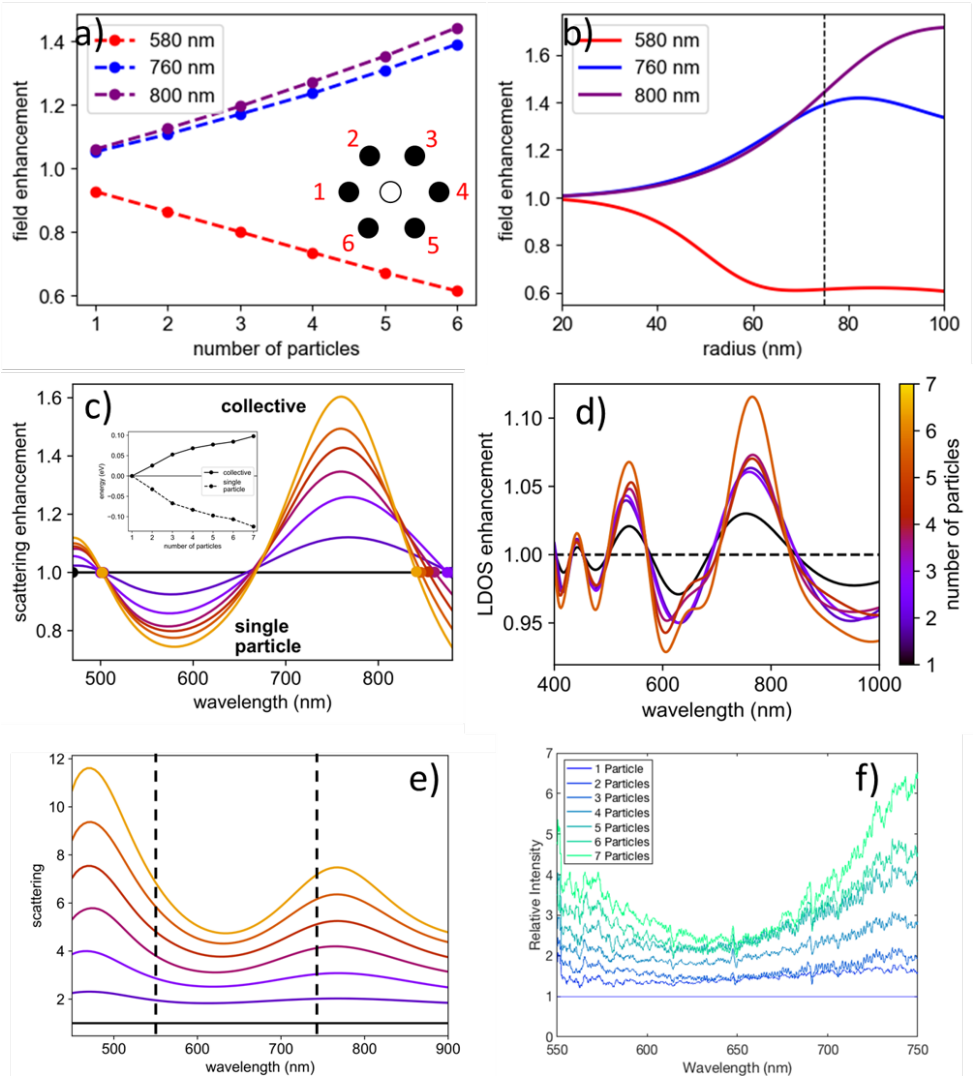

Figure A.4: Electrodynamic coupling and emergence of a collective scattering mode in OM arrays. **(a)** Electric field enhancement at the vacant location of the center of a hexagonal OM array for varying number of particles at incident vacuum wavelengths of 800 nm (violet), 760 nm (blue), and 580 nm (red). **(b)** Six-particle results from panel (a) repeated for varying particle-size (radius) at wavelengths of 800 nm (violet), 760 nm (blue), and 580 nm (red). **(c)** Simulated scattering enhancement as a function of wavelength in OM arrays versus number of particles. The inset shows the integrals for the wavelength ranges corresponding to the (i) single-particle Mie resonance and the (ii) collective mode resonance resulting from electrodynamic coupling. **(d)** Local density of (electromagnetic) states enhancement in OM arrays for 1-7 particles **(e)** Simulated wavelength-dependent total scattering of the NP arrays normalized by particle number. Note the spectral range of the experiment corresponds to that between the dashed vertical lines. **(f)** Experimental back-scattering spectra of NP arrays normalized by a 1NP spectra measured with spatially coherent light.

Figure A.4b shows the six-particle GMMT simulation of field enhancement at the vacant site as a function of particle radius ranging from 20 nm to 100 nm for the same three wavelengths as in Figure A.4a. The dependence of the field enhancement on particle size is nonlinear at each wavelength. With $\lambda = 800$ nm the magnitude of the field enhancement increases monotonically with particle size, while for $\lambda = 760$ nm the field enhancement reaches a peak near 80 nm radius before decreasing slightly. Conversely, the strength of the electric field decreases with increasing particle size for $\lambda = 580$ nm. This result follows from changes in the scattering cross sections as the volume, changing $\propto r^3$, in addition to the dipolar resonance red-shifting with increasing size. Figures A.4a-b show that significant electrodynamic coupling occurs even in small arrays (2-7 particles) due to the combined scattering from several neighbors for particles larger than ≈ 50 nm in radius.

Figure A.4c shows the scattering enhancement of spatially coherent broadband light (compared to N-fold multiplication of the single-particle scattering) as a function of wavelength for OM arrays with 1-7 particles. Consistent with the results in Figure A.3e, the scattering grows super-extensively at wavelengths near the trapping laser wavelength. The dependence of this scattering enhancement on electrodynamic coupling suggests that it is collective in nature. Figure A.4c also shows that the scattering near the single-particle Mie resonance decreases as the number of nanoparticle constituents in the OM array increases. The inset in Figure A.4c shows the integral of the scattering enhancement for the collective and single-particle resonances. As the number of particles increases, the integral of the collective resonance enhancement steadily increases while the integral of the single-particle resonance diminishes.

The local density of (electromagnetic) states (LDOS) at a certain location within or near an OM array controls the emission rate of a dipole emitter placed at that location[185, 186]. In the limit of large arrays of plasmonic particles the local density of states enhancement for specific in-plane wave vectors occurs together with large field enhancements[173]. Fig-

ure A.4d shows the measured local density of states enhancement (LDOS) in an OM array for 1-7 nanoparticles. This is consistent with the significant field enhancement shown in Figures A.4a-b. As more particles are added to the OM array, LDOS enhancement becomes increasingly prominent near the trapping laser wavelength.

Experimental and simulated scattering spectra. To experimentally determine the wavelength-dependent scattering enhancement in OM arrays, we measured backscattered spectra using a spatially coherent broadband source. A backscattering geometry was chosen for excitation and detection where the direction of propagation is normal to the plane of the array so that each particle in the array is excited with the same phase. Although we anticipate a scattering enhancement at wavelengths near that of the trapping laser (because it defines the characteristic optical binding distance), the trapping laser wavelength needs to be filtered out because it is much more intense than the coherent broadband source. We employed a pulsed supercontinuum fiber laser (Fianium WL400-4-PP), operating at maximum power with a 5.00 MHz pulse repetition rate, coupled to a computer-controlled variable interference filter (Fianium SuperChrome) set to its maximum bandwidth. As shown in Figure A.1a, the broadband beam was directed to travel collinear with the trapping laser into the optical trap, and the back-scattered light was sent through a dichroic beam splitter and notch filter (Semrock StopLine NF03-785E-25) to remove the trapping laser intensity from the back-scattered light. 20% of the light was directed towards a CMOS array detector (Andor Neo) for imaging and the remaining 80% of light was directed towards a spectrograph (Andor Shamrock SR-193i-B1-SIL). A pair of relay lenses (Thorlabs AC508-100-B-ML) with focal length f=100 mm were then used to bring the resulting spectrum from the spectrograph to a second CMOS array detector (Andor NEO). The imaging and spectral CMOS detectors were synchronized so that the spectral measurement was acquired at the same frame rate as the imaging. Both detectors were started and 1000 images and spectra were acquired at

160 fps once an OM array had formed. The spectra were classified by (i) specific numbers of nanoparticles, and (ii) as arising from ordered *vs.* disordered arrays based on the fitting error (*i.e.* deviations of the particle positions from the lattice) resulting from real-space lattice fitting of the OM arrays in each frame.

Figure A.4e shows simulated backscattered spectra for an OM array consisting of 1-7 particles normalized by the single particle spectrum. Peaks in scattering enhancement emerge near 500 nm and 800 nm as particles are added to the array. The experimentally measurable range of wavelengths is indicated by the black vertical dashed lines in Figure A.4e. Figure A.4f shows the experimentally measured backscattered spectra normalized by the single-particle scattering spectrum. The experimental and simulated spectra of the OM arrays are in good agreement.

Polarization and scattering enhancement in large OM arrays. We extended our investigation to large hexagonal arrays of 150 nm Ag NP's to elucidate the connection between the electrodynamic properties of small OM arrays and surface lattice resonances (SLR's) in the infinite lattice limit. Figure A.5a shows the average enhancement of the induced polarization (*i.e.* the proportion of the average induced-polarization of the particles to the induced-polarization of an isolated particle in the same incident field) in a hexagonal NP array with 469 particles and a lattice constant varying from 400 nm to 900 nm. The enhancement of the induced-polarization, and hence electrodynamic coupling as a result of multi-particle scattering, grows slowly for lattice spacings from 400 nm to 600 nm before rapidly increasing to a peak at 667 nm. It then declines rapidly to a value below 1, and then increases back toward 1 with increasing spacing. Figures A.5b-c show visualizations of the induced-polarization enhancement of the particles in the array for lattice spacings of 600 nm and 667 nm, respectively. At 600 nm the induced-polarization enhancement has a six-fold symmetric pattern and is small. At 667 nm (the spacing where the induced-polarization

enhancement is maximized) the maximum enhancements are nearly radially symmetric with the strongest (nearly 10-fold) enhancements at the center of the array.

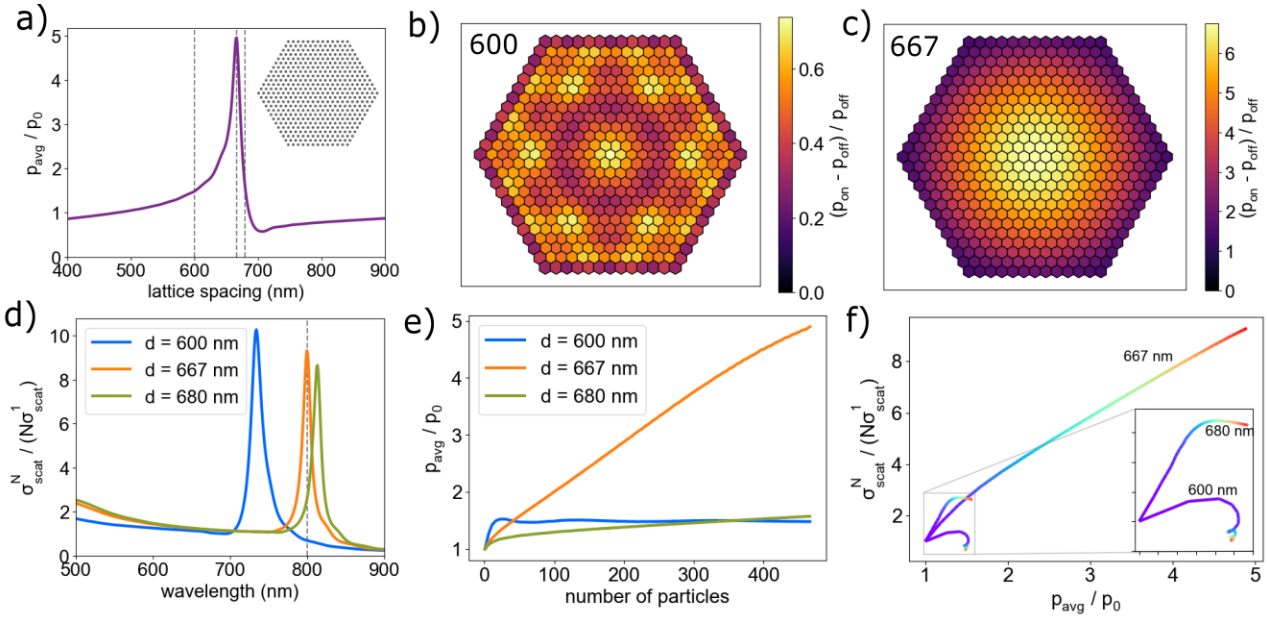

Figure A.5: Induced-polarization and scattering enhancement in large hexagonal NP arrays. **(a)** Average induced-polarization enhancement in a large (469 particles) hexagonal NP array with variable inter-particle spacing. The inset shows the arrangement of particles. **(b)** Visualization of induced-polarization enhancement as a result of multi-particle scattering in a large hexagonal NP array with 600 nm spacing. **(c)** Visualization of induced-polarization enhancement in a large hexagonal NP array with 667 nm spacing. **(d)** Enhancement of the scattering cross section per particle for hexagonal arrays with lattice constants of $d = 600$ nm, $d = 667$ nm, and $d = 680$ nm. **(e)** Average induced-polarization enhancement of NP's in a hexagonal array as it is built particle-by-particle for lattice constants of $d = 600$ nm, $d = 667$ nm, and $d = 680$ nm. **(f)** Enhancement of the scattering cross section per particle versus average polarization-enhancement of NP's in a hexagonal array as it is built particle-by-particle for lattice constants of $d = 600$ nm, $d = 667$ nm, and $d = 680$ nm.

We simulated scattering spectra for arrays with the three separations marked with vertical dashed lines. Figure A.5d shows the results obtained from GMMT simulations of 469-particle hexagonal arrays (in water) for wavelengths between 500 nm and 900 nm. The resonance peaks occur at 733 nm, 799 nm, and 812 nm for lattice spacings of 600 nm (blue), 667 nm (orange), and 680 nm (green), respectively. There is a nearly linear relationship between the resonance wavelength and lattice spacing over the range of lattices studied.

We also conducted GMMT simulations as NP arrays were built particle-by-particle to investigate how the electrodynamic properties of the arrays scale with the number of nanoparticle elements, N. Figure A.5e shows plots of induced-polarization enhancement versus number of particles. When $d = 600$ nm (the lattice constant is equal to the inter-particle spacing) the induced-polarization enhancement increases rapidly for a small number of particles before leveling off and decreasing slightly. For $d = 667$ nm the polarization enhancement increases more slowly for a small number of particles compared to $d = 600$ nm, but continues to increase steadily becoming 4-fold larger than the result for $d = 600$ nm with 469 particles. In contrast, the induced-polarization enhancement only increases slightly at $d = 680$ nm.

Figure A.5f shows plots of scattering enhancement versus polarization enhancement for hexagonal arrays with a varying number of particles (indicated by the purple-to-red colorscale) for an incident wavelength of 800 nm and lattice spacings of $d = 600$ nm, $d = 667$ nm, and $d = 680$ nm. The scattering enhancement increases steadily and monotonically with polarization enhancement for $d = 667$ nm. However, scattering enhancement increases up to a certain number of particles before decreasing for $d = 600$ nm and $d = 680$ nm. These contrasting behaviors indicate *that an increase in induced-polarization does not necessarily result in increased total scattering.* The *phase of the induced-polarizations* of the particles in the array shows that the collective excitation in the 469-particle array: (i) lags behind the phase of the incident light for $d = 600$ nm; (ii) is close to the phase of the incident light for $d = 667$ nm; and (iii) is advanced compared to the phase of the incident light for $d = 680$ nm.

Discussion and Conclusions. We have shown that induced-polarizations and electrodynamic coupling versus single scattering and interference have distinct effects on the scattering of coherent light by OM arrays. Figures A.1 and A.2 show that imaging the backscattering of the coherent trapping laser from an OM array gives dramatically different results versus imaging the particles illuminated by an incoherent source. Furthermore, the coherent images

of the OM arrays have features in common with the near-field electromagnetic field intensity because both are controlled by similar phase-dependent relationships according to Equations A.1 and A.3. Figure A.3 shows that multiple scattering and electrodynamic coupling has a minimal effect on the (qualitative) spatial characteristics of coherent light scattered by OM arrays; *i.e.* on how the images look. However, coupling leads to an enhancement of the total scattering at the trapping laser wavelength. Figure A.4 demonstrates that while coupling enhances scattering at wavelengths near the trapping laser wavelength, total scattering is not enhanced at all wavelengths. Figure A.5 shows how the electrodynamic properties of OM arrays evolve as the arrays grow. For large hexagonal arrays the collective scattering resonance wavelength (in a water medium with $n = 1.33$) is significantly shifted compared to the lattice spacing. However, our results show that maximization of scattering still occurs concurrently with large polarization enhancements due to constructive interference of the light scattered by neighboring particles.

Figure A.4a shows that each particle added to the OM array increases the electric field strength at the vacant central site of a hexagonal array for trapping laser wavelengths ($\lambda/1.33$) near the 600 nm (fixed) particle spacing. For the geometry shown in Figure A.4a, the light scattered from each particle has the same phase at the central location marked in that figure because that location is equidistant from all of the particles. The relative phase between the incident and scattered light, however, depends on the lattice spacing in comparison to the wavelength of the excitation. For the trapping laser, the laser wavelength (accounting for the index of refraction of the medium) and lattice spacing are nearly equal and the scattered light interferes constructively with the incident light. At 560 nm the interference is destructive and the field at the location of the vacant central site is diminished.

The total strength of the coupling also depends on the size (and polarizability) of the particles. Figure A.4b shows that the scattering cross sections of the 150 nm diameter particles used in our experiments and most calculations are large enough to result in significant field

enhancement in OM arrays, whereas Ag nanoparticles with diameters under 100 nm create almost none. Therefore, the geometry, inter-particle separations, and choice of particles in OM arrays contribute to the significant electrodynamic coupling that we report here.

There is an important relationship between interference and coupling that can be understood within the point dipole approximation[149]. Consider a two-dimensional array of particles with isotropic polarizability α arranged in the transverse plane of an electromagnetic plane-wave with wavelength λ_0 . The induced-polarization, $\mathbf{p}_i$, of particle i is proportional to the total electric field at the location of particle i, $\mathbf{p}_i = \alpha \mathbf{E}_{r=r_i}$ with

$$\begin{aligned} \mathbf{E}_{r=r_i} &= \mathbf{E}_0 + \alpha \sum_{j \neq i} \mathbf{G}(r_i, r_j) \mathbf{E}_{r=r_j} \\ &\approx \mathbf{E}_0 \left[1 + \alpha \sum_{j \neq i} \mathbf{G}(r_i, r_j) + \alpha^2 \sum_{j \neq i} \sum_{l \neq j} \mathbf{G}(r_i, r_j) \mathbf{G}(r_j, r_l) + ... \right] \end{aligned} \tag{A.4}$$

where $\mathbf{E}_0$ is the incident electric field and $\mathbf{G}(r_i, r_j)$ is the Green's Function tensor that propagates the scattered field at position r_j resulting from a dipole at position r_i[149, 13]

$$\mathbf{G}_{lm} = \frac{e^{ikR}}{4\pi\epsilon_0\epsilon_m R^3} \left[(3 - 3ikR - k^2R^2) \frac{R_l R_m}{R^2} + (k^2R^2 + ikR - 1)\delta_{lm} \right] \tag{A.5}$$

where l and m are polarization directions of the field, $R = |r_i - r_j|$ is the distance between the two particles, and k is the wave-vector of the incident light. At single-wavelength distances $kR = 2\pi$ where the far-field terms in the propagator with $\frac{1}{R}$ dependence give the largest contribution, although all terms are significant for OM systems. Due to the e^{ikR} phase factor in equation A.5, the induced-polarization of a particle in an OM array will have the largest contribution from light scattered by neighboring particles when all of the scattered contributions are in-phase, *i.e.* when they are interfering constructively.

Equation A.4 is an approximate solution for the scattered field at the location of a particle in an OM array expanded in orders of scattering. Each scattering order is weaker

by a factor of αG. Based on the results in Figure A.4a, we estimate that the terms in $\alpha G \approx 0.05$ As an OM array grows, an increasing number of terms contribute to higher-order (and multi-particle) scattering. In the limit of large lattices, as demonstrated in Figure A.5, higher-order and multi-particle scattering (and hence many body interactions) and what we term electrodynamic coupling makes the dominant contribution to the induced-polarization of each particle. That is, multiple-scattering cannot be ignored.

Both interference and electrodynamic coupling play important roles in understanding light scattered by OM arrays, analogously to SLR's. Interference dramatically alters the spatial profile and directionality of the light scattered by OM arrays. Furthermore, while the magnitude of the field scattered from a single particle is small compared to the incident field, the combined contributions from several nearby particles interfering constructively leads to significant field enhancement and coupling. This is especially true for large hexagonal arrays where the induced-polarization becomes $>$ 5x larger than that of an isolated particle under the same illumination. These field enhancements and coupling could also be exploited for applications in nonlinear optics, where the phenomena have an E^{2n} dependence, with n indicating the order of nonlinearity[187, 188].

REFERENCES

[1] Max Born and Emil Wolf. *Principles of Optics, 6th edn.* Pergamon Press, 1970.

[2] Lukas Novotny and Bert Hecht. *Principles of nano-optics.* Cambridge University Press, 2012.

[3] McGraw-Hill. *McGraw Hill Encyclopedia of Science & Technology.* McGraw-Hill Professional, 2007.

[4] Gustav Mie. Beiträge zur optik trüber medien, speziell kolloidaler metallösungen. *Annalen der Physik*, 330(3):377–445, 1908.

[5] John D. Joannopoulos, Steven G. Johnson, Joshua N. Winn, and Robert D. Meade. *Photonic Crystals.* Princeton University Press, 2011.

[6] Jiajing Li, Tian-Song Deng, Xiaoying Liu, James A. Dolan, Norbert F. Scherer, and Paul F. Nealey. Hierarchical assembly of plasmonic nanoparticle heterodimer arrays with tunable sub-5 nm nanogaps. *Nano Letters*, 19(7):4314–4320, jun 2019.

[7] Saman Jahani and Zubin Jacob. All-dielectric metamaterials. *Nature Nanotechnology*, 11(1):23–36, jan 2016.

[8] Gabriel Castellanos, Shunsuke Murai, T.V. Raziman, Mohammad Ramezani, Shaojun Wang, Alberto Curto, and Jaime Gómez Rivas. Exciton-Polaritons with magnetic and electric character in all-dielectric metasurfaces, 2021.

[9] John Parker, Curtis W. Peterson, Yuval Yifat, Stuart A. Rice, Zijie Yan, Stephen K. Gray, and Norbert F. Scherer. Optical matter machines: angular momentum conversion by collective modes in optically bound nanoparticle arrays. *Optica*, 7(10):1341, oct 2020.

[10] Susan E. Skelton Spesyvtseva and Kishan Dholakia. Trapping in a material world. *ACS Photonics*, 3(5):719–736, may 2016.

[11] A. Ashkin. Acceleration and trapping of particles by radiation pressure. *Physical Review Letters*, 24(4):156–159, jan 1970.

[12] The Nobel Prize in Physics 2018 (`https://www.nobelprize.org/prizes/physics/2018/summary/`), 2023.

[13] John David Jackson. *Classical Electrodynamics, 3rd Edition.* John Wiley & Sons, 1999.

[14] Sergey Sukhov, Alexander Shalin, David Haefner, and Aristide Dogariu. Actio et reactio in optical binding. *Optics Express*, 23(1):247, jan 2015.

[15] Yuval Yifat, Delphine Coursault, Curtis W. Peterson, John Parker, Ying Bao, Stephen K. Gray, Stuart A. Rice, and Norbert F. Scherer. Reactive optical matter: light-induced motility in electrodynamically asymmetric nanoscale scatterers. *Light: Science & Applications*, 7(1), dec 2018.

[16] Jun Chen, Jack Ng, Kun Ding, Kin Hung Fung, Zhifang Lin, and C. T. Chan. Negative optical torque. *Scientific Reports*, 4(1), sep 2014.

[17] Fei Han, John A. Parker, Yuval Yifat, Curtis Peterson, Stephen K. Gray, Norbert F. Scherer, and Zijie Yan. Crossover from positive to negative optical torque in mesoscale optical matter. *Nature Communications*, 9(1), nov 2018.

[18] Jun Chen, Shubo Wang, Xiao Li, and Jack Ng. Mechanical effect of photonic spin-orbit interaction for a metallic nanohelix. *Optics Express*, 26(21):27694, oct 2018.

[19] Sergey Sukhov and Aristide Dogariu. Non-conservative optical forces. *Reports on Progress in Physics*, 80(11):112001, sep 2017.

[20] Michael M. Burns, Jean-Marc Fournier, and Jene A. Golovchenko. Optical matter: Crystallization and binding in intense optical fields. *Science*, 249(4970):749–754, aug 1990.

[21] Arseniy I. Kuznetsov, Andrey E. Miroshnichenko, Yuan Hsing Fu, JingBo Zhang, and Boris Luk'yanchuk. Magnetic light. *Scientific Reports*, 2(1), jul 2012.

[22] M. Burresi, D. van Oosten, T. Kampfrath, H. Schoenmaker, R. Heideman, A. Leinse, and L. Kuipers. Probing the magnetic field of light at optical frequencies. *Science*, 326(5952):550–553, oct 2009.

[23] Tim H. Taminiau, Sinan Karaveli, Niek F. van Hulst, and Rashid Zia. Quantifying the magnetic nature of light emission. *Nature Communications*, 3(1), jul 2012.

[24] David J. Griffiths. *Introduction to Electrodynamics, 4th Edition*. Cambridge University Press, 2017.

[25] Lev Davidovich Landau, Evgeny Mikhailovich Lifshitz, and Lev Petrovich Pitaevskii. *Statistical Physics*. Pergamon, 1980.

[26] L D Landau, E.M. Lifshitz, and L. P. Pitaevskii. *Electrodynamics of Continuous Media*. Butterworth-Heinemann, 1995.

[27] E.M. Lifshitz and L. P. Pitaevskii. *Physical Kinetics*. Butterworth-Heinemann, 1995.

[28] H. C. van de Hulst. *Light Scattering by Small Particles*. Dover Publications, Inc., 1981.

[29] James A. Lock and Gérard Gouesbet. Generalized Lorenz-Mie theory and applications. *Journal of Quantitative Spectroscopy and Radiative Transfer*, 110(11):800–807, jul 2009.

[30] Daniel W. Mackowski and Michael I. Mishchenko. Calculation of the T matrix and the scattering matrix for ensembles of spheres. *Journal of the Optical Society of America A*, 13(11):2266, nov 1996.

[31] Yu lin Xu. Electromagnetic scattering by an aggregate of spheres. *Applied Optics*, 34(21):4573, jul 1995.

[32] Johannes Kepler. *De Cometis Libelli Tres*. Avgvst Vindelicorvm, 1619.

[33] John Parker. Miepy: Generalized multiparticle mie theory python module (`https://github.com/johnaparker/miepy`), 2020.

[34] John Parker. Stoked: Stokesian dynamics python module (`https://github.com/johnaparker/stoked`), 2020.

[35] Amos Egel, Krzysztof M. Czajkowski, Dominik Theobald, Konstantin Ladutenko, Alexey S. Kuznetsov, and Lorenzo Pattelli. SMUTHI: A python package for the simulation of light scattering by multiple particles near or between planar interfaces. *Journal of Quantitative Spectroscopy and Radiative Transfer*, 273:107846, oct 2021.

[36] Ardavan F. Oskooi, David Roundy, Mihai Ibanescu, Peter Bermel, J.D. Joannopoulos, and Steven G. Johnson. Meep: A flexible free-software package for electromagnetic simulations by the FDTD method. *Computer Physics Communications*, 181(3):687–702, mar 2010.

[37] Allen Taflove and Susan C. Hagness. *Computational Electrodynamics: The Finite-Difference Time-Domain Method*. Artech House, 2005.

[38] Allen Taflove, Steven G. Johnson, and Ardavan Oskooi. *Advances in FDTD Computational Electrodynamics: Photonics and Nanotechnology*. Artech House, 2013.

[39] This work was completed in part with resources provided by the University of Chicago Research Computing Center (`https://rcc.uchicago.edu/`), 2023.

[40] nanoComposix. *nanoComposix 2023 Standard Product Catalog*. available on nanocomposix.com, 2022.

[41] Precision spherical particles (`https://www.cospheric.com/`), 2023.

[42] Product catagories (`https://www.nanopartz.com/categories.asp`), 2023.

[43] Malvern Instruments Ltd. *Zetasizer Nano User Manual*. available on www.malvern.com, 2013.

[44] Carl Zeiss Microscopy GmbH. *Instruction Manual MERLIN®*. available on www.zeiss.com/microscopy, 2013.

[45] Kevin M. McPeak, Sriharsha V. Jayanti, Stephan J. P. Kress, Stefan Meyer, Stelio Iotti, Aurelio Rossinelli, and David J. Norris. Plasmonic films can easily be better: Rules and recipes. *ACS Photonics*, 2(3):326–333, feb 2015.

[46] Wolfgang Becker. *The bh TCSPC Handbook, 4th edition.* available on www.becker-hickl.com, 2010.

[47] PicoQuant(GmbH). *TimeHarp 260: User's Manual and Technical Data, Version 3.2.0.0.* available on www.picoquant.com, 2020.

[48] A. Ashkin, J. M. Dziedzic, and T. Yamane. Optical trapping and manipulation of single cells using infrared laser beams. *Nature*, 330(6150):769–771, dec 1987.

[49] Min-Cheng Zhong, Xun-Bin Wei, Jin-Hua Zhou, Zi-Qiang Wang, and Yin-Mei Li. Trapping red blood cells in living animals using optical tweezers. *Nature Communications*, 4(1), apr 2013.

[50] Itia A. Favre-Bulle, Alexander B. Stilgoe, Halina Rubinsztein-Dunlop, and Ethan K. Scott. Optical trapping of otoliths drives vestibular behaviours in larval zebrafish. *Nature Communications*, 8(1), sep 2017.

[51] Alexander S. Urban, Andrey A. Lutich, Fenando D. Stefani, and Jochen Feldmann. Laser printing single gold nanoparticles. *Nano Letters*, 10(12):4794–4798, oct 2010.

[52] Spas Nedev, Alexander S. Urban, Andrey A. Lutich, and Jochen Feldmann. Optical force stamping lithography. *Nano Letters*, 11(11):5066–5070, oct 2011.

[53] Jaekwon Do, Khalid N. Sediq, Kieran Deasy, David M. Coles, Jessica Rodríguez-Fernández, Jochen Feldmann, and David G. Lidzey. Photonic crystal nanocavities containing plasmonic nanoparticles assembled using a laser-printing technique. *Advanced Optical Materials*, 1(12):946–951, aug 2013.

[54] Ying Bao, Zijie Yan, and Norbert F. Scherer. Optical printing of electrodynamically coupled metallic nanoparticle arrays. *The Journal of Physical Chemistry C*, 118(33):19315–19321, aug 2014.

[55] Julián Gargiulo, Santiago Cerrota, Emiliano Cortés, Ianina L. Violi, and Fernando D. Stefani. Connecting metallic nanoparticles by optical printing. *Nano Letters*, 16(2):1224–1229, jan 2016.

[56] Ianina L. Violi, Julián Gargiulo, Catalina von Bilderling, Emiliano Cortés, and Fernando D. Stefani. Light-induced polarization-directed growth of optically printed gold nanoparticles. *Nano Letters*, 16(10):6529–6533, sep 2016.

[57] Julián Gargiulo, Ianina L. Violi, Santiago Cerrota, Lukáš Chvátal, Emiliano Cortés, Eduardo M. Perassi, Fernando Diaz, Pavel Zemánek, and Fernando D. Stefani. Accuracy and mechanistic details of optical printing of single Au and Ag nanoparticles. *ACS Nano*, 11(10):9678–9688, sep 2017.

[58] Uroš Delić, Manuel Reisenbauer, Kahan Dare, David Grass, Vladan Vuletić, Nikolai Kiesel, and Markus Aspelmeyer. Cooling of a levitated nanoparticle to the motional quantum ground state. *Science*, 367(6480):892–895, feb 2020.

[59] Lorenzo Magrini, Philipp Rosenzweig, Constanze Bach, Andreas Deutschmann-Olek, Sebastian G. Hofer, Sungkun Hong, Nikolai Kiesel, Andreas Kugi, and Markus Aspelmeyer. Real-time optimal quantum control of mechanical motion at room temperature. *Nature*, 595(7867):373–377, jul 2021.

[60] Felix Tebbenjohanns, M. Luisa Mattana, Massimiliano Rossi, Martin Frimmer, and Lukas Novotny. Quantum control of a nanoparticle optically levitated in cryogenic free space. *Nature*, 595(7867):378–382, jul 2021.

[61] Michael M. Burns, Jean-Marc Fournier, and Jene A. Golovchenko. Optical binding. *Physical Review Letters*, 63(12):1233–1236, sep 1989.

[62] Jack Ng, Z. F. Lin, C. T. Chan, and Ping Sheng. Photonic clusters formed by dielectric microspheres: Numerical simulations. *Phys. Rev. B*, 72:085130, Aug 2005.

[63] Shun-Fa Wang, Tetsuhiro Kudo, Ken ichi Yuyama, Teruki Sugiyama, and Hiroshi Masuhara. Optically evolved assembly formation in laser trapping of polystyrene nanoparticles at solution surface. *Langmuir*, 32(47):12488–12496, sep 2016.

[64] Aristide Dogariu, Sergey Sukhov, and José Sáenz. Optically induced 'negative forces'. *Nature Photonics*, 7(1):24–27, dec 2012.

[65] A. V. Ivlev, J. Bartnick, M. Heinen, C.-R. Du, V. Nosenko, and H. Löwen. Statistical mechanics where Newton's third law is broken. *Phys. Rev. X*, 5:011035, Mar 2015.

[66] Lukáš Chvátal, Oto Brzobohatý, and Pavel Zemánek. Binding of a pair of au nanoparticles in a wide gaussian standing wave. *Optical Review*, 22(1):157–161, feb 2015.

[67] Vítězslav Karásek, Martin Šiler, Oto Brzobohatý, and Pavel Zemánek. Dynamics of an optically bound structure made of particles of unequal sizes. *Optics Letters*, 42(7):1436, mar 2017.

[68] Stephen H. Simpson, Pavel Zemánek, Onofrio M. Maragò, Philip H. Jones, and Simon Hanna. Optical binding of nanowires. *Nano Letters*, 17(6):3485–3492, may 2017.

[69] Patrick Figliozzi, Nishant Sule, Zijie Yan, Ying Bao, Stanislav Burov, Stephen K. Gray, Stuart A. Rice, Suriyanarayanan Vaikuntanathan, and Norbert F. Scherer. Driven optical matter: Dynamics of electrodynamically coupled nanoparticles in an optical ring vortex. *Phys. Rev. E*, 95:022604, Feb 2017.

[70] Nishant Sule, Yuval Yifat, Stephen K. Gray, and Norbert F. Scherer. Rotation and negative torque in electrodynamically bound nanoparticle dimers. *Nano Letters*, 17(11):6548–6556, oct 2017.

[71] Fan Nan, Fei Han, Norbert F. Scherer, and Zijie Yan. Dissipative self-assembly of anisotropic nanoparticle chains with combined electrodynamic and electrostatic interactions. *Advanced Materials*, 30(45):1803238, sep 2018.

[72] Yoshihiko Arita, Ewan M. Wright, and Kishan Dholakia. Optical binding of two cooled micro-gyroscopes levitated in vacuum. *Optica*, 5(8):910, jul 2018.

[73] Vojtěch Svak, Jana Flajšmanová, Lukáš Chvátal, Martin Šiler, Alexandr Jonáš, Jan Ježek, Stephen H. Simpson, Pavel Zemánek, and Oto Brzobohatý. Stochastic dynamics of optically bound matter levitated in vacuum. *Optica*, 8(2):220, feb 2021.

[74] Jakob Rieser, Mario A. Ciampini, Henning Rudolph, Nikolai Kiesel, Klaus Hornberger, Benjamin A. Stickler, Markus Aspelmeyer, and Uroš Delić. Tunable light-induced dipole-dipole interaction between optically levitated nanoparticles. *Science*, 377(6609):987–990, aug 2022.

[75] Zijie Yan, Raman A. Shah, Garrett Chado, Stephen K. Gray, Matthew Pelton, and Norbert F. Scherer. Guiding spatial arrangements of silver nanoparticles by optical binding interactions in shaped light fields. *ACS Nano*, 7(2):1790–1802, feb 2013.

[76] Zijie Yan, Stephen K. Gray, and Norbert F. Scherer. Potential energy surfaces and reaction pathways for light-mediated self-organization of metal nanoparticle clusters. *Nature Communications*, 5(1), may 2014.

[77] Curtis W. Peterson, John Parker, Stuart A. Rice, and Norbert F. Scherer. Controlling the dynamics and optical binding of nanoparticle homodimers with transverse phase gradients. *Nano Letters*, 19(2):897–903, jan 2019.

[78] M. Nieto-Vesperinas, J. J. Sáenz, R. Gómez-Medina, and L. Chantada. Optical forces on small magnetodielectric particle. *Optics Express*, 18(11):11428, may 2010.

[79] Xiaohao Xu, Manuel Nieto-Vesperinas, Cheng-Wei Qiu, Xiaoshuai Liu, Dongliang Gao, Yao Zhang, and Baojun Li. Kerker-type intensity-gradient force of light. *Laser & Photonics Reviews*, 14(4):1900265, feb 2020.

[80] A. Ashkin and J. P. Gordon. Stability of radiation-pressure particle traps: an optical Earnshaw theorem. *Optics Letters*, 8(10):511, oct 1983.

[81] Jan Gieseler, Bradley Deutsch, Romain Quidant, and Lukas Novotny. Subkelvin parametric feedback cooling of a laser-trapped nanoparticle. *Physical Review Letters*, 109(10), sep 2012.

[82] Materials and methods and additional information are available in Supplementary Materials for *Magnetic field trapping and photonic Hall effect of silicon nanoparticles.*

[83] Masaru Onoda, Shuichi Murakami, and Naoto Nagaosa. Hall effect of light. *Phys. Rev. Lett.*, 93:083901, Aug 2004.

[84] Onur Hosten and Paul Kwiat. Observation of the spin hall effect of light via weak measurements. *Science*, 319(5864):787–790, feb 2008.

[85] D. Haefner, S. Sukhov, and A. Dogariu. Spin hall effect of light in spherical geometry. *Phys. Rev. Lett.*, 102:123903, Mar 2009.

[86] Jinli Ren, Yan Li, Yida Lin, Yi Qin, Rui Wu, Jinbo Yang, Yun-Feng Xiao, Hong Yang, and Qihuang Gong. Spin hall effect of light reflected from a magnetic thin film. *Applied Physics Letters*, 101(17):171103, oct 2012.

[87] Dongliang Gao, Ran Shi, Andrey E. Miroshnichenko, and Lei Gao. Enhanced spin hall effect of light in spheres with dual symmetry. *Laser & Photonics Reviews*, 12(11):1800130, sep 2018.

[88] R. Shi, D. L. Gao, H. Hu, Y. Q. Wang, and L. Gao. Enhanced broadband spin hall effects by core-shell nanoparticles. *Optics Express*, 27(4):4808, feb 2019.

[89] Jan Gieseler, Juan Ruben Gomez-Solano, Alessandro Magazzù, Isaac Pérez Castillo, Laura Pérez García, Marta Gironella-Torrent, Xavier Viader-Godoy, Felix Ritort, Giuseppe Pesce, Alejandro V. Arzola, Karen Volke-Sepúlveda, and Giovanni Volpe. Optical tweezers — from calibration to applications: a tutorial. *Advances in Optics and Photonics*, 13(1):74, mar 2021.

[90] Uttam Manna, Jung-Hoon Lee, Tian-Song Deng, John Parker, Nolan Shepherd, Yossi Weizmann, and Norbert F. Scherer. Selective induction of optical magnetism. *Nano Letters*, 17(12):7196–7206, nov 2017.

[91] Arseniy I. Kuznetsov, Andrey E. Miroshnichenko, Mark L. Brongersma, Yuri S. Kivshar, and Boris Luk'yanchuk. Optically resonant dielectric nanostructures. *Science*, 354(6314), nov 2016.

[92] Li Li, Tanya Hutter, Alexander S. Finnemore, Fu Min Huang, Jeremy J. Baumberg, Stephen R. Elliott, Ullrich Steiner, and Sumeet Mahajan. Metal oxide nanoparticle mediated enhanced Raman scattering and its use in direct monitoring of interfacial chemical reactions. *Nano Letters*, 12(8):4242–4246, jul 2012.

[93] John Parker, Norbert Scherer, and Stephen Gray. Optical magnetism in core-satellite nanostructures excited by vector beams. In Ali Adibi, Shawn-Yu Lin, and Axel Scherer, editors, *Photonic and Phononic Properties of Engineered Nanostructures VIII*. SPIE, feb 2018.

[94] Tian-Song Deng, John Parker, Yuval Yifat, Nolan Shepherd, and Norbert F. Scherer. Dark plasmon modes in symmetric gold nanoparticle dimers illuminated by focused cylindrical vector beams. *The Journal of Physical Chemistry C*, 122(48):27662–27672, nov 2018.

[95] Tian-Song Deng, John Parker, Yutaro Hirai, Nolan Shepherd, Hiroshi Yabu, and Norbert F. Scherer. Designing "metamolecules" for photonic function: Reduced backscattering. *physica status solidi (b)*, 257(12):2000169, aug 2020.

[96] Lei Shi, T. Umut Tuzer, Roberto Fenollosa, and Francisco Meseguer. A new dielectric metamaterial building block with a strong magnetic response in the sub-1.5-micrometer region: Silicon colloid nanocavities. *Advanced Materials*, 24(44):5934–5938, aug 2012.

[97] Andrey B. Evlyukhin, Carsten Reinhardt, Andreas Seidel, Boris S. Luk'yanchuk, and Boris N. Chichkov. Optical response features of Si-nanoparticle arrays. *Physical Review B*, 82(4), jul 2010.

[98] Tianhua Feng, Yi Xu, Wei Zhang, and Andrey E. Miroshnichenko. Ideal magnetic dipole scattering. *Physical Review Letters*, 118(17), apr 2017.

[99] J.M. Geffrin, B. García-Cámara, R. Gómez-Medina, P. Albella, L.S. Froufe-Pérez, C. Eyraud, A. Litman, R. Vaillon, F. González, M. Nieto-Vesperinas, J.J. Sáenz, and F. Moreno. Magnetic and electric coherence in forward- and back-scattered electromagnetic waves by a single dielectric subwavelength sphere. *Nature Communications*, 3(1), nov 2012.

[100] Andrey B. Evlyukhin, Sergey M. Novikov, Urs Zywietz, René Lynge Eriksen, Carsten Reinhardt, Sergey I. Bozhevolnyi, and Boris N. Chichkov. Demonstration of magnetic dipole resonances of dielectric nanospheres in the visible region. *Nano Letters*, 12(7):3749–3755, jun 2012.

[101] Elisabet Xifré-Pérez, Lei Shi, Umut Tuzer, Roberto Fenollosa, Fernando Ramiro-Manzano, Romain Quidant, and Francisco Meseguer. Mirror-image-induced magnetic modes. *ACS Nano*, 7(1):664–668, dec 2012.

[102] Lei Shi, E. Xifré-Pérez, F. J. García de Abajo, and F. Meseguer. Looking through the mirror: Optical microcavity-mirror image photonic interaction. *Optics Express*, 20(10):11247, may 2012.

[103] Lei Xu, Mohsen Rahmani, Khosro Zangeneh Kamali, Aristeidis Lamprianidis, Lavinia Ghirardini, Jürgen Sautter, Rocio Camacho-Morales, Haitao Chen, Matthew Parry, Isabelle Staude, Guoquan Zhang, Dragomir Neshev, and Andrey E. Miroshnichenko. Boosting third-harmonic generation by a mirror-enhanced anapole resonator. *Light: Science & Applications*, 7(1), jul 2018.

[104] Artyom Assadillayev, Tatsuki Hinamoto, Minoru Fujii, Hiroshi Sugimoto, Mark L. Brongersma, and Søren Raza. Plasmon launching and scattering by silicon nanoparticles. *ACS Photonics*, 8(6):1582–1591, may 2021.

[105] Hiroshi Sugimoto and Minoru Fujii. Broadband dielectric–metal hybrid nanoantenna: Silicon nanoparticle on a mirror. *ACS Photonics*, 5(5):1986–1993, mar 2018.

[106] Ivan S. Sinev, Andrey A. Bogdanov, Filipp E. Komissarenko, Kristina S. Frizyuk, Mihail I. Petrov, Ivan S. Mukhin, Sergey V. Makarov, Anton K. Samusev, Andrei V. Lavrinenko, and Ivan V. Iorsh. Chirality driven by magnetic dipole response for demultiplexing of surface waves. *Laser & Photonics Reviews*, 11(5):1700168, sep 2017.

[107] Qifeng Ruan, Nannan Li, Hang Yin, Ximin Cui, Jianfang Wang, and Hai-Qing Lin. Coupling between the Mie resonances of Cu_2O nanospheres and the excitons of dye aggregates. *ACS Photonics*, 5(9):3838–3848, aug 2018.

[108] Zengli Huang, Jianfeng Wang, Zhenghui Liu, Gengzhao Xu, Yingmin Fan, Haijian Zhong, Bing Cao, Chinhua Wang, and Ke Xu. Strong-field-enhanced spectroscopy in silicon nanoparticle electric and magnetic dipole resonance near a metal surface. *The Journal of Physical Chemistry C*, 119(50):28127–28135, dec 2015.

[109] Fu Deng, Hongfeng Liu, and Sheng Lan. Metal substrate-induced line width compression in the magnetic dipole resonance of a silicon nanosphere illuminated by a focused azimuthally polarized beam. *Nanoscale Research Letters*, 13(1), dec 2018.

[110] H. Li, Y. Xu, J. Xiang, X. F. Li, C. Y. Zhang, S. L. Tie, and S. Lan. Exploiting the interaction between a semiconductor nanosphere and a thin metal film for nanoscale plasmonic devices. *Nanoscale*, 8(45):18963–18971, 2016.

[111] Ivan Sinev, Ivan Iorsh, Andrey Bogdanov, Dmitry Permyakov, Filipp Komissarenko, Ivan Mukhin, Anton Samusev, Vytautas Valuckas, Arseniy I. Kuznetsov, Boris S. Luk'yanchuk, Andrey E. Miroshnichenko, and Yuri S. Kivshar. Polarization control over electric and magnetic dipole resonances of dielectric nanoparticles on metallic films. *Laser & Photonics Reviews*, 10(5):799–806, aug 2016.

[112] Munir Hasan Nayfeh and Morton K. Brussel. *Electricity and Magnetism*. John Wiley & Sons, Ltd., 1985.

[113] Andrey E. Miroshnichenko, Andrey B. Evlyukhin, Yuri S. Kivshar, and Boris N. Chichkov. Substrate-induced resonant magnetoelectric effects for dielectric nanoparticles. *ACS Photonics*, 2(10):1423–1428, oct 2015.

[114] Amos Egel. *Accurate optical simulation of disordered scattering layers for light extraction from organic light emitting diodes*. PhD thesis, Karlsruhe Institute of Technology, Karlsruhe, Germany, 2019. Available at `https://doi.org/10.5445/IR/1000093961`.

[115] Jiamiao Yang, Qiaozhi He, Linxian Liu, Yuan Qu, Rongjun Shao, Bowen Song, and Yanyu Zhao. Anti-scattering light focusing by fast wavefront shaping based on multi-pixel encoded digital-micromirror device. *Light: Science & Applications*, 10(1), jul 2021.

[116] Wei Liu and Yuri S. Kivshar. Generalized kerker effects in nanophotonics and meta-optics [invited]. *Optics Express*, 26(10):13085, may 2018.

[117] The MathWorks Inc. Matlab version: 9.12.0.1975300 (r2022a), 2022.

[118] Aleksandar D. Rakić, Aleksandra B. Djurišić, Jovan M. Elazar, and Marian L. Majewski. Optical properties of metallic films for vertical-cavity optoelectronic devices. *Applied Optics*, 37(22):5271, aug 1998.

[119] Jiaming Hao, Wei Yan, and Min Qiu. Super-reflection and cloaking based on zero index metamaterial. *Applied Physics Letters*, 96(10):101109, mar 2010.

[120] Wei Xiong. Molecular vibrational polariton dynamics: What can polaritons do? *Accounts of Chemical Research*, 56(7):776–786, mar 2023.

[121] Garret D. Wiesehan and Wei Xiong. Negligible rate enhancement from reported cooperative vibrational strong coupling catalysis. *The Journal of Chemical Physics*, 155(24):241103, dec 2021.

[122] Bo Xiang, Raphael F. Ribeiro, Matthew Du, Liying Chen, Zimo Yang, Jiaxi Wang, Joel Yuen-Zhou, and Wei Xiong. Intermolecular vibrational energy transfer enabled by microcavity strong light–matter coupling. *Science*, 368(6491):665–667, may 2020.

[123] James A. Hutchison, Tal Schwartz, Cyriaque Genet, Eloïse Devaux, and Thomas W. Ebbesen. Modifying chemical landscapes by coupling to vacuum fields. *Angewandte Chemie International Edition*, 51(7):1592–1596, jan 2012.

[124] Diego R. Abujetas, Johannes Feist, Francisco J. García-Vidal, Jaime Gómez Rivas, and José A. Sánchez-Gil. Strong coupling between weakly guided semiconductor nanowire modes and an organic dye. *Physical Review B*, 99(20), may 2019.

[125] D. Pagel, A. Alvermann, and H. Fehske. Nonclassical light from few emitters in a cavity. *Physical Review A*, 91(4), apr 2015.

[126] Francesco Todisco, Radu Malureanu, Christian Wolff, P. A. D. Gonçalves, Alexander S. Roberts, N. Asger Mortensen, and Christos Tserkezis. Magnetic and electric mie-exciton polaritons in silicon nanodisks. *Nanophotonics*, 9(4):803–814, mar 2020.

[127] Per Lunnemann and A. Femius Koenderink. The local density of optical states of a metasurface. *Scientific Reports*, 6(1), feb 2016.

[128] Lin Cui, Ming-Yuan Huang, Yu-Meng You, Gao-Min Li, Yu-Jun Zhang, Chuan-Kun Liu, and Shi-Lin Liu. Enhancement of magnetic dipole emission at yellow light with polarization-independent hexagonally arrayed nanorods optical metamaterials. *Optical Materials Express*, 6(4):1151, mar 2016.

[129] Brice Rolly, Betina Bebey, Sebastien Bidault, Brian Stout, and Nicolas Bonod. Promoting magnetic dipolar transition in trivalent lanthanide ions with lossless mie resonances. *Physical Review B*, 85(24), jun 2012.

[130] Dmitry N. Chigrin, Deepu Kumar, David Cuma, and Gero von Plessen. Emission quenching of magnetic dipole transitions near a metal nanoparticle. *ACS Photonics*, 3(1):27–34, dec 2015.

[131] Mark Kasperczyk, Steven Person, Duarte Ananias, Luis D. Carlos, and Lukas Novotny. Excitation of magnetic dipole transitions at optical frequencies. *Physical Review Letters*, 114(16), apr 2015.

[132] Freddy T. Rabouw, P. Tim Prins, and David J. Norris. Europium-doped $NaYF_4$ nanocrystals as probes for the electric and magnetic local density of optical states throughout the visible spectral range. *Nano Letters*, 16(11):7254–7260, oct 2016.

[133] Sinan Karaveli and Rashid Zia. Spectral tuning by selective enhancement of electric and magnetic dipole emission. *Physical Review Letters*, 106(19), may 2011.

[134] Shunsuke Murai, Gabriel W. Castellanos, T. V. Raziman, Alberto G. Curto, and Jaime Gómez Rivas. Enhanced light emission by magnetic and electric resonances in dielectric metasurfaces. *Advanced Optical Materials*, 8(16):1902024, may 2020.

[135] W. T. Carnall, P. R. Fields, and K. Rajnak. Electronic energy levels of the trivalent lanthanide aquo ions. iv. Eu^{3+}. *The Journal of Chemical Physics*, 49(10):4450–4455, nov 1968.

[136] N. Noginova, G. Zhu, M. Mavy, and M. A. Noginov. Magnetic dipole based systems for probing optical magnetism. *Journal of Applied Physics*, 103(7):07E901, apr 2008.

[137] R. Hussain, D. Keene, N. Noginova, and M. Durach. Spontaneous emission of electric and magnetic dipoles in the vicinity of thin and thick metal. *Optics Express*, 22(7):7744, mar 2014.

[138] A Volokitina, P Loiko, E Dunina, A Kornienko, J M Serres, M Aguiló, F Díaz, A Pavlyuk, and X Mateos. Polarized spectroscopy of electric and magnetic dipole transitions of Europium (iii) ions in c_2 sites. *Journal of Physics: Conference Series*, 2086(1):012175, dec 2021.

[139] P.A. Loiko, G.E. Rachkovskaya, G.B. Zakharevich, A.A. Kornienko, E.B. Dunina, A.S. Yasukevich, and K.V. Yumashev. Cooperative up-conversion in Eu^{3+},Yb^{3+}-doped SiO_2-PbO-PbF_2-CdF_2 oxyfluoride glass. *Journal of Non-Crystalline Solids*, 392-393:39–44, jun 2014.

[140] P. Mohanty and S. Ram. Light emission associated with the $^5D_0 \rightarrow {}^7F_3$ forbidden transition in Eu^{3+} cations dispersed in an Eu^{3+}:Al_2O_3 mesoporous structure. *Philosophical Magazine Letters*, 86(6):375–384, 2006.

[141] Edo Waks and Deepak Sridharan. Cavity QED treatment of interactions between a metal nanoparticle and a dipole emitter. *Physical Review A*, 82(4), oct 2010.

[142] Koichi Okamoto, Saurabh Vyawahare, and Axel Scherer. Surface-plasmon enhanced bright emission from CdSe quantum-dot nanocrystals. *Journal of the Optical Society of America B*, 23(8):1674, aug 2006.

[143] Xue-Wen Chen, Vahid Sandoghdar, and Mario Agio. Coherent interaction of light with a metallic structure coupled to a single quantum emitter: From superabsorption to cloaking. *Physical Review Letters*, 110(15), apr 2013.

[144] Wei Zhang, Alexander O. Govorov, and Garnett W. Bryant. Semiconductor-metal nanoparticle molecules: Hybrid excitons and the nonlinear fano effect. *Physical Review Letters*, 97(14), oct 2006.

[145] A. Ridolfo, O. Di Stefano, N. Fina, R. Saija, and S. Savasta. Quantum plasmonics with quantum dot-metal nanoparticle molecules: Influence of the Fano effect on photon statistics. *Physical Review Letters*, 105(26), dec 2010.

[146] Ryan D. Artuso and Garnett W. Bryant. Strongly coupled quantum dot-metal nanoparticle systems: Exciton-induced transparency, discontinuous response, and suppression as driven quantum oscillator effects. *Physical Review B*, 82(19), nov 2010.

[147] A. Manjavacas, F. J. García de Abajo, and P. Nordlander. Quantum plexcitonics: Strongly interacting plasmons and excitons. *Nano Letters*, 11(6):2318–2323, may 2011.

[148] S. A. Tatarkova, A. E. Carruthers, and K. Dholakia. One-dimensional optically bound arrays of microscopic particles. *Physical Review Letters*, 89(28), dec 2002.

[149] Kishan Dholakia and Pavel Zemánek. Colloquium: Gripped by light: Optical binding. *Reviews of Modern Physics*, 82(2):1767–1791, jun 2010.

[150] Kayn A. Forbes, David S. Bradshaw, and David L. Andrews. Optical binding of nanoparticles. *Nanophotonics*, 9(1):1–17, nov 2019.

[151] David S. Bradshaw and David L. Andrews. Optically induced forces and torques: Interactions between nanoparticles in a laser beam. *Phys. Rev. A*, 72:033816, Sep 2005.

[152] Davit Hakobyan and Etienne Brasselet. Left-handed optical radiation torque. *Nat. Photonics*, 8(8):610–614, 2014.

[153] Silvia Albaladejo, Juan José Sáenz, and Manuel I Marqués. Plasmonic nanoparticle chain in a light field: A resonant optical sail. *Nano Lett.*, 11(11):4597–4600, 2011.

[154] Yohai Roichman and David G. Grier. Three-dimensional holographic ring traps. In David L. Andrews, Enrique J. Galvez, and Gerard Nienhuis, editors, *SPIE Proceedings*. SPIE, feb 2007.

[155] Zijie Yan, Manas Sajjan, and Norbert F. Scherer. Fabrication of a material assembly of silver nanoparticles using the phase gradients of optical tweezers. *Physical Review Letters*, 114(14), apr 2015.

[156] Jana Damková, Lukáš Chvátal, Jan Ježek, Jindřich Oulehla, Oto Brzobohatỳ, and Pavel Zemánek. Enhancement of the 'tractor-beam' pulling force on an optically bound structure. *Light Sci. Appl.*, 7(1):17135, 2018.

[157] Fan Nan and Zijie Yan. Synergy of intensity, phase, and polarization enables versatile optical nanomanipulation. *Nano Letters*, 20(4):2778–2783, mar 2020.

[158] José A. Rodrigo, Mercedes Angulo, and Tatiana Alieva. All-optical motion control of metal nanoparticles powered by propulsion forces tailored in 3d trajectories. *Photonics Research*, 9(1):1, dec 2021.

[159] Yuanjie Yang, Yu-Xuan Ren, Mingzhou Chen, Yoshihiko Arita, and Carmelo Rosales-Guzmán. Optical trapping with structured light: a review. *Advanced Photonics*, 3(03), may 2021.

[160] Oto Brzobohatý, Lukáš Chvátal, Alexandr Jonáš, Martin Šiler, Jan Kaňka, Jan Ježek, and Pavel Zemánek. Tunable soft-matter optofluidic waveguides assembled by light. *ACS Photonics*, 6(2):403–410, jan 2019.

[161] Fan Nan and Zijie Yan. Tuning nanoparticle electrodynamics by an optical-matter-based laser beam shaper. *Nano Letters*, 19(5):3353–3358, apr 2019.

[162] Oto Brzobohatý, Lukáš Chvátal, and Pavel Zemánek. Optomechanical properties of optically self-arranged colloidal waveguides. *Opt. Lett.*, 44(3):707–710, Feb 2019.

[163] Xiang Han, Hui Luo, Guangzong Xiao, and Philip H. Jones. Optically bound colloidal lattices in evanescent optical fields. *Opt. Lett.*, 41(21):4935–4938, Nov 2016.

[164] Vassili Demergis and Ernst-Ludwig Florin. Ultrastrong optical binding of metallic nanoparticles. *Nano Lett.*, 12(11):5756–5760, 2012.

[165] Tetsuhiro Kudo, Shang-Jan Yang, and Hiroshi Masuhara. A single large assembly with dynamically fluctuating swarms of gold nanoparticles formed by trapping laser. *Nano Letters*, 18(9):5846–5853, 2018. PMID: 30071730.

[166] Aleksey S. Tsipotan, Marina A. Gerasimova, Vitaliy V. Slabko, and Aleksandr S. Aleksandrovsky. Laser-induced wavelength-controlled self-assembly of colloidal quasi-resonant quantum dots. *Opt. Express*, 24(10):11145–11150, May 2016.

[167] Bernhard Lamprecht, Gerburg Schider, RT Lechner, Harald Ditlbacher, Joachim R Krenn, Alfred Leitner, and Franz R Aussenegg. Metal nanoparticle gratings: Influence of dipolar particle interaction on the plasmon resonance. *Phys. Rev. Lett.*, 84(20):4721, 2000.

[168] Vira V Kravets, Oleg A Yeshchenko, Victor V Gozhenko, Leonidas E Ocola, David A Smith, James V Vedral, and Anatoliy O Pinchuk. Electrodynamic coupling in regular arrays of gold nanocylinders. *J. Phys. D: Appl. Phys.*, 45(4):045102, 2012.

[169] Anatoliy O Pinchuk and George C Schatz. Nanoparticle optical properties: Far-and near-field electrodynamic coupling in a chain of silver spherical nanoparticles. *Mater. Sci. Eng. B*, 149(3):251–258, 2008.

[170] Peter Nordlander, C Oubre, E Prodan, K Li, and MI Stockman. Plasmon hybridization in nanoparticle dimers. *Nano Lett.*, 4(5):899–903, 2004.

[171] Prashant K Jain and Mostafa A El-Sayed. Plasmonic coupling in noble metal nanostructures. *Chem. Phys. Lett.*, 487(4-6):153–164, 2010.

[172] FJ Garcia De Abajo. Colloquium: Light scattering by particle and hole arrays. *Rev. Mod. Phys*, 79(4):1267, 2007.

[173] Weijia Wang, Mohammad Ramezani, Aaro I Väkeväinen, Päivi Törmä, Jaime Gómez Rivas, and Teri W Odom. The rich photonic world of plasmonic nanoparticle arrays. *Mater. Today*, 21(3):303–314, 2018.

[174] Vasyl G Kravets, Andrei V Kabashin, William L Barnes, and Alexander N Grigorenko. Plasmonic surface lattice resonances: A review of properties and applications. *Chem. Rev.*, 118(12):5912–5951, 2018.

[175] Charles Cherqui, Marc R Bourgeois, Danqing Wang, and George C Schatz. Plasmonic surface lattice resonances: Theory and computation. *Acc. Chem. Res.*, 52(9):2548–2558, 2019.

[176] SRK Rodriguez, MC Schaafsma, A Berrier, and J Gómez Rivas. Collective resonances in plasmonic crystals: Size matters. *Physica B Condens. Matter*, 407(20):4081–4085, 2012.

[177] Craig F Bohren and Donald R Huffman. *Absorption and Scattering of Light by Small Particles*. John Wiley & Sons, 2008.

[178] Shengli Zou, Nicolas Janel, and George C Schatz. Silver nanoparticle array structures that produce remarkably narrow plasmon lineshapes. *J. Chem. Phys*, 120(23):10871–10875, 2004.

[179] Leif J Sherry, Shih-Hui Chang, George C Schatz, Richard P Van Duyne, Benjamin J Wiley, and Younan Xia. Localized surface plasmon resonance spectroscopy of single silver nanocubes. *Nano Lett.*, 5(10):2034–2038, 2005.

[180] Materials and methods and additional information are available in Supplementary Materials for *Electrodynamic Interference and Coupling in Nanoparticle-based Optical Matter Arrays*.

[181] John Moore, Conrad Stanitski, and Peter Jurs. *Principles of Chemistry: The Molecular Science*. Cengage Learning, 2009.

[182] Gabriel Araneda, Stefan Walser, Yves Colombe, Daniel B Higginbottom, Jürgen Volz, Rainer Blatt, and Arno Rauschenbeutel. Wavelength-scale errors in optical localization due to spin–orbit coupling of light. *Nat. Phys.*, 15(1):17–21, 2019.

[183] Barbara Wild, Lina Cao, Yugang Sun, Bishnu P Khanal, Eugene R Zubarev, Stephen K Gray, Norbert F Scherer, and Matthew Pelton. Propagation lengths and group velocities of plasmons in chemically synthesized gold and silver nanowires. *ACS Nano*, 6(1):472–482, 2012.

[184] Erin M Hicks, Shengli Zou, George C Schatz, Kenneth G Spears, Richard P Van Duyne, Linda Gunnarsson, Tomas Rindzevicius, Bengt Kasemo, and Mikael Käll. Controlling plasmon line shapes through diffractive coupling in linear arrays of cylindrical nanoparticles fabricated by electron beam lithography. *Nano Lett.*, 5(6):1065–1070, 2005.

[185] Edward M Purcell, Henry Cutler Torrey, and Robert V Pound. Resonance absorption by nuclear magnetic moments in a solid. *Phys. Rev.*, 69(1-2):37, 1946.

[186] Matthew Pelton. Modified spontaneous emission in nanophotonic structures. *Nat. Photonics*, 9(7):427, 2015.

[187] Yuen-Ron Shen. The principles of nonlinear optics. *wi*, 1984.

[188] Rongchao Jin, Justin E Jureller, and Norbert F Scherer. Precise localization and correlation of single nanoparticle optical responses and morphology. *Appl. Phys. Lett.*, 88(26):263111, 2006.

[189] J. M. Taylor and G. D. Love. Spontaneous symmetry breaking and circulation by optically bound microparticle chains in gaussian beam traps. *Phys. Rev. A*, 80:053808, Nov 2009.

[190] Taka aki Yano, Yuta Tsuchimoto, Remo Proietti Zaccaria, Andrea Toma, Alejandro Portela, and Masahiko Hara. Enhanced optical magnetism for reversed optical binding forces between silicon nanoparticles in the visible region. *Optics Express*, 25(1):431, jan 2017.

[191] Urs Zywietz, Andrey B. Evlyukhin, Carsten Reinhardt, and Boris N. Chichkov. Laser printing of silicon nanoparticles with resonant optical electric and magnetic responses. *Nature Communications*, 5(1), mar 2014.

[192] C. Tserkezis, P. A. D. Gonçalves, C. Wolff, F. Todisco, K. Busch, and N. A. Mortensen. Mie excitons: Understanding strong coupling in dielectric nanoparticles. *Physical Review B*, 98(15), oct 2018.

[193] Rebecca Heilmann, Aaro I. Väkeväinen, Jani-Petri Martikainen, and Päivi Törmä. Strong coupling between organic dye molecules and lattice modes of a dielectric nanoparticle array. *Nanophotonics*, 9(2):267–276, dec 2019.

[194] Tanya Hutter, Fu Min Huang, Stephen R. Elliott, and Sumeet Mahajan. Near-field plasmonics of an individual dielectric nanoparticle above a metallic substrate. *The Journal of Physical Chemistry C*, 117(15):7784–7790, apr 2013.

[195] Timo A Nieminen, Simon John Wyatt Parkin, Norman Richard Heckenberg, and Halina Rubinsztein-Dunlop. Optical torque and symmetry. In *Optical Trapping and Optical Micromanipulation*, volume 5514, pages 254–264. International Society for Optics and Photonics, 2004.

[196] Arthur Ashkin, James M Dziedzic, JE Bjorkholm, and Steven Chu. Observation of a single-beam gradient force optical trap for dielectric particles. *Opt. Lett.*, 11(5):288–290, 1986.

[197] Richard W Bowman and Miles J Padgett. Optical trapping and binding. *Rep. Prog. Phys*, 76(2):026401, 2013.

[198] Shengli Zou and George C Schatz. Narrow plasmonic/photonic extinction and scattering line shapes for one and two dimensional silver nanoparticle arrays. *J. Chem. Phys*, 121(24):12606–12612, 2004.

[199] Naomi J Halas, Surbhi Lal, Wei-Shun Chang, Stephan Link, and Peter Nordlander. Plasmons in strongly coupled metallic nanostructures. *Chem. Rev.*, 111(6):3913–3961, 2011.

[200] Wei Zhou and Teri W Odom. Tunable subradiant lattice plasmons by out-of-plane dipolar interactions. *Nat. Nanotechnol.*, 6(7):423, 2011.

[201] Emil Prodan, Corey Radloff, Naomi J Halas, and Peter Nordlander. A hybridization model for the plasmon response of complex nanostructures. *Science*, 302(5644):419–422, 2003.

[202] José A Rodrigo, Mercedes Angulo, and Tatiana Alieva. Tailored optical propulsion forces for controlled transport of resonant gold nanoparticles and associated thermal convective fluid flows. *Light Sci. Appl*, 9(1):1–11, 2020.

[203] Trimble, Inc. SketchUp Make version: 17.0.18899, 2017.